

**INTERNAL FLOW EFFECTS ON PERFORMANCE OF  
COMBUSTION POWERED ACTUATORS**

A Thesis  
Presented to  
The Academic Faculty

by

Ashok Rajendar

In Partial Fulfillment  
of the Requirements for the Degree  
Master of Science in the  
School of Mechanical Engineering

Georgia Institute of Technology  
December 2011

**INTERNAL FLOW EFFECTS ON PERFORMANCE OF  
COMBUSTION POWERED ACTUATORS**

Approved by:

Dr. Ari Glezer, Advisor  
School of Mechanical Engineering  
*Georgia Institute of Technology*

Dr. Thomas Crittenden  
School of Mechanical Engineering  
*Georgia Institute of Technology*

Dr. Timothy Lieuwen  
School of Aerospace Engineering  
*Georgia Institute of Technology*

Date Approved: 9<sup>th</sup> November 2011

## ACKNOWLEDGEMENTS

I would first like to thank my advisor, Dr. Ari Glezer. His technical knowledge was of great assistance when I encountered obstacles in my work, while his immense experience helped me through events like my first conference. I am grateful to have had the chance to work with him. I am also grateful to have worked with Dr. Thomas Crittenden. As the originator of combustion actuator technology, I was fortunate to be privy to his advice regarding the project as well as his perspective as a long-time member of the Georgia Tech community. Without his assistance and advice, my time here would have been considerably more difficult. I would also like to thank Dr. Timothy Lieuwen, who has consented to be on my thesis committee. The financial support for this project was provided by NASA's Subsonic Rotary Wing Program, to which I am grateful, as without this body's support my work would not have been possible.

I would also like to thank my colleagues at the Fluid Mechanics Research Laboratory, whose support and friendship have made my experience here a memorable and positive one. Beyond helping me maintain my sanity, the technical advice and help they provided helped me cope with capricious experimental equipment and uncooperative software. I would like to acknowledge George Woo, Dan Brozowski, Abe Gissen, John Kearney, and Mark Simpson, who have all been of great help over the years, as well as John Culp, and Hanif Hunter, whom I have had occasion to share thoughts, jokes, and late-night cups of

coffee with while grousing about work. I also want to thank Jack Crawford, my friend and roommate for many years.

Most of all, I would like to thank my family and loved ones. I am grateful to my wife Shweta, who has helped ease the difficult times that are part and parcel of higher education. Finally, my mother and father have supported me without reservation or hesitation, not just during my time here, but always. Whenever I made a misstep, or when times were tough, they always helped guide me back to where I needed to be. To these people I am indebted, as they have all contributed greatly to my success.

# TABLE OF CONTENTS

	Page
ACKNOWLEDGEMENTS	iii
LIST OF TABLES	vii
LIST OF FIGURES	viii
LIST OF SYMBOLS	xii
SUMMARY	xv
 <u>CHAPTER</u>	
<b>1 INTRODUCTION</b>	<b>1</b>
1.1 Motivation	1
1.2 Brief Outline	5
<b>2 LITERATURE REVIEW</b>	<b>7</b>
2.1 Small-Scale Combustion	7
2.2 The COMPACT Technology	10
2.2.1 Premixed Designs	11
2.2.2 Non-premixed Designs	14
2.2.3 Impulse of the Actuation Jet	18
<b>3 EXPERIMENTAL SETUP</b>	<b>22</b>
3.1 Combustion Actuator Design, Spark Ignition, and Pressure Measurement	22
3.2 Imaging and Particle Image Velocimetry	25
3.3 Operating Conditions	27
<b>4 EFFECT OF VARIATION OF AIR INLET JET MOMENTUM FLUX ON ACTUATOR PERFORMANCE</b>	<b>29</b>
4.1 Overview of Baseline Configuration	29

4.2 Exploration of Baseline Configuration Performance	31
4.3 Flow Visualization of Baseline Configuration Actuator Undergoing Combustion ( $d_{air} = 0.79$ mm)	48
4.3.1 Non-combusting Flow Field	48
4.3.2 Combusting Flow Field Evolution	52
4.4 Changes in Actuator Performance due to Variation of Air Inlet Jet Momentum Flux	58
4.4.1 Non-combusting Flow Field	60
4.4.2 Combusting Flow Field Evolution	63
4.5 Investigation of the Refill Process	70
<b>5 EFFECT OF VARIATION OF INLET CONFIGURATION ON ACTUATOR PERFORMANCE</b>	<b>75</b>
5.1 Combustion Actuator Inlet Configurations	75
5.2 Pressure Testing of Inlet Configurations	76
5.3 PIV for F1 and E5	79
5.3.1 F1 (High Peak Pressure Configuration)	79
Non-Combusting Flow Field	79
Combusting Flow Field Evolution	82
5.3.2 E5 (Low Peak Pressure Configuration)	87
Non-Combusting Flow Field	87
Combusting Flow Field Evolution	87
5.4 Flow Field Types and General Effects	94
<b>6 CONCLUSION</b>	<b>99</b>
APPENDIX: Table A	102
REFERENCES	104

## LIST OF TABLES

	Page
Table 1: Peak pressure, mean inlet velocity, momentum flux ratio with respect to hydrogen jet, selected timing parameters, and actuation jet impulse for $d_{air} = 0.79, 1.63, \text{ and } 2.92 \text{ mm}$ , $Q = 66.7 \text{ std. cm}^3/\text{s}$ , $\Phi = 0.75$ , and $f = 5\text{Hz}$	60
Table 2: Peak pressure, start time, rise time, pulse duration, and actuation jet impulse for configurations A2, F1, and E5, $d_{air} = 0.79 \text{ mm}$ , $Q = 66.7 \text{ std. cm}^3/\text{s}$ , $\Phi = 0.75$ , and $f = 5\text{Hz}$	79
Table A: Peak pressures of all tested configurations	102

## LIST OF FIGURES

	Page
Figure 1.1: Schematic of combustion actuator	1
Figure 1.2: Premixed and non-premixed combustion actuators	2
Figure 1.3: Transitory reattachment of separated flow over a stalled airfoil (angle of attack, $\alpha = 19^\circ$ ) due to single actuation pulse (Woo et al. 2008)	4
Figure 2.1: Example of time-dependent, phase-averaged pressure inside combustion chamber of a premixed actuator design during the combustion process, combined with Schlieren of actuation jet, $V = 1 \text{ cm}^3$ (aspect ratio $H/D = 1.27$ ), $d_{ex} = 1.30 \text{ mm}$ , $\Phi = 0.7$ , and $f = 30 \text{ Hz}$ (Crittenden 2003)	12
Figure 2.2: Time scales associated with combustion actuator operation	16
Figure 3.1: An assembled COMPACT device – <b>a.</b> oxidizer inlet tube, <b>b.</b> securing plate, <b>c.</b> variable inlet position combustion chamber unit, <b>d.</b> combustion chamber interior, <b>e.</b> front optical access windows, <b>f.</b> exhaust orifice, <b>g.</b> fuel inlet tube, <b>h.</b> pressure transducer holder, and <b>i.</b> back plate	22
Figure 3.2: Combustion chamber schematic, view of right side containing air inlet array (left) and front view (right)	23
Figure 3.3: Camera setup and illuminated planes	27
Figure 4.1: Schematic of actuator in baseline configuration, showing arrays of air (left) and fuel (right) inlets. Inlets in use are filled in. The green dashed line shows the plane in which the axes of the inlets and the exhaust orifice lie	30
Figure 4.2: Phase-averaged pressure-time traces during combustion, $Q = 66.7 \text{ s-cm}^3/\text{s}$ , $d_{air} = 0.79\text{mm}$ , $f = 5\text{Hz}$ . $\Phi = 1.0$ (—), $0.9$ (—), $0.8$ (—), $0.7$ (—), $0.6$ (—), $0.5$ (—)	32
Figure 4.3: Variation of $p_{max}$ and $J_1$ with $\Phi$ , $Q = 66.7 \text{ s-cm}^3/\text{s}$ , $d_{air} = 0.79\text{mm}$ , $f = 5\text{Hz}$ , $p_{max}/p_{atm}$ (—), $J_1/J_0$ (—)	33
Figure 4.4: Variation of pressure trace timing with $\Phi$ , $Q = 66.7 \text{ s-cm}^3/\text{s}$ , $d_{air} = 0.79\text{mm}$ , $f = 5\text{Hz}$ , $\Delta t_{rise}/\tau_{refill}$ (—), $\Delta t_{pulse}/\tau_{refill}$ (—)	35



- Figure 4.5: Variation of  $p_{max}$  with  $f$ ,  $Q = 66.7 \text{ s-cm}^3/\text{s}$ ,  $d_{air} = 0.79\text{mm}$ ,  
 $f = 5\text{Hz}$ ,  $\Phi = 1.0$  (—),  $0.9$  (—),  $0.8$  (—),  $0.7$  (—),  $0.6$  (—),  
 $0.5$  (—) 37
- Figure 4.6: Idealized variation of  $p_{max}$  with  $f$ , with instantaneous mixing  
and perfect scavenging 40
- Figure 4.7: Phase-averaged pressure-time traces during combustion,  
 $\Phi = 0.75$ ,  $d_{air} = 0.79\text{mm}$ ,  $f = 5\text{Hz}$ ,  $Q = 100$  (—),  $80$  (—),  
 $66.7$  (—),  $50$  (—),  $33.3 \text{ s-cm}^3/\text{s}$  (—) 42
- Figure 4.8: Variation of  $p_{max}$  and  $J_1$  with  $Q$ ,  $\Phi = 0.75$ ,  $d_{air} = 0.79\text{mm}$ ,  
 $f = 5\text{Hz}$ ,  $p_{max}/p_{atm}$  (—),  $J_1/J_0$  (—) 43
- Figure 4.9: Variation of pressure trace timing with  $Q$ ,  $\Phi = 0.75$ ,  
 $d_{air} = 0.79\text{mm}$ ,  $f = 5\text{Hz}$ ,  $\Delta t_{rise}/\tau_{refill}$  (—),  $\Delta t_{pulse}/\tau_{refill}$  (—) 44
- Figure 4.10: Variation of  $p_{max}$  with  $f$ ,  $\Phi = 0.75$ ,  $d_{air} = 0.79\text{mm}$ ,  $f = 5\text{Hz}$ ,  
 $Q = 100$  (—),  $80$  (—),  $66.7$  (—),  $50$  (—),  $33.3 \text{ s-cm}^3/\text{s}$  (—) 45
- Figure 4.11: Planar PIV cross-sections of the non-combusting flow field,  
 $d_{air} = 0.79 \text{ mm}$ ,  $Q = 66.7 \text{ s-cm}^3/\text{s}$ ,  $\Phi = 0.75$  and  $f = 5\text{Hz}$ ,  
a) planes P1-5, b) planes N1-3 49
- Figure 4.12: Planar PIV cross-sections of the combusting flow field,  
 $d_{air} = 0.79 \text{ mm}$ ,  $Q = 66.7 \text{ s-cm}^3/\text{s}$ ,  $\Phi = 0.75$  and  $f = 5\text{Hz}$ ,  
a)  $t = 0.1 \text{ ms}$  ( $t/\tau_{refill} = 0.002$ ) and b)  $0.3 \text{ ms}$  ( $0.007$ ), c)  $0.5 \text{ ms}$   
( $0.011$ ), d)  $0.7 \text{ ms}$  ( $0.016$ ) 53
- Figure 4.13: Images showing propagation of the flame front in the central  
plane P3 at a)  $t = 0.3 \text{ ms}$  and b)  $0.5 \text{ ms}$  after spark ignition, and  
c) the change in  $r_{eff}$  with time. The blue arrows mark the  
location of the air inlet 57
- Figure 4.14: Pressure traces,  $Q = 66.7 \text{ s-cm}^3/\text{s}$ ,  $\Phi = 0.75$  for a)  $d_{air} = 1.63$   
b)  $2.92 \text{ mm}$ ,  $f = 5$  (—),  $10$  (—),  $15 \text{ Hz}$  (—) 59
- Figure 4.15: Planar PIV cross-sections of the non-combusting flow field,  
 $d_{air} = 2.92 \text{ mm}$ ,  $Q = 66.7 \text{ s-cm}^3/\text{s}$ ,  $\Phi = 0.75$  and  $f = 5\text{Hz}$ ,  
a) planes P1-5, b) planes N1-3 61

- Figure 4.16: Planar PIV cross-sections of the combusting flow field,  $d_{air} = 2.92$  mm,  $Q = 66.7$  s-cm<sup>3</sup>/s,  $\Phi = 0.75$  and  $f = 5$ Hz, a)  $t = 0.1$  ms ( $t/\tau_{refill} = 0.002$ ) and b) 0.3 ms (0.007), c) 0.5 ms (0.011), d) 0.7 ms (0.016) 64
- Figure 4.17: Images showing propagation of the flame front in the central plane P3 at a)  $t = 0.3$  ms and b) 0.5 ms after spark ignition, and c) the change in  $r_{eff}$  with time. The blue arrows mark the location of the air inlet 66
- Figure 4.18: Planar cross-sections of TKE of the combusting flow field,  $d_{air} = 0.79$  mm,  $Q = 66.7$  s-cm<sup>3</sup>/s,  $\Phi = 0.75$  and  $f = 5$ Hz, a) non-combusting flow, b) 0.3 ms (0.007), and c) 0.5 ms (0.011) 68
- Figure 4.19: Planar cross-sections of TKE of the combusting flow field,  $d_{air} = 2.92$  mm,  $Q = 66.7$  s-cm<sup>3</sup>/s,  $\Phi = 0.75$  and  $f = 5$ Hz, a) non-combusting flow, b) 0.3 ms (0.007), and c) 0.5 ms (0.011) 69
- Figure 4.20: Images used to determine seed particle density, a) PIV image of P3 seeded flow, b) contrast-enhanced image, c) conversion to black and white, and d) computation of seed density based on mean brightness of selected area 72
- Figure 4.21: Variation of  $\rho_s/\rho_{s0}$  with  $t/\tau_{refill}$ ,  $Q = 66.7$  s-cm<sup>3</sup>/s,  $\Phi = 0.75$ , for  $d_{air} = 0.79$  mm at  $f = 5$  (—), 10 (—), and 15 Hz (—), and for  $d_{air} = 2.92$  mm at  $f = 5$  (—), 10 (—), and 15 Hz (—) 73
- Figure 5.1: Schematic of actuator in showing arrays of air inlets (left) and fuel inlets (right) 76
- Figure 5.2: Pressure traces,  $Q = 66.7$  s-cm<sup>3</sup>/s,  $\Phi = 0.75$ ,  $d_{air} = 0.79$  mm for a) cfg. F1 and b) cfg. E5, for  $f = 5$  (—), 10 (—), 15 Hz (—); cfg. A2,  $f = 5$  Hz (—) 78
- Figure 5.3: Planar PIV cross-sections of the non-combusting flow field for configuration F1, P1-5,  $d_{air} = 0.79$  mm,  $Q = 66.7$  s-cm<sup>3</sup>/s,  $\Phi = 0.75$  and  $f = 5$ Hz, a) planes P1-5, b) planes N1-3 80
- Figure 5.4: Planar PIV cross-sections of the combusting flow field of configuration F1,  $d_{air} = 0.79$  mm,  $Q = 66.7$  s-cm<sup>3</sup>/s,  $\Phi = 0.75$  and  $f = 5$ Hz, a)  $t = 0.1$  ms ( $t/\tau_{refill} = 0.002$ ), b) 0.3 ms (0.007), c) 0.5 ms (0.011) 83
- Figure 5.5: Images showing propagation of the flame front in the central plane P3 for configuration F1 at a)  $t = 0.3$  ms and b) 0.5 ms after spark ignition, and c) the change in  $r_{eff}$  with time 86

Figure 5.6: Planar PIV cross-sections of the non-combusting flow field for configuration E5, P1-5, $d_{air} = 0.79$ mm, $Q = 66.7$ s-cm <sup>3</sup> /s, $\Phi = 0.75$ and $f = 5$ Hz, a) planes P1-5, b) planes N1-3	88
Figure 5.7: Planar PIV cross-sections of the combusting flow field of configuration E5, $d_{air} = 0.79$ mm, $Q = 66.7$ s-cm <sup>3</sup> /s, $\Phi = 0.75$ and $f = 5$ Hz, a) $t = 0.1$ ms ( $t/\tau_{refill} = 0.002$ ), b) 0.5 ms (0.011), c) 0.9 ms (0.023)	90
Figure 5.8: Images showing propagation of the flame front in the central plane P3 for configuration E5 at a) $t = 0.3$ ms and b) 0.5 ms after spark ignition, and c) the change in $r_{eff}$ with time	92
Figure 5.9: Simplified flow field for air inlet jet in corner of array	95
Figure 5.10: Simplified flow field for air inlet jet in middle hole on outer row of array	96
Figure 5.11: Simplified flow field for air inlet jet in central hole of array	97

## LIST OF SYMBOLS

$A_{ex}$	exhaust orifice area
$d_{air}$	diameter of air inlet
$d_{ex}$	diameter of exhaust orifice
$d_{fuel}$	diameter of fuel inlet
$D$	diameter of cylindrical combustion chamber
$E_{comb}$	energy release during combustion
$E_A$	activation energy of reaction
$f$	actuation frequency
$f_{max}$	maximum stable actuation frequency
$f_{refill}$	refill, or ideal frequency, $Q/V$
$F$	thrust produced by actuation jet
$H$	combustion chamber height
$J_0$	impulse of non-combusting exhaust orifice outflow
$J_1$	impulse of actuation jet during pressure pulse
$J_{jet}$	impulse of actuation jet
$m_{air}$	mass of air (oxidizer)
$m_{fuel}$	mass of fuel (hydrogen)
$\dot{m}_p$	mass flow rate of combustion products
$M$	Mach number
$n$	order of reaction
$p$	pressure inside combustion chamber

$p_{ex}$	pressure at exit plane of exhaust orifice
$p_{max}$	maximum pressure during combustion
$p_t$	total (stagnation) pressure
$Q$	overall volumetric flow rate
$r_{eff}$	effective (spherical) radius
$Re_{air}$	Reynolds number of air inlet jet
$R_u$	universal gas constant
$S$	flame speed
$S_F$	speed of flame front, including gas expansion
$S_L$	laminar flame speed
$S_T$	turbulent flame speed
$t$	time after spark ignition
$t_I$	time after ignition of reactants (as shown by PIV images)
$t_{end}$	time when pressure pulse ends
$t_{max}$	time at which $p_{max}$ occurs
$t_{start}$	time when pressure pulse begins
$T$	temperature
$\bar{T}$	mean temperature in reaction zone
$T_b$	temperature of burned products
$T_u$	temperature of unburned reactants
$T_{conv}$	convective time scale
$u$	speed of fluid
$\overline{u_{air}}$	mean speed of air jet at inlet orifice

$v'$	velocity fluctuation
$v'_{rms}$	root-mean-square velocity fluctuation
$V$	volume of combustion chamber
$A$	angle of attack
$\gamma$	ratio of specific heats ( $c_p/c_v$ )
$\Delta t$	time between first and second images of a PIV image pair
$\Delta t_{mix}$	mixing time
$\Delta t_{pulse}$	combustion pressure pulse duration
$\Delta t_{rise}$	combustion pressure pulse rise time
$\mu_{air}$	viscosity of air
$\rho$	density
$\rho_0$	density of reactants
$\rho_s$	seeding density
$\rho_{s0}$	seeding density of non-combusting flow
$\rho_{air}$	density of air at inlet orifice
$\tau$	period ( $1/f$ )
$\tau_{refill}$	refill, or ideal period ( $1/f_{refill}$ )
$\Phi$	equivalence ratio

## SUMMARY

The performance of a non-premixed combustion-powered fluidic actuator for high speed flow control is characterized with particular emphasis on changes in performance due to variation of the momentum flux of the oxidizer inlet jet and variation of the relative locations of the fuel and oxidizer inlets. A mixture of fuel and oxidizer is ignited inside the actuator's combustion chamber, creating a transient, high-momentum actuation jet which can be used to alter the flow field around aerodynamic bodies. The inlet conditions and geometry affect the flow field inside the actuator, which in turn affects the mixing of fuel and oxidizer species and the propagation of the flame. Actuator performance is characterized using time-resolved pressure measurements within the device's combustion chamber during the combustion process. Phase-locked, high-magnification Particle Image Velocimetry (PIV) is used to obtain several planar cross-sections of the three-dimensional flow field both in the presence and the absence of combustion. Analysis of the pressure data together with the non-combusting and combusting flow fields reveals how the momentum flux of the oxidizer inlet jet and the relative locations of the inlet orifices can significantly affect actuator performance.

# CHAPTER 1

## INTRODUCTION

### 1.1 Motivation

COMbustion Powered ACTuation (COMPACT) is a novel technology that can be used to apply active flow control to aerodynamic bodies. The onset of separated flow around airfoils can result in significant loss of lift and greatly increased drag, placing severe limitations on the performance of both fixed- and rotary-wing aircraft in certain flight regimes. Active control of separation can be applied to aircraft to reduce drag, increase lift, or increase maneuverability, resulting in higher attainable speeds, increased range, or superior flying characteristics.

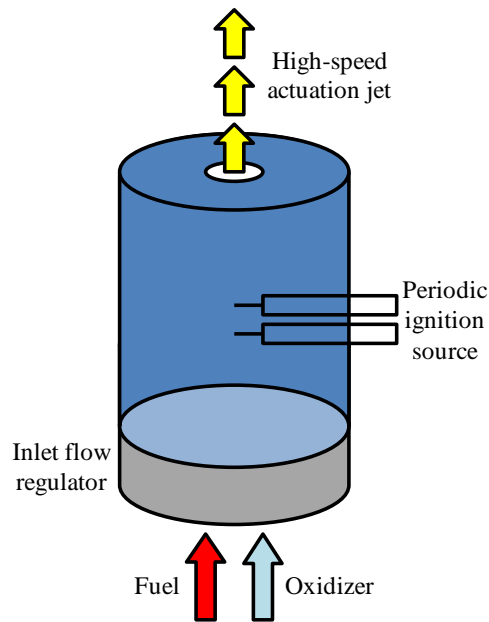


Figure 1.1: Schematic of combustion actuator



COMPACT technology has been the subject of a number of earlier investigations (e.g.: Crittenden 2003, Warta 2007). The actuator is analogous to a fluidic amplifier in that low-momentum reactants enter the chamber and high-momentum products exit. Figure 1.1 is a schematic of the combustion actuator concept. Reactants flow into the chamber via orifices or flow regulating elements, where they are then ignited by a controllable periodic ignition source. The ensuing rise in pressure shuts off the flow of reactants into the chamber and creates a high-speed actuation jet issuing from the exhaust orifice. If the combustion-induced internal pressure is sufficiently high the actuation jet can momentarily approach sonic speeds (the exhaust orifice is a simple, straight-walled, circular design, so the jet cannot exceed  $M = 1$ ).

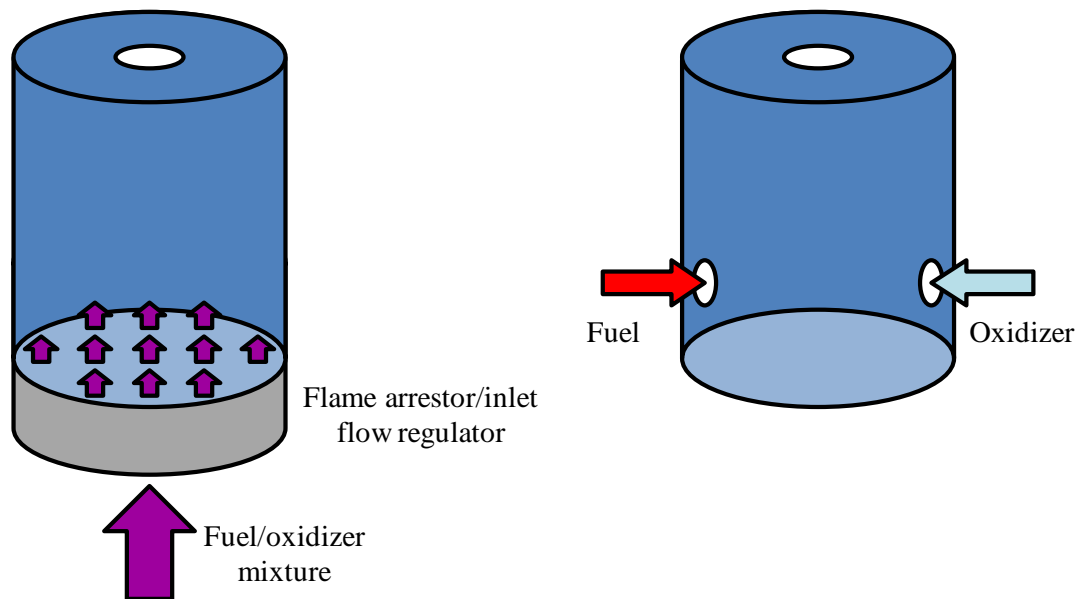


Figure 1.2: Premixed (left) and non-premixed combustion actuators

Figure 1.2 shows the two main types of combustion actuator: the premixed actuator (cf. Crittenden 2003), where fuel and oxidizer are mixed upstream and enter the chamber through a single inlet orifice, and the non-premixed actuator (cf. Warta 2007), a

newer design where there are separate oxidizer and fuel inlets and mixing of reactants takes place inside the combustion chamber. As will be discussed in Chapter 2, previous investigations have shown that the latter produces better performance. Thus the non-premixed actuator is the focus of the present work. Premixed combustion-based actuation was first explored by Crittenden (2003) as an alternative to standard synthetic jets for high-speed flow control. The early investigations showed that the COMPACT devices were relatively small and light and the potential to use the on-board fuel supply could mean a reduction in weight relative to other active flow control technologies. Continued work by Warta (2007) showed the utility of non-premixed operation, and explored high-frequency operation.

An early application of COMPACT devices to separation control was reported by Funk et al. (2002). They showed that the boundary layer of a stalled airfoil at a constant angle of attack of  $24^\circ$  can be temporarily re-attached using momentary pulses, where the frequency of actuation was on the order of the convective time-scale of flow over the airfoil, and thus of the resulting flow instabilities. The duration of the control jet pulse is of  $O(1 \text{ ms})$ , at least an order of magnitude shorter than the convective time-scale. Later investigations by Brzozowski and Glezer (2006) showed that the actuation pulse severs the separated vorticity layer causing a slight reduction in circulation. This is followed by the formation of an attached boundary layer that grows in the streamwise direction, resulting in a net increase in circulation of approximately 25% lasting several (8-10) convective time scales ( $T_{conv}$ ) until the flow relaxes and separation recurs. Figure 1.3 shows the re-attachment of stalled flow due to a single combustion pulse, suggesting a reattachment mechanism similar to that of synthetic jet actuation (Woo et al. 2008).

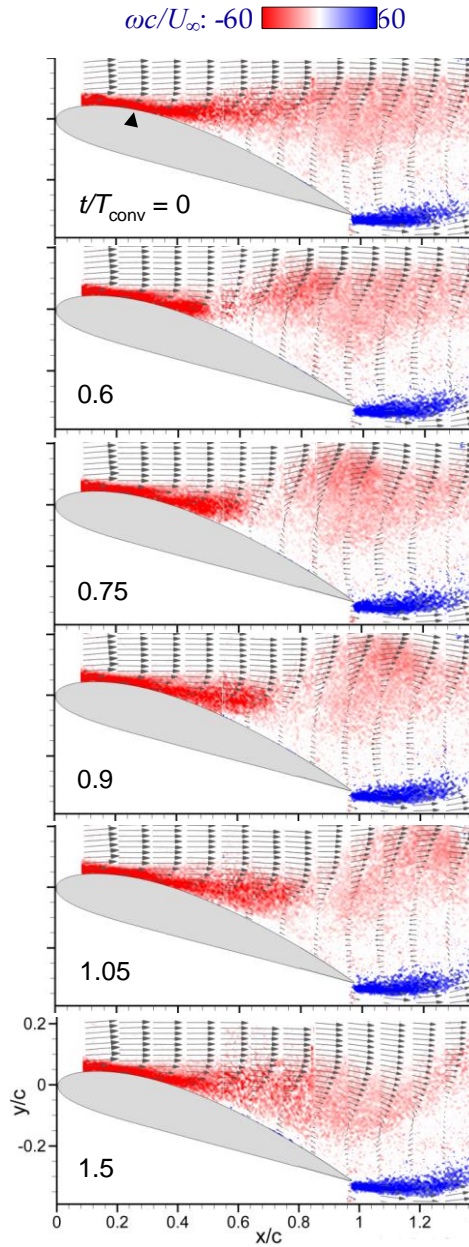


Figure 1.3: Transitory reattachment of separated flow over a stalled airfoil (angle of attack,  $\alpha = 19^\circ$ ) due to single actuation pulse (Woo et al. 2008)

Recent developments by Woo et al. (2009) have shown that it is possible to take advantage of the slow relaxation of the flow following each pulse by using “bursts” comprising several pulses at high frequencies to successively increase circulation by as much as 58%, followed by slow relaxation to the stalled flow.

This thesis discusses further investigations into the operation of the COMPACT devices themselves. Specifically, it focuses on understanding how the momentum flux of the oxidizer inlet jet and the relative locations of the oxidizer and fuel inlets within the actuator's combustion chamber affect the internal flow field, and how such changes in the flow field impact the performance of the actuator. It is the flow structures and characteristic velocities that determine the efficacy of mixing within the actuator, the various time-scales required for mixing and chamber evacuation, and other important criteria that affect flame propagation, and thus the momentum of the actuation jet.

## **1.2 Brief Outline**

Chapter 2 contains an overview of the literature relating to small-scale combustion and combustion actuation. Devices utilizing small-scale combustion are discussed, including micro gas turbines and Wankel engines and the challenges encountered in operating these devices due to the small scales involved. The previous work on COMPACT devices is also discussed, with an overview of the initial work by Crittenden and the development by Warta. The pressure pulse and actuation jet are discussed, along with the various time-scales of interest during the combustion process as well as the methods of determination of flame speed and thrust.

Chapter 3 discusses the design and construction of the experimental actuator, detailing the features that allow the inlet geometry to be varied, and the typical conditions under which the actuator is tested. It also provides an overview of the experimental setup for the two diagnostic methods: PIV and time-dependent measurements of pressure during the combustion process.

Chapter 4 discusses the effect that changing the oxidizer inlet diameter has on combustion actuator performance, based on a particular baseline configuration. Actuator performance is characterized by the changes in pressure over the combustion process, while images of the combustion inside the chamber are processed using PIV to identify different flow features associated with the observed changes in pressure when conditions are varied.

Chapter 5 describes the changes in performance that occur when the inlet configuration (i.e.: the relative locations of the fuel and oxidizer inlets) is varied. Finally, Chapter 6 is a summary and conclusion of the findings of the present investigation, as well as suggestions for possible future investigations.

## **CHAPTER 2**

### **LITERATURE REVIEW**

#### **2.1 Small-Scale Combustion**

In recent years, combustion within volumes of  $1 \text{ cm}^3$  or smaller has been applied to two fields: power generation and propulsion. The appeal of small-scale combustion is in the large amount of energy that can be extracted from a relatively small mass of hydrocarbon fuel due to the high energy density of such fuels compared to current battery technology (45 MJ/kg for octane, vs. 1.2 MJ/kg for a lithium-based battery). While hydrogen provides 140 MJ/kg, storage is problematic: even when liquefied, the density per unit volume is less than a third that of octane. Nevertheless, it is a popular fuel in combustion experiments and is used in the development of COMPACT because it is gaseous and thus does not require atomization within the combustion chamber. Moreover, its wide flammability range enables operation over a wide range of equivalence ratios and flow rates. If small-scale combustion systems can be made sufficiently small, reliable, and inexpensive to meet commercial requirements they would be extremely desirable, as they would likely weigh significantly less than a battery-powered system with the same amount of stored energy.

There are several issues that arise from the length scales [O(1 cm) or smaller] over which small-scale combustion devices must operate. Fernandez-Pello's (2002) survey of small-scale combustion for power generation discusses some of the challenges associated with combustion occurring in volumes with length scales on the order of the characteristic flame thickness. As the combustion chamber volume is decreased, heat loss

from the chamber (which lowers the flame speed, see Equations 2.4 and 2.5) becomes important due to the increase in surface-area-to-volume ratio. If the combustion dimensions are on the order of a few cubic millimeters, depending upon operating conditions, they are at the scale of the quenching distance (the length scale at which heat transfer and loss of radicals from the flame to the walls of the combustion chamber is rapid enough to extinguish the flame). If the length scale is on the order of but larger than the quenching distance, the resultant low flame speed leads to poor performance. If the length scale is equal to or smaller than the quenching distance, the flame will be extinguished.

A number of investigations of small-scale combustion were carried out at the MIT Gas Turbine Laboratory. Epstein et al. (1997) provides an overview of two devices: a small-scale gas turbine for propulsion or power generation and a small-scale rocket engine, both of which were microfabricated from silicon. The gas turbine is a single-shaft design with a radial turbine and compressor. Its combustion chamber is  $40 \text{ mm}^3$  in volume ( $0.04 \text{ cm}^3$ ). These gas turbines and the internal combustion engines discussed below comprise the majority of small-scale combustion devices with moving parts. One significant problem with such devices is friction between the moving parts, which is relatively greater than the friction in macro-scale engines due to the greater surface-area-to-volume ratio of the small-scale devices. As a result, the microfabricated engines devices do not approach the efficiency of macro-scale gas turbines or gasoline powered piston engines (approximately 30-50% [Mattingly 2005] and 10-20% [Moran and Shapiro 2004] respectively). Nevertheless, as long as micro-engines can provide higher power and energy density than batteries of comparable size, they can still be very useful.

The utility of this particular gas turbine is discussed in terms of the potential high power-to-weight ratio and possible use in mobile electronics or Unmanned Aerial Vehicles (UAVs). However, the design has been plagued by low efficiency, in part because of leakage due to problems with tolerances. Another challenge is the low Reynolds number of the flow inside the device, including the combustion chamber. The resultant laminar flow in these regions of the device hinders efficient mixing and combustion. As yet, these gas turbines have not produced net power.

Waitz et al. (1998) discusses a small-scale combustor for the gas turbine, mentioning problems such as heat transfer from the small-volume combustion chamber to the compressor, which reduces efficiency. In later work on the turbine Protz (2000) achieved a rotation speed of 30,000 rpm when the device was used as a turbocharger (cold flow, no combustion), while Spadacinni (2004) further investigated the combustor design by dividing it into “hot” and “cold” regions and experimenting with catalysts. Despite the challenges, the advantages of small-scale gas turbines are attractive and other teams have worked on them, including Shan et al. (2006) who developed a working combustor and compressor-turbine assembly, though it did not produce net power. In related work on small-scale rockets, London et al. (2001) developed the earlier design (Epstein et al. 1997) into a “rocket-on-a-chip”, complete with turbopumps and valves for the reactants. Thrust on the order of 1 N was achieved, corresponding to a thrust-to-weight ratio of 85:1, but like the gas turbine, the rocket experiences problems with heat loss from the combustion chamber.

Work on microfabricated small-scale internal combustion engines for power generation has included Wankel-type rotary engines and reciprocating free-piston engines



of both compression- and spark-ignition designs. Rotary engines have been the subject of a series of investigations by Fu et al. (2001), who built a steel device with a displacement of  $77.5 \text{ mm}^3$ . Once again, heat loss is a problem, and while the device produces net positive power, its mechanical efficiency is approximately 0.2%, due in part to low compression. Further work by Swanger et al. (2004) has produced a larger micro-Wankel engine, displacing  $350 \text{ mm}^3$ , which has better sealing of the rotor resulting in corresponding improvements in compression ratio and power.

Free-piston designs were also investigated by a number of different investigators, including Aichlamayr et al. (2002) and Ogawa et al. (2004). The latter is a spark-ignited Otto-cycle design with a  $15 \text{ mm}^3$  combustion chamber, built onto a chip with the inlet and exhaust channels micromachined into a wafer of silicon. The former is an innovative design that utilizes Homogeneous Charge Compression Ignition (HCCI). The engine is designed such that the premixed charge auto-ignites at Top Dead Center, and thus does not need a spark plug and the associated ancillary equipment. Low efficiency is a problem for this design as well, though computer models have suggested that the design is feasible.

## **2.2 The COMPACT Technology**

The devices discussed in the previous section are used for propulsion and power. This is typical of the interest in small-scale combustion, where the technology is developed to replace batteries and motors. In contrast, the purpose of COMPACT technology is to produce high momentum-flux pulsed actuators. The basic concept as discussed in Section 1.1 is described in Crittenden (2003), along with the effects of a

variety of conditions on actuator performance. Two actuator configurations have been developed and have been differentiated by the method of mixing of fuel and oxidizer.

### 2.2.1 Premixed design

The first actuators were of a premixed design. In a premixed actuator, fuel and oxidizer are mixed upstream of the combustion chamber and then enter the chamber through a sintered metal plate that functions as a passive flow-regulating and flame-arresting element. Once the mixture is ignited by the spark source, the pressure inside the chamber rises until the inlet flow through the sintered metal element is shut off. The size of the pores in the element is such that it inhibits flame propagation upstream. Figure 2.1 shows the pressure-time history inside the combustion chamber of a typical case, along with phase-locked Schlieren images of the actuation jet (Crittenden 2003).

Time-resolved pressure measurement to quantify performance has been used since the original work of Crittenden (2003). Figure 2.1 shows that after spark ignition, pressure begins to rise, along with the mass flow through the exhaust orifice, indicating that the speed and momentum flux of the actuation jet rises as well. At peak pressure the jet is strongest and, as the magnified Schlieren images show, shock structures indicate that the orifice is choked with the actuation jet emerging at  $M = 1$ . After peak pressure is attained, the pressure slowly relaxes to ambient, accompanied by falling speed and momentum of the actuation jet. By about 5 ms following spark ignition, the actuation jet has effectively ceased and flow from the exhaust orifice is only due to the inflow of reactants.

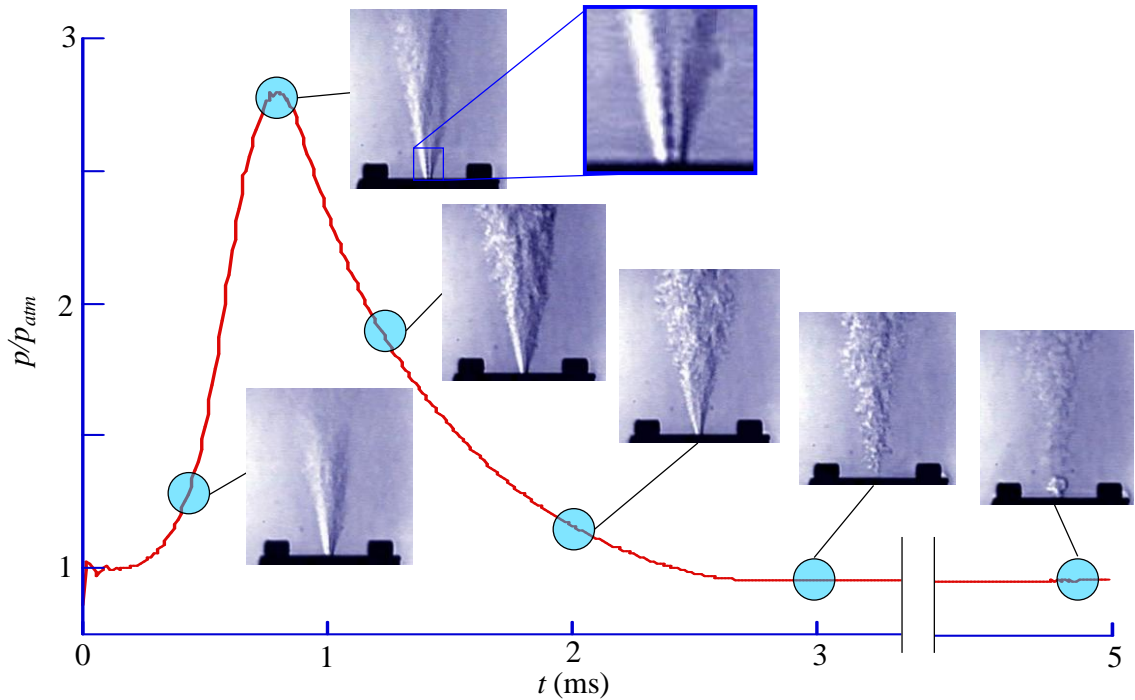


Figure 2.1: Example of time-dependent, phase-averaged pressure inside combustion chamber of a premixed actuator design during the combustion process, combined with Schlieren of actuation jet,  $V = 1 \text{ cm}^3$  (aspect ratio  $H/D = 1.27$ ),  $d_{ex} = 1.30 \text{ mm}$ ,  $\Phi = 0.7$ , and  $f = 30 \text{ Hz}$  (Crittenden 2003)

Premixed actuators were first investigated because it was assumed that mixing the reactants upstream of the chamber would allow the actuator to operate at relatively high frequencies by eliminating the mixing time of reactants within the chamber. The sintered metal element typically covers the entire diameter of the base of the chamber, resulting in a low-speed inlet flow. This was assumed to result in less mixing of reactants with the remaining combustion products than if the inlet flow were a high-speed turbulent jet, and was thus to be more efficient at scavenging the chamber.

Crittenden (2003) demonstrated the use of both hydrogen and propane as viable fuels with air as the oxidizer. As mentioned in Chapter 1, the main diagnostic data were time-resolved pressure measurements inside the chamber. Since the goal of COMPACT

is to produce a high-momentum actuation jet that can be pulsed at as high a frequency as possible, an actuator that performs well produces high peak pressures and is capable of high stable actuation frequencies. In order to achieve these goals, the chamber must have efficient scavenging, quick and effective mixing of reactants, and short pulse durations. For a single actuation pulse, propane produces longer pulse durations (7.3 vs. 4.5 ms for hydrogen at equivalence ratio  $\Phi = 1.0$ ), whereas hydrogen produces effective combustion over a wider range of equivalence ratios (a lower limit of  $\Phi = 0.4$ , vs.  $\Phi = 0.8$  for propane), and produces higher peak pressures ( $p_{max}/p_{atm} = 4.4$  vs. 1.68 at  $\Phi = 1.0$ ). Premixed actuators were characterized in terms of their response to variation of equivalence ratio  $\Phi$ , flow rate  $Q$ , combustion chamber volume  $V$ , exhaust orifice diameter  $d_{ex}$ , aspect ratio (the ratio of chamber height to depth)  $H/D$ , and actuation frequency  $f$ . Of the various cases tested, the  $V = 1 \text{ cm}^3$ ,  $H/D = 1.72$  combustor yields the highest peak pressures near  $\Phi = 1$  for both fuels, which decreases with  $\Phi$  ( $p_{max}/p_{atm}$  for propane and hydrogen are 1.26 at  $\Phi = 0.8$ , and 1.23 at  $\Phi = 0.4$  respectively). Likewise, decreasing the diameter of the exhaust orifice results in higher peak pressures along with a corresponding increase of pulse duration (for  $d_{ex} = 1.78$  and 0.79 mm,  $p_{max}/p_{atm}$  and the pulse durations  $\Delta t_{pulse}$  are 3.73 and 5.09, and 1.5 and 3.0 ms respectively). Increasing  $f$  results in lower peak pressures and longer pulse durations: for 5 and 15 Hz, peak pressures are 4.3 to 2.4 atm respectively ( $\Phi = 1$ ). Increasing  $Q$ , results in increased peak pressures: for  $Q = 10$  and  $100 \text{ cm}^3/\text{s}$ ,  $p_{max}/p_{atm} = 2.61$  and 4.11 respectively.

Before discussing the non-premixed COMPACT configuration, it is important to consider another implementation of combustion actuation, namely a resonant detonation actuator (Beck, et al. 2005). Similar to COMPACT, the goal is to produce a pulsed jet for

aerodynamic flow control. This type of device operates by filling a tube with reactants (e.g.: hydrogen and air), and then igniting it at one end, causing a detonation wave to travel down the tube, producing an actuation jet from the exhaust orifice at the other end. The tube is approximately 40 cm long, and is designed to produce actuation pulses at over 1000 Hz. Cutler and Drummond (2006) demonstrated operation of an actuator with a 20 cm tube at 1400 Hz. In both cases, the size of the device is considerable, being much larger than what is typically considered small-scale combustion. Moreover, the device uses active metering of fuel, where an actuated valve is used to control the flow into the tube. While one of the goals was to use passive metering (as in most COMPACT devices), this has not been achieved yet. The more complicated design and larger size of the resonant detonation actuator means that it is in a different niche from the designs investigated in this thesis.

### 2.2.2 Non-Premixed Designs

The COMPACT concept was extended by Crittenden and Warta (2006) to include a nonpremixed actuator. Unlike the earlier premixed designs, the nonpremixed actuator combustion chamber has separate fuel and oxidizer inlets so that the mixing of reactants occurs inside the chamber, adding a delay that is associated with a characteristic mixing time. However the removal of the sintered metal flow-regulating element allows the reactants to be delivered into the chamber by high-momentum jets. The resulting performance is superior to that of premixed designs in terms of peak pressure and maximum operating frequency, and is associated with the enhanced small-scale motions present within the combustion chamber prior to ignition. It was shown that actuation

frequencies as high as 500 Hz are attainable, albeit at greatly reduced peak pressure ( $p_{max}/p_{atm} \approx 1.3$ ).

Warta (2007) conducted an extensive comparison of premixed and nonpremixed actuators based on time-resolved combustor pressure measurements. The impact on peak pressure and maximum stable actuation frequency of fuel type, equivalence ratio, flow rate, exhaust orifice diameter, chamber volume, and aspect ratio, ignition location, and inlet type was investigated. Of the premixed and nonpremixed types, the latter typically provides better performance by both metrics stated earlier: for a given case ( $\Phi = 0.41$ ,  $Q = 100$  std.  $\text{cm}^3/\text{s}$ ,  $V = 2$   $\text{cm}^3$ ,  $d_{ex} = 1.78$  mm,  $f = 35$  Hz)  $p_{max}/p_{atm}$  and  $\Delta t_{pulse}$  for the nonpremixed and premixed actuators are 4.5 and 2.75, and 2.0 and 2.5 ms respectively. For the same case, the maximum stable operating frequencies  $f_{max}$  for the nonpremixed and premixed designs are 110 and 95 Hz respectively. These data are typical, with the nonpremixed designs outperforming the premixed designs over the greater portion of the parameter space.

Warta's nonpremixed actuators were of two basic types: air injection, and air-fuel injection. In the former, air enters the chamber via a small-diameter orifice, while fuel enters via the same type of sintered metal flow-regulating element used in premixed actuators. In the latter, air and fuel both enter the chamber via separate small-diameter orifices. The use of separate orifices allows for more flexibility of inlet placement; since the chamber's internal flow field is determined by the shape of the interior and the placement of the inlets, varying the latter provides greater control of the flow and thus chamber performance. The use of the sintered metal element allows for greater pressure differentials between the chamber and the fuel line, thus allowing the chamber to

maintain lower pressures over the operating cycle, as is the case for high frequency operation, but its fixed location limits the extent to which the internal flow can be manipulated.

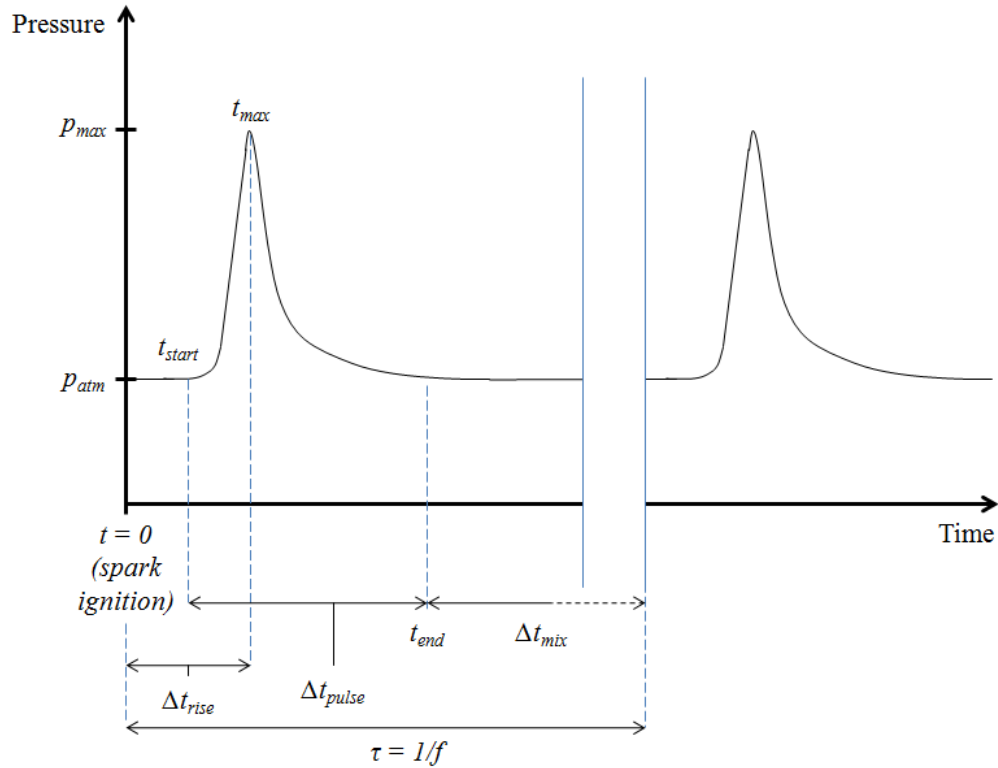


Figure 2.2: Time scales associated with combustion actuator operation

Investigations of both premixed and non-premixed actuators suggest that there are important time scales during the operation of the device that characterize processes such as mixing and scavenging. Figure 2.2 shows a schematic of the pressure pulse with annotated time scales of interest.  $t_{start}$  is the time at which the combustor pressure begins to rise following spark ignition, and is defined here as the time at which  $p = 0.05(p_{max} - p_{atm}) + p_{atm}$ , or when the pressure has risen by 5% of the maximum pressure change relative to the non-combusting baseline ( $p/p_{atm} = 1$ ). It can be viewed as a measure of the difficulty of igniting the mixture. A higher  $t_{start}$  implies that a longer

time required for the reactant mixture to ignite, and thus a longer time for the spark to transfer sufficient heat to the mixture and provide a sufficient concentration of free radicals. It is important to note that  $t_{start}$  is not the time at which the flame front begins propagating, as the PIV data in Chapter 4 shows that the actual presence of the flame front occurs considerably earlier.

The peak pressure is attained at  $t_{max}$  and the pressure pulse ends at  $t_{end}$ . Together, they define the operating characteristics of the chamber: the rise time from spark ignition  $\Delta t_{rise} = t_{max} - (t = 0) = t_{max}$  and the duration of the pulse is  $\Delta t_{pulse} = t_{end} - t_{start}$ .  $\Delta t_{rise}$  may be used as a rough measure of the flame propagation speed  $S_F$ , the speed of the flame front with respect to the center of the combustion chamber.  $S_F$  includes the effects of expansion of gas behind the flame as well as wrinkling of the flame front due to the small scale motions of the flow. This is distinct from the flame speed  $S$ , which is dependent on the thermodynamic state and chemical composition of the flow (Turns 2000). Assuming that  $t_{max}$  occurs when the flame front reaches the walls of the chamber and is extinguished, then  $r_{eff}/\Delta t_{rise} \sim S_F$ , where  $r_{eff}$  is the effective radius of the chamber (i.e. the radius of a sphere of the same volume as the chamber, since the flame front is assumed to propagate spherically; for  $V = 2.95 \text{ cm}^3$ ,  $r_{eff} = 8.9 \text{ mm}$ ). The effective radius is then an estimate of the distance travelled by the flame front during the rise time.

The mixing time for the reactants after combustion is complete is  $\Delta t_{mix}$ . For a nonpremixed actuator, it is defined as the time required for incoming reactants to displace remnant exhaust gasses and mix together, while for a premixed actuator, it is solely the time required to displace exhaust gasses. The mixing time can be longer than  $\tau$ , the period of actuation. When it is longer, mixing is incomplete and combustion efficiency



decreases. As stated above, early investigations into COMPACT started with premixed configurations because it was assumed that this would minimize  $\Delta t_{mix}$ . However as Crittenden and Warta (2006), and Warta (2007) show, the performance of premixed actuators is not necessarily better than nonpremixed designs. Due to the improved performance of the nonpremixed actuators, and specifically the versatility of the air-fuel injection type, this was chosen as a natural starting point for further investigation by Rajendar et al. (2008), and in the present work.

Finally, an alternate route has been investigated by Crittenden and Raghu (2009), who have worked on a device that combines COMPACT devices and fluidic actuators. The fluidic actuator produces a high frequency oscillating jet from a steady or intermittent (low-frequency) fluid inflow. This suggests that the low frequency [O(100 Hz)] input jet from the combustion actuator can drive the high-frequency [O(1,000-10,000 Hz)] fluidic oscillator, using no moving parts.

### 2.2.3 Impulse of the Actuation Jet and Flame Propagation within the Actuator

The impulse of the actuation jet over a single combustion cycle  $J_I$  is one of the two key performance parameters (the other is the maximum stable operating frequency). Impulse is calculated as the time integral of the thrust of the actuation jet,  $F$ , which is related to the combustor pressure  $p$ , and can be obtained by treating the actuator as a rocket engine with the exhaust orifice operating as the rocket's nozzle (Mattingly 2005):

$$F = (p_{ex} - p_{atm})A_{ex} + \dot{m}_p V_{ex} \quad (2.1)$$

where  $p_{ex}$  is the pressure at the exit of the exhaust orifice,  $A_{ex}$  is the area of the exhaust orifice,  $\dot{m}_p$  is the mass flow rate of the actuation jet at velocity  $V_{ex}$ . Substituting the ideal gas and isentropic compressible flow equations into Equation 2.1 gives Equation 2.2:

$$F = [(p_{ex} - p_{atm}) + \gamma P_{ex} M] A_{ex} \quad (2.2)$$

where  $\gamma$  is the ratio of specific heats ( $c_p/c_v$ ), which for  $300 \leq T \leq 1000$  K varies between 1.40 and 1.34 (Moran and Shapiro 2004), and thus may be approximated as 1.37 for the purposes of calculating impulse. When the exhaust is not choked ( $M < 1$ ),  $p_{ex} = p_{atm}$ . The variation of  $p_{ex}$  with  $M$  is given by (Mattingly 2005):

$$\frac{p_{ex}}{p_t} = \left(1 + \frac{\gamma-1}{2} M^2\right)^{-\gamma/(\gamma-1)} \quad (2.3)$$

where  $p_t$  is the stagnation pressure. In the COMPACT device,  $p_t$  may be approximated as the pressure inside the combustion chamber due to the low flow velocity inside the combustion chamber (the dynamic pressure is on the order of  $10^1$ - $10^2$  Pa while the static pressure is on the order of  $10^5$  Pa). Thus at  $M = 1.0$ ,  $p_{ex}/p = 0.53$ . Since  $p$  and  $p_{ex}$  are known, the Mach number can be calculated and used to compute the thrust as shown in Equation 2.2, which is then integrated over the duration of the actuation cycle to obtain the impulse of the actuation jet  $J_I$ .

As shown in Chapter 4, the performance of the actuator is directly related to the propagation of the flame front, which is in turn dependent on the nature of the flow field within the chamber. It is thus necessary to understand what factors affect flame speed.

The data in Chapters 4 and 5 also show that the flame front is “wrinkled”. The flame propagation is thus turbulent in nature, and is characterized as being in the so-called “wrinkled laminar” regime of turbulent flame propagation. Turns (2000) defines the flame speed for this regime as:

$$S_T = \left(1 + \frac{v'_{rms}}{S_L}\right) S_L \quad (2.4)$$

where  $v'_{rms}$  is the root-mean-square velocity fluctuation and  $S_L$  is the laminar flame speed.  $S_T$  is greater than the corresponding value for  $S_L$  within this regime because the wrinkling of the flame front increases its effective area, allowing it to consume reactants at a greater rate. One measure of the intensity of small-scale motion is the Turbulent Kinetic Energy (TKE), the energy of the small-scale (turbulent) velocity fluctuations,  $\frac{1}{2}\rho(v')^2$  (Tennekes and Lumley 1972). The instantaneous turbulent velocity fluctuation, the difference between the mean flow velocity and the instantaneous velocity, is  $v'$ , so  $v'_{rms}$  can be treated as the square root of  $(v')^2$ .

Turns (2000) shows that  $S_L$  is dependent upon:

$$S_L \propto \bar{T}^{0.375} T_u T_b^{-n/2} \exp\left(-\frac{E_A}{2R_u T_b}\right) P^{(n-2)/2} \quad (2.5)$$

$\bar{T}$  is the mean temperature across the reaction zone,  $T_u$  and  $T_b$  are the unburned temperature of the reactants and the burned temperature of the products respectively,  $n$  is the overall order of the reaction (dependent on the concentration of reactants),  $E_A$  is the activation energy of the combustion reaction, and  $R_u$  is the universal gas constant.

Equation 2.5 is derived by considering a 1D, constant area, steady flow of premixed reactants into a flame resulting from a single-step exothermic combustion reaction, with products exiting the flame. The approximations include assuming constant specific heats and no pressure change across the flame. Because of these simplifications and the geometry used, Equations 2.4 and 2.5 do not yield the rate of flame propagation within the COMPACT combustion chamber, as discussed in Section 2.2.2, but they are useful in determining why performance changes are observed when inlet conditions are changed.

## CHAPTER 3

### EXPERIMENTAL SETUP

#### 3.1 Combustion Actuator Design, Spark Ignition, and Pressure Measurement

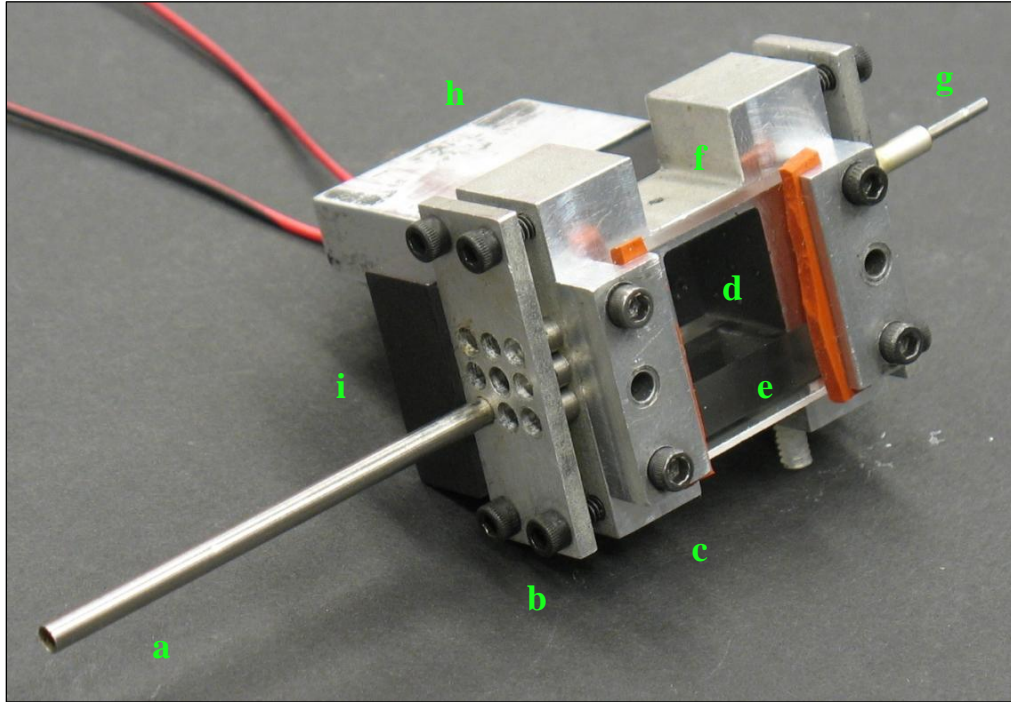


Figure 3.1: Modular COMPACT test chamber – **a.** oxidizer inlet tube, **b.** securing plate, **c.** variable inlet position combustion chamber unit, **d.** combustion chamber interior, **e.** front optical access windows, **f.** exhaust orifice, **g.** fuel inlet tube, **h.** pressure transducer holder, and **i.** back plate

The investigations described in this thesis were conducted using a modular non-premixed combustion actuator, shown in Figure 3.1. It comprises a  $\text{cm}^3$ -scale combustion chamber fed by one air inlet and one fuel inlet, inside which the reactant mixture is ignited by two columnar spark electrodes (not visible in figure). The inlets are circular orifices located on opposite walls of the chamber. The actuator is designed to enable

incremental variation of the relative location of the air and fuel inlets. The combustion chamber comprises an aluminum block that forms the left, right, and top walls, an aluminum back plate which is the rear wall, and interchangeable walls that can either be quartz for optical access (as shown) or aluminum for extended operation.

Fuel and oxidizer flow into the chamber through two inlets, each of which is part of a  $3 \times 3$  array on opposing walls of the chamber. The flow tubes are held in place by collars that provide mechanical support and sealing, and the unused holes on both sides are plugged when not in use.

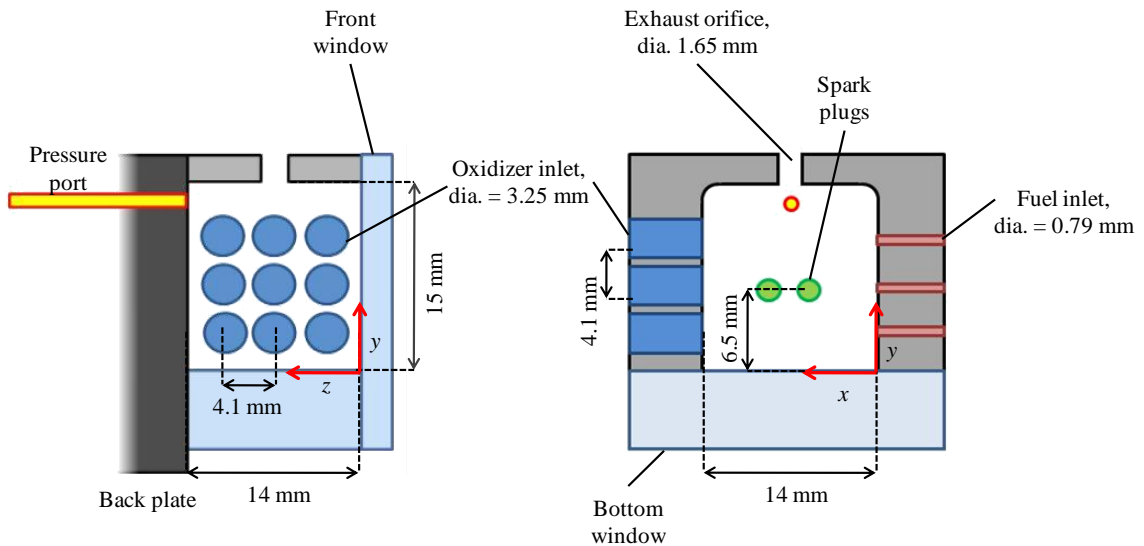


Figure 3.2: Combustion chamber schematic, view of right side containing air inlet array (left) and front view (right)

Figure 3.2 shows a schematic of the chamber from the right and front views, with the aluminum chamber walls shown as light grey. The combustion chamber cross-section is  $15 \times 14$  mm with a depth of 14 mm, yielding a total chamber volume of  $V = 2.95 \text{ cm}^3$ . Ceramic insulators which carry the spark ignition wires are inserted through the center of the rear wall of the chamber (back plate, in dark gray), with the resulting spark gap

(approximately 1 mm wide) located 7 mm from the back plate and 6.5 mm from the bottom wall. The diameter of the straight-walled circular exhaust orifice  $d_{ex}$  is 1.65 mm and it is positioned so that its axis is normal to the axes of the air and fuel inlets. The holes for the inlets are arranged on a square grid, with a 4.1 mm center-to-center spacing. The fuel inlets are all circular orifices with diameter  $d_{fuel} = 0.79$  mm which is unchanged throughout the experiments. The oxidizer inlets are also circular orifices with a larger diameter,  $d_{air} = 3.25$  mm. This enables variation of the size of the injection port into the chamber by the use of a variety of flow tube inserts. One such tube is shown in Figure 3.1 (component a). In the present experiments,  $d_{air} = 0.79, 1.63,$  and  $2.92$  mm. Figure 3.2 also shows two sets of axes. Together these comprise the 3D axes  $x$ - $y$ - $z$  of a standard right-handed coordinate system used in the flow field plots shown in Chapters 4 and 5.

Spark ignition is effected using a modified automotive electronic ignition system which is triggered by the LabVIEW code running on a laboratory computer, which also controls phase-locked sampling of the combustor pressure during the combustion process. The time-dependent pressure is measured using a high-frequency, high-temperature piezoresistive pressure transducer. The transducer has a range of up to 200 psia (approximately 13.5 atm), is mounted in the back plate of the combustor, and is connected via a 15 mm long port to the combustion chamber itself. The sampling rate is 100 kHz and the sampling lasts up to 50 ms following spark ignition. The computer triggers the spark using a periodic square wave set at the actuation frequency  $f$ . This square wave signal also triggers data acquisition from the pressure transducer, recording the time-dependent pressure during the combustion process. This process is repeated for a selected number of combustion cycles (50 cycles in the data presented in Chapters 4 and

5), producing a series of individual pressure-time histories, or pressure “traces” for each iteration of the cycle. The phase-averaged pressure trace for a given case (cf. Figure 2.1) is obtained by calculating the mean pressure at each time step from all the individual pressure traces from all recorded cycles.

### **3.2 Imaging and Particle Image Velocimetry**

The flow field inside the combustion chamber is quantified by Particle Image Velocimetry (PIV) with incense smoke used for seeding the flow. For an in-depth description of PIV and the various techniques used, consult Raffel et al. (1998). A dual-head Yag laser (532 nm) is used to illuminate a single cross-sectional plane within the chamber for two exposures. Images are recorded by a 1 megapixel CCD camera using a microscope objective lens such that the nominal field of view measures  $15 \times 15$  mm and the magnification is  $14 \mu\text{m}/\text{pixel}$ . A band-pass filter ( $532 \pm 2$  nm) is used in front of the camera to reduce optical transmission of light emanating from the spark ignition and combustion processes. The interior surfaces of the chamber are painted matte black using heat-resistant paint in order to provide a high-contrast background for the incense particles to be illuminated against, and to reduce reflections from the walls that could obscure the particles. The image pair of the seeded flow is cross-correlated by the PIV software to produce a 2D vector field that is an approximation of the instantaneous flow field in that plane.

The lasers and image acquisition hardware are controlled by LaVision PIV software. Combustor ignition is controlled by a National Instruments board, which also triggers PIV image acquisition. User-specified time delays between the spark trigger and



the PIV trigger enable acquisition of phase-locked PIV data (100 image pairs). Data are also collected for the nominally steady non-combusting flow (flow rate and equivalence ratio are maintained, but with no spark ignition).

The PIV method is described by Raffel et al. (2007). The parameter  $\Delta t$ , the time interval between acquisition of the first and second images of a pair, determines the velocity resolution. Experimentation with various values for  $\Delta t$  showed that  $\Delta t = 8 \mu\text{s}$  captured a maximum resolvable speed of 14 m/s, while it reliably recorded speeds as low as 1 m/s. This range contains most of the speeds observed in both non-combusting and combustion flow within the chamber, with the exception of very high speed inlet jets, and is thus used in all PIV data presented herein.

The present chamber design allows for image acquisition in orthogonal cross-sectional planes inside the chamber within a volume measuring  $14 \times 15 \times 8$  mm. The present measurements include two sets of orthogonal planes: 5 planes Parallel to the front window (P1, P2, P3, P4, and P5) and 3 planes Normal to the window (N1, N2, and N3). These sets of planes are denoted by the green lines in Figure 3.3.

The air flow into the chamber is seeded with smoke particles by passing it through a pressurized vessel in which incense is burned. The incense particles are burned off during the COMPACT combustion process, thus allowing for direct visualization of the burned regions (and nominal flame front location) in the images. However, this precludes measuring the flow field behind the flame front and during the refill process before significant flow of fresh seeded air has entered the chamber after combustion.

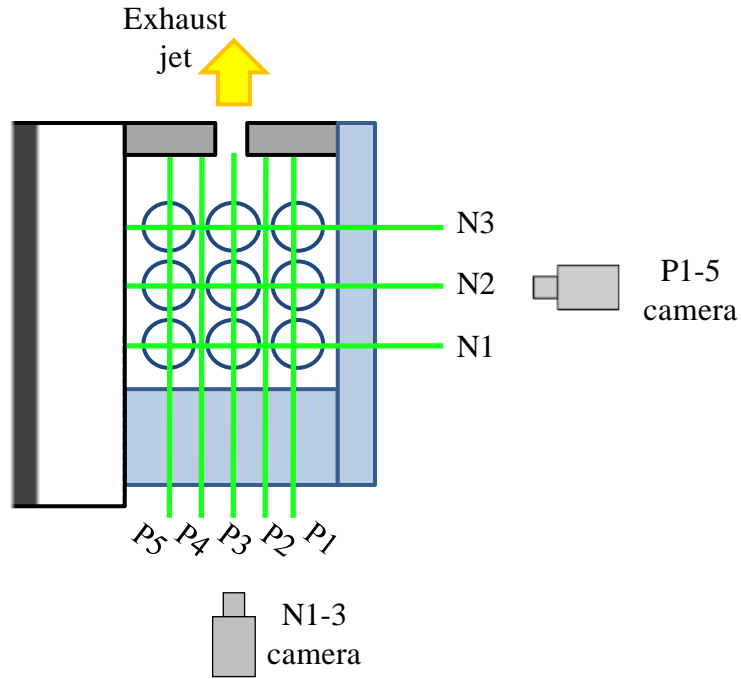
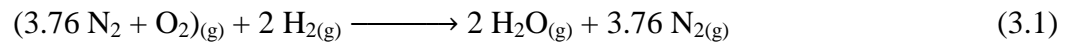


Figure 3.3: PIV camera setup and illuminated planes

### 3.3 Operating Conditions

All the experiments discussed in this document, used air and hydrogen as the oxidizer and fuel respectively. The reaction under stoichiometric conditions is:



The equation assumes that air is composed of 79%  $\text{N}_2$  and 21%  $\text{O}_2$ . The energy released by the reaction is  $E_{comb} = 241.8 \text{ kJ/mol}$  of water produced (Nuffield 1999), and features an overall mole change from 6.76 moles of reactants to 5.76 moles of products. The equivalence ratio is:

$$\Phi = \frac{(m_{fuel}/m_{air})}{(m_{fuel}/m_{air})_{st}} \quad (3.1)$$

$(m_{fuel}/m_{air})$  is the ratio of mass flow rate of fuel to mass flow rate of air, and the subscript  $st$  indicates the stoichiometric fuel-oxidizer ratio.

The actuator was tested over a variety of operating frequencies, equivalence ratios, and flow rates. However, for the PIV measurements in Sections 4.3 and 4.4, and in Chapter 5, the operating conditions were  $f = 5$  Hz,  $\Phi = 0.75$ , and  $Q = 66.7$  std. cm<sup>3</sup>/s (standard centimeters cubed per second – standard denotes conditions at room temperature and pressure). The flow was metered using thermal mass-flow meters, which displayed the rate of flow in SLPM, or standard liters per minute, which was converted to std. cm<sup>3</sup>/s. The use of flow controllers was investigated, but the rapid variations in pressure in the air and hydrogen lines during actuator operation rendered them unreliable.

## CHAPTER 4

### EFFECT OF VARIATION OF AIR INLET JET MOMENTUM FLUX ON ACTUATOR PERFORMANCE

Previous investigations of non-premixed combustion actuators (Crittenden 2003 and Warta 2007) used designs with fuel and oxidizer inlets that were sized to produce “choked” (sonic) jets at the exhaust orifice at most of the flow rate/equivalence ratio combinations tested. The higher momentum air inlet jet exerts the dominant influence on the flow field within the combustion chamber at the equivalence ratios ( $0.5 \leq \Phi \leq 1.0$ ) and inlet diameters tested. It determines the direction of the bulk flow independently of the fuel inlet jet is present or absent (i.e. whether the fuel supply is on or off). The discussions in this Chapter focus on the changes in performance brought about by changing the air inlet diameter,  $d_{air}$ , and thus the momentum of the air jet.

#### 4.1 Overview of Baseline Configuration

The inlet geometry of the chamber discussed in this Chapter features a pair of opposed inlets, with a single exhaust orifice as shown in Figure 4.1 (back plate and windows shown for orientation purposes, cf. Figure 3.2). The inlets are located approximately 13 mm from the exhaust orifice and 2 mm above the base of the chamber. The axes of the three orifices lie in a single plane located 7 mm from the front and rear walls. This configuration was chosen as a starting point because it was assumed that it would result in efficient mixing of reactants and scavenging of exhaust products. The assumption was that the turbulent fuel and oxidizer jets would mix evenly over short time

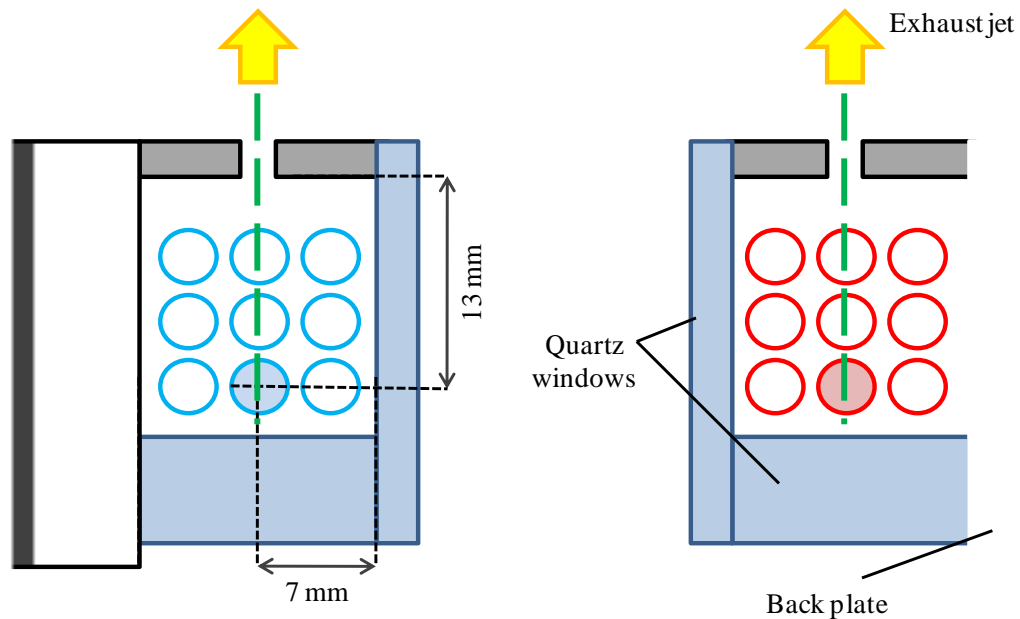


Figure 4.1: Schematic of actuator in baseline configuration, showing arrays of air (left) and fuel (right) inlets. Inlets in use are filled in. The green dashed line shows the plane in which the axes of the inlets and the exhaust orifice lie

scales (less than 0.1 – 1 ms, the convective time scale of the air inlet jet), producing a mixture that would be distributed evenly throughout the chamber over a longer time scale (1 – 10 ms, the time scale of the bulk circulation). The placement of both inlets near the base of the chamber was intended to allow the inflow of fresh reactants to displace combustion products from the bottom of the chamber towards the exhaust orifice at the top and thus to avoid trapping pockets of burnt gases with the fresh reactants. This baseline configuration of air and fuel inlets is compared to other configurations in Chapter 5.

## 4.2 Exploration of Baseline Configuration Performance

This investigation of the baseline configuration focuses on finding relationships between controllable operating conditions, namely the equivalence ratio  $\Phi$ , overall flow rate  $Q$ , and actuation frequency  $f$ , and the parameters that define the performance of the actuator: peak pressure  $p_{max}$ , maximum stable actuation frequency  $f_{max}$ , and total impulse of the actuation jet  $J_1$ . Comparison of the actuator's performance at different flow rates and equivalence ratios shows how variations in performance are connected with energy release during combustion  $E_{comb}$  and air inlet jet momentum  $J_{air}$ .

Testing of the baseline configuration under a variety of conditions has revealed that of the three air inlet orifice diameters tested ( $d_{air} = 0.79, 1.63, \text{ and } 2.92$  mm), the best performance in terms of  $f_{max}$  and  $p_{max}$  is obtained when  $d_{air} = 0.79$  mm. Figure 4.2 shows time traces of phase-averaged (over 50 cycles) combustor pressure (normalized by atmospheric pressure  $p_{atm}$ ) following spark ignition (time is normalized by the refill time  $\tau_{refill} = 1/f_{refill} = V/Q$ ). These traces capture the ignition of the reactant mixture, combustion, and the outflow of burned products that escape due to their resultant increase in volume and displacement by the flow of fresh reactants. The pressure traces are obtained for a range of equivalence ratios  $0.5 \leq \Phi \leq 1.0$  at  $Q = 66.7$  std. cm<sup>3</sup>/s, and an actuation frequency of  $f = 5$  Hz ( $\tau_{refill} = 44.3$  ms,  $f_{refill} = 22.6$  Hz). Assuming that all the fuel undergoes complete combustion, the energy release of the reaction is directly proportional to the equivalence ratio ( $E_{comb} \propto \Phi$ ). Hence, varying the equivalence ratio changes the temperature of the products, the flame speed,  $S$ , and hence the pressure rise due to combustion.

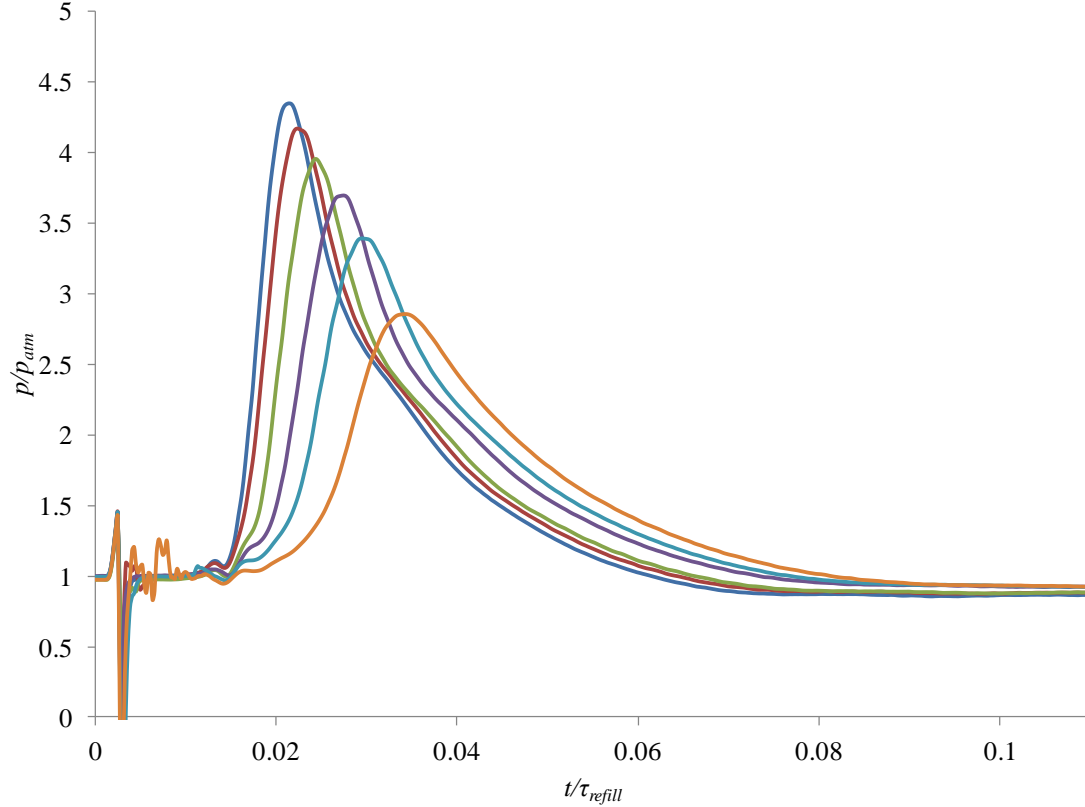


Figure 4.2: Phase-averaged pressure-time traces during combustion,  $Q = 66.7 \text{ s-cm}^3/\text{s}$ ,  $d_{air} = 0.79\text{mm}$ ,  $f = 5\text{Hz}$ ,  $\Phi = 1.0$  (—),  $0.9$  (—),  $0.8$  (—),  $0.7$  (—),  $0.6$  (—),  $0.5$  (—)

Figure 4.2 shows the pressure traces for the above conditions, which are as expected (cf. Figures 2.1 and 2.2, Section 3.1). The noisy transient signals before the main pressure pulses ( $0 < t/\tau_{refill} < 0.15$ ) are due to the high-voltage spark that ignites the mixture. The traces in Figure 4.2 show a number of trends, including decreasing peak pressure and increasing pulse duration with reduced equivalence ratio. These trends will be explained in detail below. As expected,  $\Phi = 1.0$  produces the highest peak pressure because the combustion reaction releases the largest amount of thermal energy into the chamber (highest  $E_{comb}$ ) and thus produces the hottest combustion products, which rapidly expand to produce the transient actuation jet.

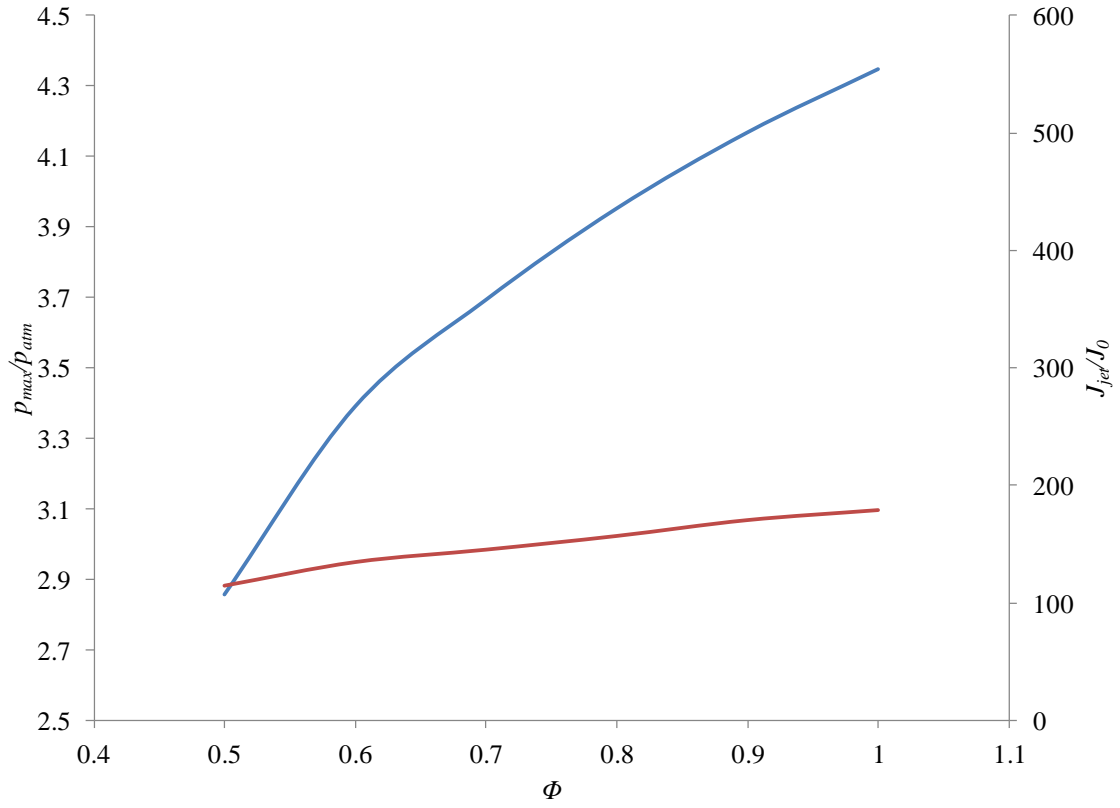


Figure 4.3: Variation of  $p_{max}$  and  $J_I$  with  $\Phi$ ,  $Q = 66.7 \text{ s-cm}^3/\text{s}$ ,  $d_{air} = 0.79\text{mm}$ ,  $f = 5\text{Hz}$ ,  $p_{max}/p_{atm}$  (—),  $J_I/J_0$  (—)

Figure 4.3 shows the variation of the peak pressure inside the chamber and impulse of the actuation jet  $J_I$  with equivalence ratio (extracted from Figure 4.2). The method of calculating  $J_I$  from the pressure traces is described in Section 2.2.3 (Equations 2.1-2.3). The impulse of the actuation jet is normalized by the impulse of the non-combusting flow out of the exhaust orifice,  $J_0 = Q^2 \Delta t_{pulse} \rho_0 / A_{ex}$ , where  $\Delta t_{pulse}$  is the pulse duration and  $\rho_0$  is the density of the unburned reactants.

Figure 4.3 shows that  $p_{max}/p_{atm}$  increases from 2.8 to 4.3 as  $\Phi$  is increased from 0.5 to 1.0. For comparison, adiabatic combustion of air and hydrogen in a constant volume calculated using Gaseq (a chemical equilibrium calculator developed by C.



Morley [2005]; utilized widely e.g.: Black et al. 2007, Bellorio and Pimenta 2005) yields  $p_{max}/p_{atm}$  varying from 6.1 to 8.0 for the same range of  $\Phi$  – a larger absolute change, but a much smaller relative change. This highlights the real-world inefficiencies of the actuator and its variance from the constant-volume adiabatic heat release model.

The actuator's performance is limited by several factors. Heat transfer away from the burning gases into the walls of the combustion chamber results in decreased combustion efficiency. This effect is more pronounced at low actuation frequencies and in the first several cycles before the chamber walls heat up sufficiently. On the other hand, as the wall temperature increases the flame quenching effect decreases. Moreover, the combustor is not a constant volume system. During the initial phases of combustion following ignition as the flame propagates within the combustor and before there is significant flow through the exhaust orifice, the combustion process may be approximated as nearly “constant volume” until approximately  $t/\tau_{refill} = 0.0113$ , or  $t = 0.5$  ms for  $d_{air} = 0.79$  mm in Figure 4.12c. At later times, the exhaust flow is significant and contains both reactants and high temperature combustion products, resulting in incomplete combustion within the chamber and further loss of heat to the ambient. Figure 4.3 also shows that  $J_I$  increases with  $\Phi$ , exhibiting an approximate 56% increase over the range of equivalence ratios tested.  $J_I$  depends on the area under the pressure trace, and while the duration of the pressure pulse decreases with increasing  $\Phi$  (as will be discussed below), the simultaneous increase in  $p$  (and  $p_{max}$ ) results in an overall increase in the impulse.

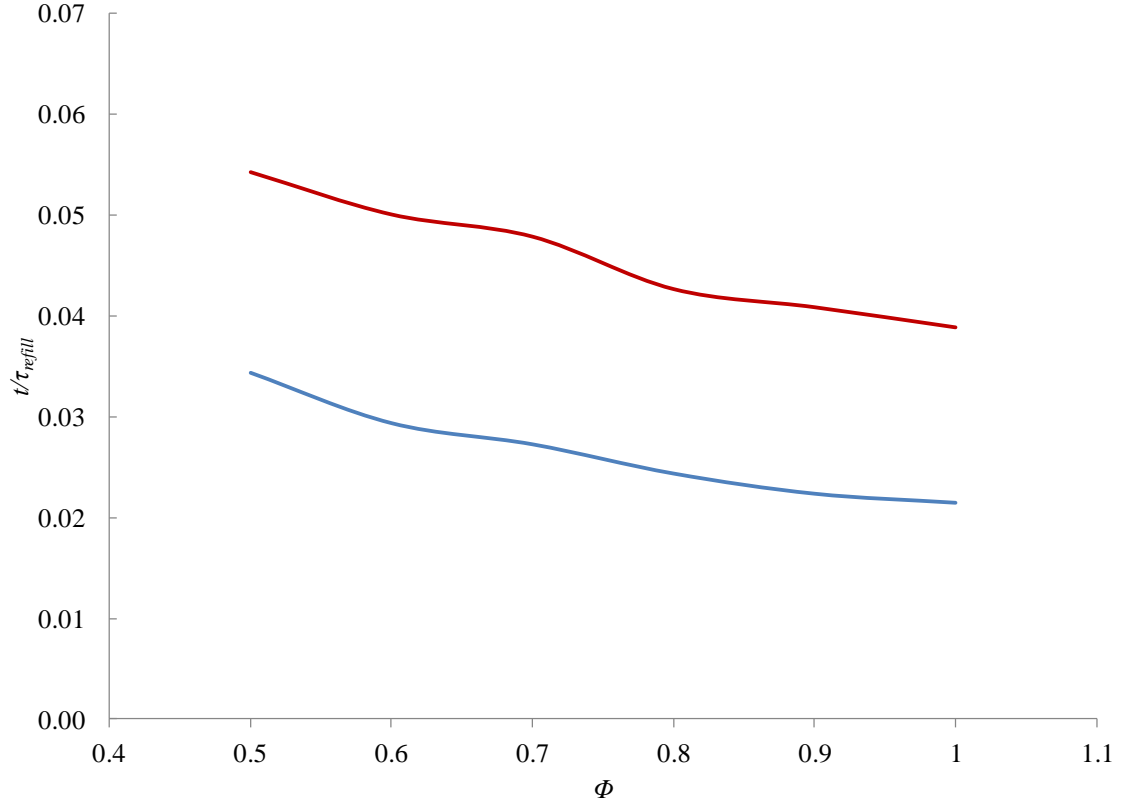


Figure 4.4: Variation of pressure trace timing with  $\Phi$ ,  $Q = 66.7 \text{ s-cm}^3/\text{s}$ ,  $d_{air} = 0.79\text{mm}$ ,  $f = 5\text{Hz}$ ,  $\tau_{refill} = 44.3 \text{ ms}$ ,  $\Delta t_{rise}/\tau_{refill}$  (—),  $\Delta t_{pulse}/\tau_{refill}$  (—)

Figure 4.4 shows that both pressure pulse duration  $\Delta t_{pulse}$  and the rise time of the pulse  $\Delta t_{rise}$  decrease with increasing  $\Phi$  (cf. Figure 2.2 and Section 2.2.2 for formal definitions). The rise time can be related to the flame propagation speed  $S_F$  through the use of an effective radius for the combustion chamber ( $r_{eff} = 8.9 \text{ mm}$ , cf. Section 2.2.2). As shown in Figure 4.4,  $\Delta t_{rise}/\tau_{refill}$  decreases from 0.033 to 0.022 as  $\Phi$  increases from 0.5 to 1.0, which corresponds to an increase in  $S_F$  from 6.0 to 9.3 m/s. Note that  $S_F$  is not the flame speed  $S$  since the flame front is pushed ahead by hot expanding gasses, but the two are related (the higher the local flame speed relative to the products, the faster the rate of propagation through the chamber, cf. Section 2.2.2). Figures 4.13 and 4.17 show that the

flame front is in the “wrinkled laminar” regime (cf. Figures 4.18 and 4.19 for Turbulent Kinetic Energy [TKE] within the combustion chamber). Hence, Equations 2.4 (the turbulent flame speed  $S_T$ ) and 2.5 (laminar flame speed  $S_L$ , which determines  $S_T$ ) can be used to explain the trend in  $\Delta t_{rise}$ : product temperature  $T_b$  increases with  $\Phi$ , resulting in increased flame speeds  $S$  and thus faster flame propagation within the chamber  $S_F$ . As the PIV data in Sections 4.3 and 4.4 shows, these estimates of  $S_F$  are quite close to the actual values. Law (1993) states that  $S_L$  decreases from 2.1 m/s to 0.6 m/s as  $\Phi$  is decreased from 1.0 to 0.5 at  $p = 100$  kPa (approximately 1 atmosphere). Bradley et al. (2006) found that at  $p = 1.0$  MPa (approximately 10 atm.),  $S_L$  decreases to about 1.9 m/s at  $\Phi = 1.0$ , and to 0.3 m/s at  $\Phi = 0.5$ . Calculations of  $S_F$  from the pressure data (cf. Figures 4.4 and 4.9) and PIV data (cf. Figures 4.13 and 4.17) show that the propagation rates are considerably higher than these  $S_L$  values. This is addressed below.

The normalized total pulse duration,  $\Delta t_{pulse}/\tau_{refill}$  decreases from 0.054 to 0.039 as  $\Phi$  is increased from 0.5 to 1.0. The time required for the pressure to relax back to ambient is  $\Delta t_{pulse} - (t_{max} - t_{start})$ . This quantity decreases from 0.039 to 0.032 as  $\Phi$  increases from 0.5 to 1.0, and is due to the behavior of  $p_{max}$ . As  $p_{max}$  increases, the contents of the chamber expand more, resulting in higher mass flow rates through the exhaust during combustion. The faster this high-temperature material leaves the chamber, the sooner pressure decreases.

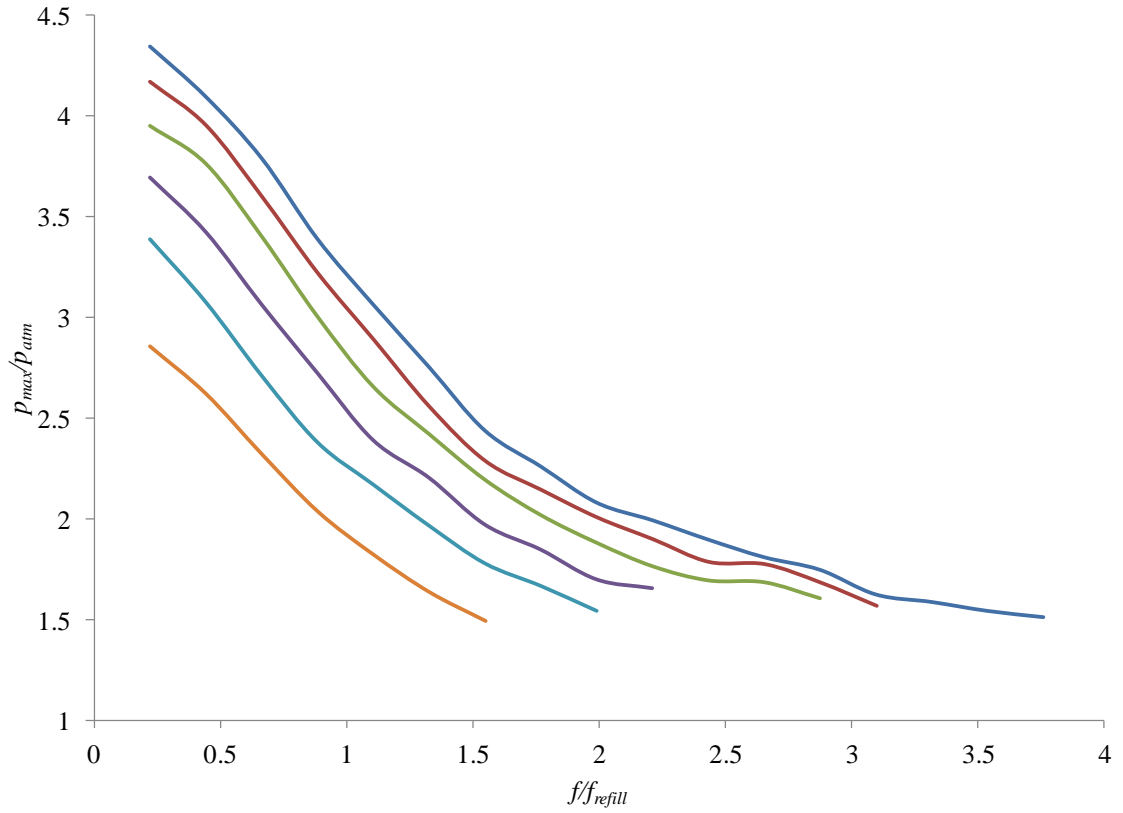


Figure 4.5: Variation of  $p_{max}$  with  $f$ ,  $Q = 66.7 \text{ s-cm}^3/\text{s}$ ,  $d_{air} = 0.79\text{mm}$ ,  $f = 5\text{Hz}$ ,  $\Phi = 1.0$  (—),  $0.9$  (—),  $0.8$  (—),  $0.7$  (—),  $0.6$  (—),  $0.5$  (—)

Figure 4.5 shows the variation of  $p_{max}/p_{atm}$  over a range of operating frequencies from  $f/f_{refill} = 0.221$  ( $f = 5 \text{ Hz}$ ) to  $f_{max}/f_{refill}$ , the highest stable operating frequency, over a range of equivalence ratios  $0.5 \leq \Phi \leq 1.0$  (same as Figures 4.2-4.4). Figure 4.5 shows that the peak pressure decreases as operating frequency is increased for all equivalence ratios, and that the peak stable operating frequency decreases with equivalence ratio ( $f_{max}/f_{refill}$  decreases from 3.76 [85 Hz] for  $\Phi = 1.0$  to 1.54 [35 Hz] for  $\Phi = 0.5$ ). The trend observed in Figure 4.2 where a higher  $p_{max}$  is correlated with increased equivalence ratio is extended here for all frequencies higher than 5 Hz: at a given value of  $f/f_{refill}$ ,  $p_{max}$  increases with  $\Phi$ .

These trends are associated with the effect of  $f$  on the refill process. As shown in Figure 2.2, after the pressure pulse subsides, reactants are free to flow into the chamber, refilling it with fresh charge. The time that it takes for the reactants to displace the remnants of the combustion products and mix is  $\Delta t_{mix}$  (cf. definition in Section 2.2.2), which is determined by the inlet and chamber geometries and the flow conditions. Depending on the actuation frequency, complete mixing may not occur before the next ignition. For all  $f$  such that  $(\Delta t_{mix} + t_{start} + \Delta t_{pulse}) < \tau = 1/f$ ,  $p_{max}$  should ideally remain nearly invariant. When  $(\tau - t_{start} - \Delta t_{pulse}) < \Delta t_{mix}$  the mixing of reactants and/or the evacuation of burned products from previous cycles is incomplete when ignition occurs thereby lowering the effective equivalence ratio,  $\Phi_{eff}$  (the actual ratio of fuel species to non-fuel species divided by the stoichiometric fuel-oxidizer ratio). As  $f$  is increased,  $\Phi_{eff}$  eventually reaches a point where it is no longer equal to  $\Phi$  and instead falls. As a result, the energy released during combustion,  $E_{comb}$  decreases resulting in lower burned temperature  $T_b$ , lower flame propagation speed  $S_F$ , and lower peak pressure  $p_{max}$ . Note that in Figure 4.5 none of the curves are invariant with  $f/f_{refill}$  for any part of the domain. Thus, the first condition above was not achieved in the experiments discussed here.

An estimate for  $\Phi_{eff}$  for an actuator operating at a particular equivalence ratio and frequency can be obtained from Figure 4.5 by assuming that a unique  $p_{max}$  is attained at a given  $\Phi_{eff}$ . For example,  $p_{max}/p_{atm} = 2.86$  both at  $f/f_{refill} = 0.221$  ( $f = 5$  Hz) for  $\Phi = 0.5$ , and at  $f/f_{refill} = 1.33$  ( $f \approx 30$  Hz) for  $\Phi = 1.0$ . This suggests that they share the same  $\Phi_{eff}$ . To find  $\Phi_{eff}$  requires a peak pressure-frequency curve that flattens out for  $p_{max}/p_{atm} = 2.86$  at sufficiently low operating frequencies (i.e.: periods such that  $[\Delta t_{mix} + t_{start} + \Delta t_{pulse}] < \tau$ ). However, as mentioned above, the actuators were not tested at sufficiently low

equivalence ratios and frequencies to produce such a curve. The evidence suggests that for  $p_{max}/p_{atm} = 2.86$ ,  $\Phi_{eff}$  would likely be less than 0.5. It should be noted, however, that comparing different cases in this manner is not strictly comparing like quantities. Two cases with different nominal equivalence ratios and flow rates that produce the same peak pressure would likely have different actual proportions of fuel, air, and burned products in the chamber at the time of ignition. Driving the equivalence ratio lean with cold air vs. a mixture of cold air and burned products would have different effects on the pressure-time history, altering the timing parameters such as  $\Delta t_{rise}$  and  $\Delta t_{pulse}$ . In the current experimental setup, it is impossible to determine the relative abundance of fuel, oxidizer, and combustion products inside the chamber over the actuator's cycle, which would be necessary to determine  $\Phi_{eff}$ .

For all curves in Figure 4.5  $p_{max}$  decreases with  $f$  indicating that  $\Delta t_{mix}$  is already greater than  $\tau$ , and that mixing of reactants and evacuation of products is incomplete. Warta (2007) suggested an idealized model of actuator operation where fuel and oxidizer enter the chamber either premixed or in such a manner that they mix instantaneously. The fuel-oxidizer mixture displaces the extant products of combustion in such a way that no mixing of fresh reactants and products would occur. In this case,  $\Delta t_{mix} = \tau_{refill}$ , and if the mixing time is longer than the refill period then the next combustion cycle involves combustion of proportionately less fuel and oxidizer. The concept is shown in Figure 4.6.

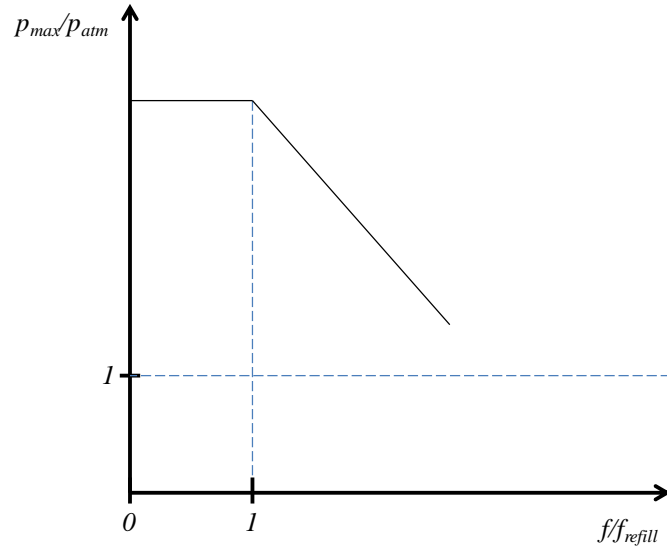


Figure 4.6: Idealized variation of  $p_{max}$  with  $f$ , with instantaneous mixing and perfect scavenging

Because it is assumed that mixing is instantaneous and that combustion products are completely displaced by incoming reactants with no mixing, for  $f \leq f_{refill}$  the combustion chamber contains only fully mixed fuel and oxidizer. For  $f > f_{refill}$ , the proportion of fresh charge in the chamber is equal to the ratio  $\tau/\Delta t_{mix}$ , resulting a linear decrease in peak pressure (due to the linear decrease in energy and products produced by combustion). In the present actuator, mixing of the air and hydrogen only takes place once the two species are in contact and requires finite time. Additional time is taken by advection through the combustion chamber's volume. Moreover, rather than evenly displacing the combustion products from previous cycles, fresh reactants mix with the products to some degree. Thus, the time required to completely scavenge the chamber is considerably longer than in the idealized model, with some products remaining inside and some mixture of combustion products and fresh reactants escaping the chamber through the exhaust orifice. In some cases, there might even be regions of the chamber where

combustion products are trapped for long periods of time. These limitations adversely affect performance, and are affected by the combustion chamber geometry, the placement of the air and hydrogen inlets, the placement of the spark plugs, and the speed/momentum fluxes of the inlet jets.

The reduced effective equivalence ratio  $\Phi_{eff}$  that results when frequency is increased results in lower combustion temperatures, flame propagation speeds, peak pressures (cf. Section 2.2.3). Exacerbating this is the ejection of unburned reactants because of the slow flame propagation (cf. PIV data in Section 4.3), which in turn reduces the total energy released by combustion, further contributing to reduced temperatures and pressures. Figure 4.5 thus shows  $p_{max}/p_{atm}$  decreasing for all tested frequencies, well under  $f/f_{refill} = 1.0$ . Peak pressures continue to decrease with increased operating frequency for all equivalence ratios, until  $p_{max}/p_{atm} \approx 1.5$ . The peak frequency seems to occur when peak pressure is around this value, which may suggest that there is a certain minimum  $\Phi_{eff}$  for which a hydrogen-air mixture combusts, and that the peak pressure at this ratio is approximately  $p_{max}/p_{atm} = 1.5$ .

The previous discussions focused on the effect of  $\Phi$  on actuator performance and hence the energy released during combustion,  $E_{comb}$ . Changing the volumetric flow rate  $Q$  results in higher air jet Reynolds number  $Re_{air} = \frac{\rho_{air}\overline{u_{air}}d_{air}}{\mu_{air}}$  ( $\rho_{air}$  and  $\overline{u_{air}}$  are the density and average velocity of the air jet at the inlet, and  $\mu_{air}$  is the viscosity). This increase is accompanied by an increase in the Turbulent Kinetic Energy (TKE) of the flow within the combustion chamber as shown in Figures 4.18 and 4.19. Changing  $Q$  also results in a shorter refill time,  $\tau_{refill}$ . The effects of these changes are discussed below.



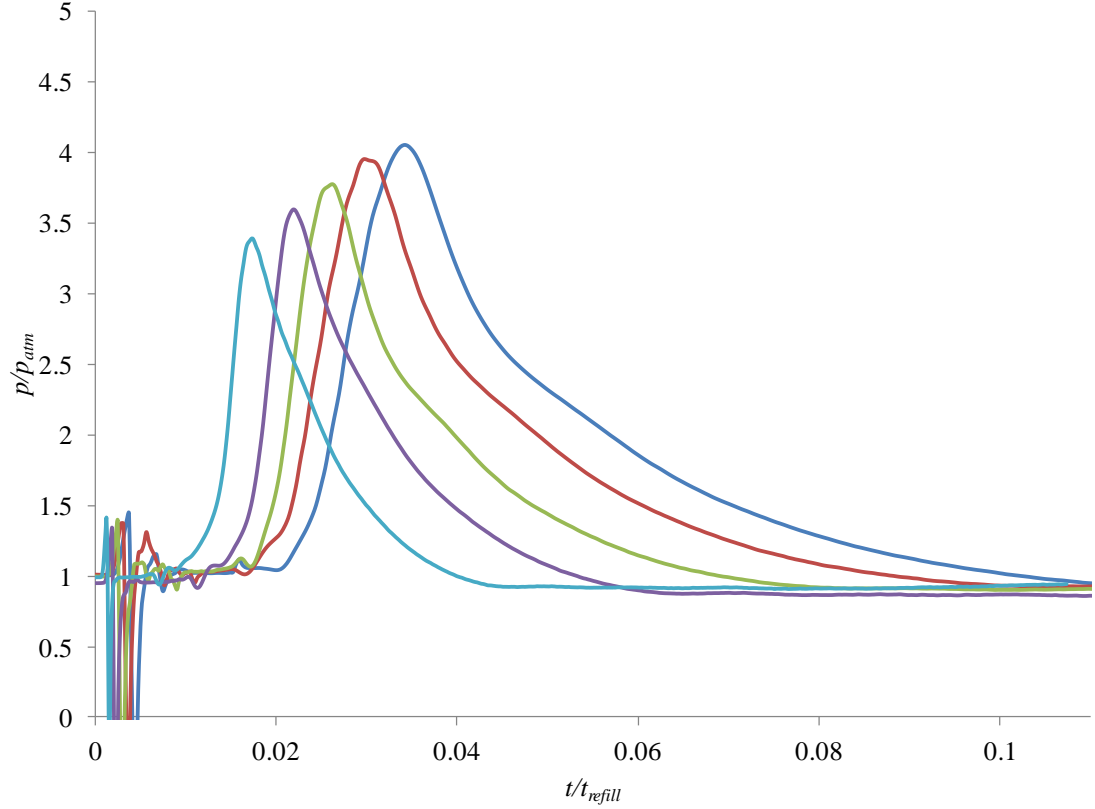


Figure 4.7: Phase-averaged pressure-time traces during combustion,  $\Phi = 0.75$ ,  $d_{air} = 0.79\text{mm}$ ,  $f = 5\text{Hz}$ ,  $Q = 100$  (—),  $80$  (—),  $66.7$  (—),  $50$  (—),  $33.3$   $\text{s-cm}^3/\text{s}$  (—)

Figure 4.7 shows normalized phase-averaged (over 50 cycles) pressure traces during combustion for  $33.3 \leq Q \leq 100$  std.  $\text{cm}^3/\text{s}$  and  $\Phi = 0.75$  ( $f = 5$  Hz and  $d_{air} = 0.79$  mm held constant). Peak pressure occurs when  $Q = 100$  std.  $\text{cm}^3/\text{s}$  (the highest tested), and decreases with flow rate. However,  $t_{max}/\tau_{refill}$  increases with increasing  $p_{max}$ , which is unlike the pressure traces shown in Figure 4.2. Indeed, the overall pulse duration increases with rising flow rate. This is because  $\tau_{refill}$  decreases from 91.7 to 27.3 ms as  $Q$  is increased from 33 to 100 std.  $\text{cm}^3/\text{s}$ . As a result,  $t/\tau_{refill}$  is compressed for higher  $Q$ .

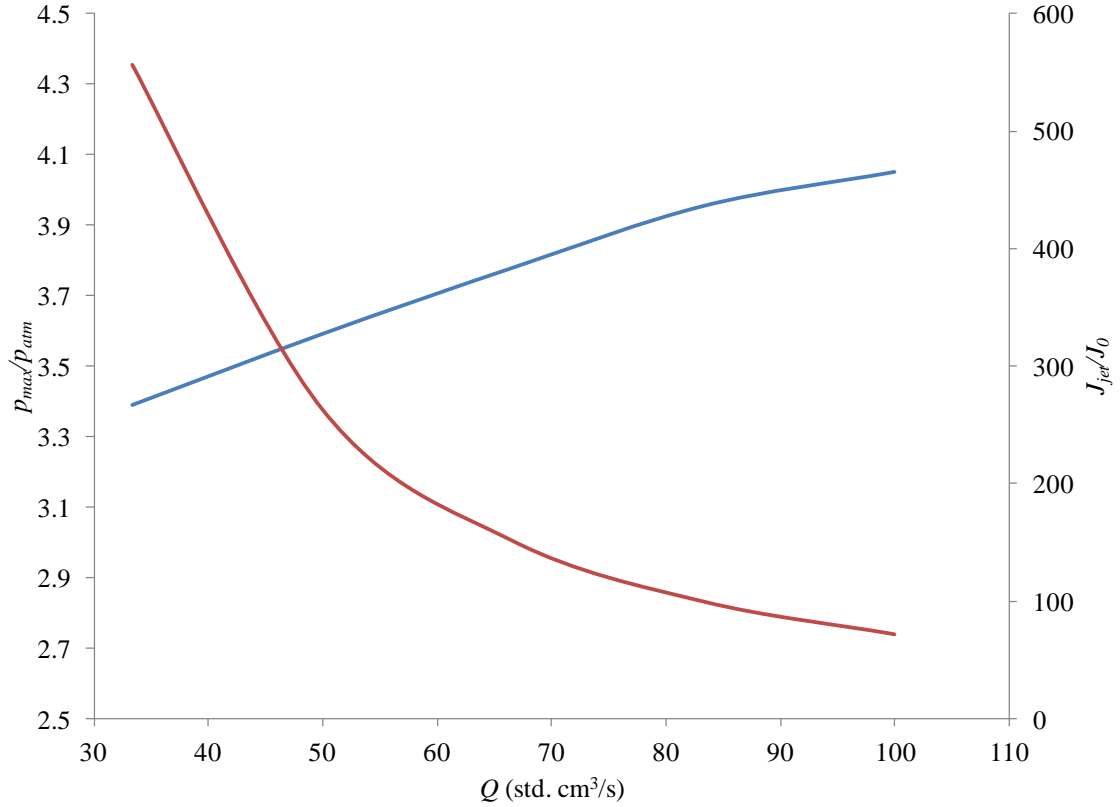


Figure 4.8: Variation of  $p_{max}$  and  $J_I$  with  $Q$ ,  $\Phi = 0.75$ ,  $d_{air} = 0.79\text{mm}$ ,  $f = 5\text{Hz}$ ,  $P_{max}/P_{atm}$  (—),  $J_I/J_0$  (—)

Figure 4.8 is derived from the data in Figure 4.7 and shows that  $p_{max}/p_{atm}$  increases as a result of increased  $Q$ . The air jet Reynolds number  $Re_{air}$  increases with  $Q$  (from 3100 at  $Q = 33.3$  std. cm<sup>3</sup>/s to 9200 at  $Q = 100$  std. cm<sup>3</sup>/s) resulting in greater TKE within the chamber and thus increased flame speed and flame propagation through the chamber (cf. Equation 2.4). As a result, the flame front moves faster through the chamber at higher flow rates and leads to quicker consumption of reactants. Thus, proportionately less fuel is lost through the exhaust orifice during the combustion process and more energy is released within the chamber. Note also that the normalized jet impulse  $J_I/J_0$  decreases with increasing flow rate. This is because, while the impulse of the actuation jet increases

with flow rate due to the increased peak pressure, the impulse of the non-combusting exhaust orifice flow also increases with flow rate, resulting in  $J_1/J_0$  decreases with increasing  $Q$ . Thus, while in absolute terms increasing  $Q$  results in improved performance (higher  $p_{max}$ , higher  $J_1$ ), non-dimensionalizing by  $J_0$  shows that increasing the flow rate is an inefficient way to extract higher impulse, since increasing  $J_0$  essentially means that more fuel is wasted flowing out of the chamber when not combusting.

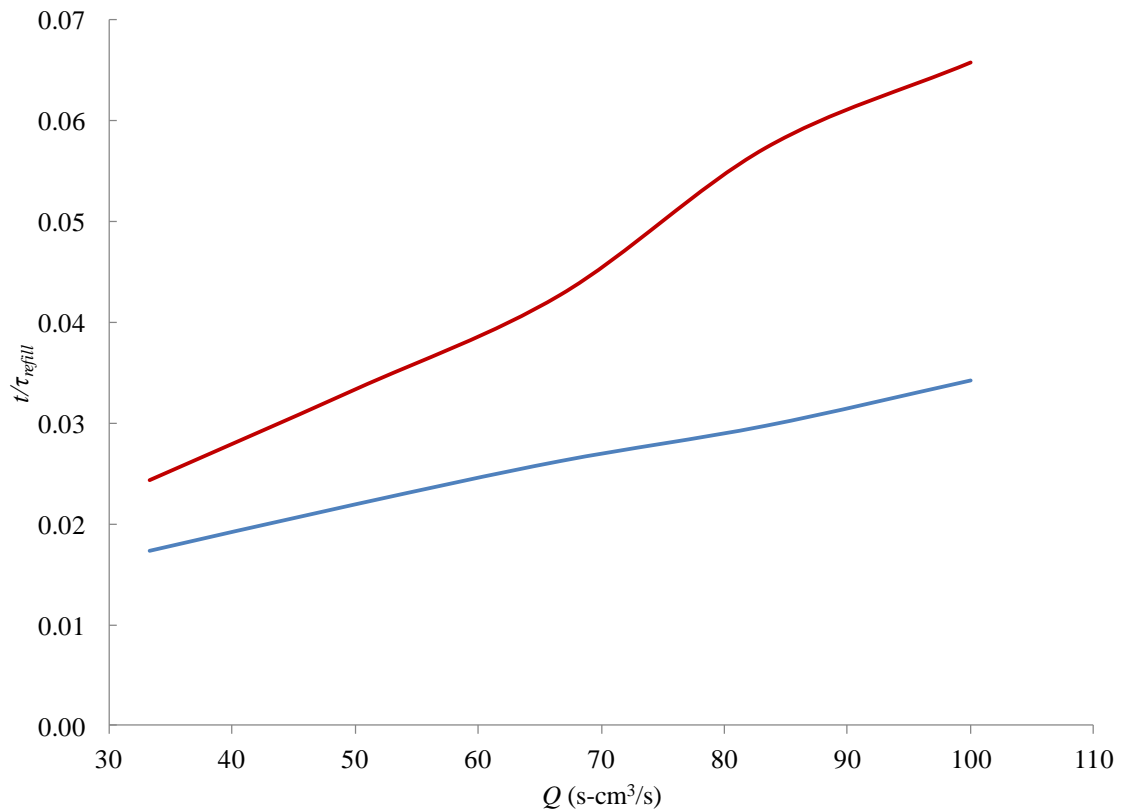


Figure 4.9: Variation of pressure trace timing with  $Q$ ,  $\Phi = 0.75$ ,  $d_{air} = 0.79\text{mm}$ ,  $f = 5\text{Hz}$ ,  $\Delta t_{rise}/\tau_{refill}$  (—),  $\Delta t_{pulse}/\tau_{refill}$  (—)

Figure 4.9 shows the dimensionless timing parameters extracted from Figure 4.7. As is evident from the pressure traces in Figure 4.7, all timing parameters increase with  $Q$  owing to the rapid decrease of  $\tau_{refill}$ , which falls from 91.7 ms at  $Q = 33$  std.  $\text{cm}^3/\text{s}$  to

27.3 ms at 100 std. cm<sup>3</sup>/s.  $\Delta t_{rise}$  decreases from 1.59 to 0.93 ms as  $Q$  is increased, resulting a range of flame propagation speeds  $5.8 < S_F < 8.8$  m/s (which overestimates the flame speed estimated from PIV data). However,  $\Delta t_{rise}/\tau_{refill}$  increases from 0.017 to 0.034 as  $Q$  increases. This is also true of  $\Delta t_{pulse}$  which decreases from 2.3 to 1.8 ms as  $Q$  is increased, but rises when normalized by  $\tau_{refill}$  from 0.024 to 0.066.

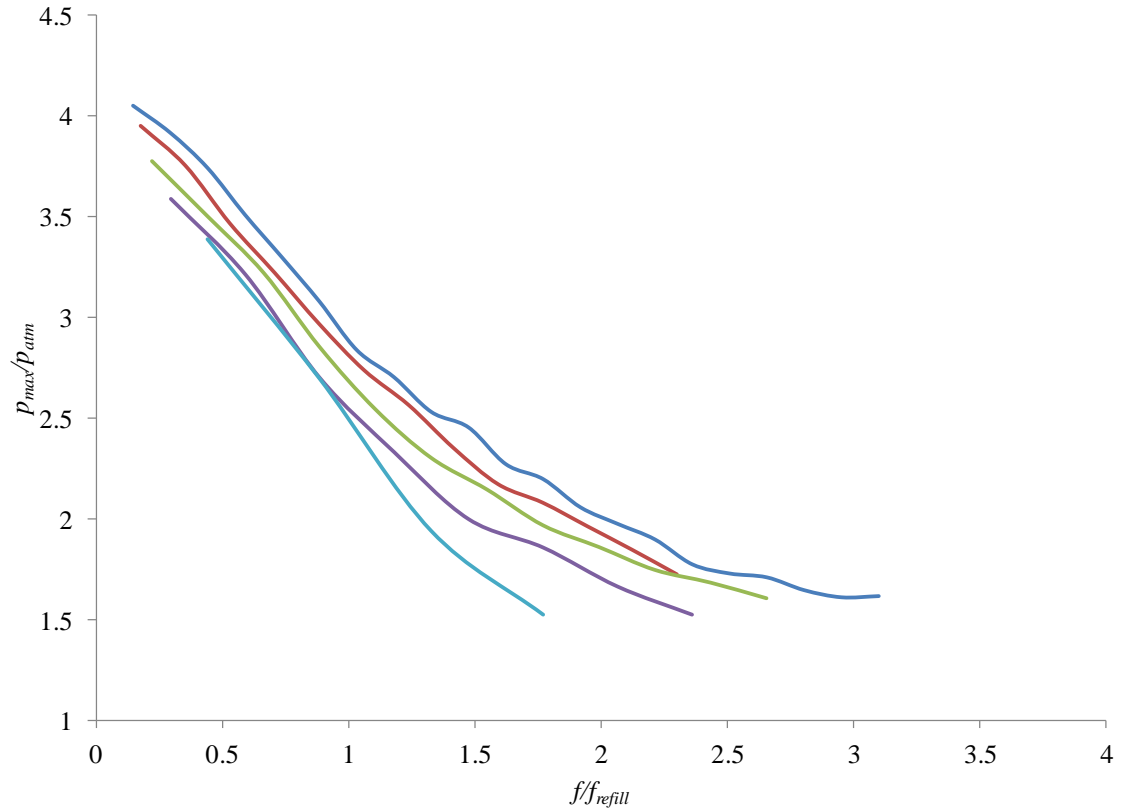


Figure 4.10: Variation of  $p_{max}$  with  $f$ ,  $\Phi = 0.75$ ,  $d_{air} = 0.79$ mm,  $f = 5$ Hz,  $Q = 100$  (—), 80 (—), 66.7 (—), 50 (—), 33.3 s-cm<sup>3</sup>/s (—)

Figure 4.10 shows that the peak pressure can be sustained at higher operating frequencies by increasing the flow rate. This is partly due to the fact that the refill period  $\tau_{refill}$  is shorter at higher flow rates, and partly due to the effect of increased  $Q$  on the intensity of small-scale motion within the chamber. The mass fluxes of each of the inlet

jets are higher at higher  $Q$  such that the chamber is filled more quickly and thus combustion products are displaced more effectively.

For  $f/f_{refill} > 0.75$  the curves diverge as frequency increases, with the distance between adjacent curves increasing as the maximum stable actuation frequency  $f_{max}$  is approached. As in Figure 4.5,  $p_{max}/p_{atm}$  at  $f_{max}/f_{refill}$  tends to be around 1.5, further confirming that this is the lowest sustainable  $p_{max}$ . It is instructive to compare data from Figures 4.5 ( $\Phi = 1.0$ ,  $Q = 66.7$  std.  $\text{cm}^3/\text{s}$ ) and 4.10 ( $\Phi = 0.75$ ,  $Q = 80$  std.  $\text{cm}^3/\text{s}$ ) as for both of these the flow rate of hydrogen  $Q_{H_2} = 20$  std.  $\text{cm}^3/\text{s}$ . For the latter, at  $f = 5$  Hz ( $f/f_{refill} = 0.177$ )  $p_{max}/p_{atm} = 3.95$  and  $f_{max} = 65$  Hz ( $f/f_{refill} = 2.30$ ), while for the former, at  $f = 5$  Hz ( $f/f_{refill} = 0.221$ )  $p_{max}/p_{atm} = 4.35$  and  $f_{max} = 85$  Hz ( $f/f_{refill} = 3.76$ ). Even though  $Q_{H_2}$  in both cases is similar the operation at higher  $\Phi$  and lower  $Q$  produces both higher  $p_{max}$  at all actuation frequencies and higher  $f_{max}$ . This comparison shows that while increasing the overall flow rate improves actuator performance in terms of peak pressure and maximum actuation frequency because of the increase in both the TKE and the speed of the scavenging process, doing so by maintaining the fuel flow rate and increasing the equivalence ratio (by decreasing the flow rate of the air) allows the actuator to achieve even higher peak pressure and maximum frequency, making more efficient use of the fuel available.

The experiments where  $Q$  and  $\Phi$  were changed raise the question of whether the flame propagation speed  $S_F$  is influenced more by the reaction kinetics and thermodynamics or the gas expansion behind the flame front. In the present experiments, these effects are not decoupled, but it is possible to infer a relationship. Law (1993) states that the laminar flame speed  $S_L$  increased from 0.6 to 2.1 m/s as  $\Phi$  increased from 0.5 to

1.0 at standard temperature and pressure. This change is due entirely to the change in the chemical properties of the flow, which results in a change in the burned temperature,  $T_b$  (cf. Equation 2.5). The values for  $S_F$  calculated both from the pressure and PIV data are considerably (2-3 times) higher, which suggests that the dominant influence upon the flame front in the actuator's combustion chamber is the expansion of burned gases behind it. However, in terms of the changes in performance, it appears that doubling  $\Phi$  resulted in an increase in  $S_F$  of approximately one half (6 to 9 m/s), while tripling  $Q$  resulted in a similar increase in  $S_F$ , both in terms of percentage and magnitude. As such, it appears that the reaction kinetics have a stronger influence on the propagation of the flame front than the flow properties, at least at low actuation frequencies.

Experiments with spherical bombs have been conducted to determine the laminar flame speed  $S_L$  for hydrogen-air mixtures, accounting for the influence of flame stretching and gas expansion behind the flame in determining  $S_L$  (Milton and Keck 1984, Dowdy et al. 1990, Lamoureux et al. 2003). For these purposes it is interesting to consider the values of flame propagation speed  $S_F$  attained in the spherical bomb investigations. Lamoureux et al. (2003) showed that while the laminar flame speeds were similar to those stated by Law (1993), the actual average speed of the flame relative to the chamber walls was approximately 12 m/s, which is considerably higher than the speeds obtained in the present experiments. This discrepancy may be attributed to the fact that unlike the present actuator, the spherical bomb is essentially a constant volume.

## 4.3 Flow Visualization of Baseline Configuration Actuator Undergoing

### Combustion ( $d_{air} = 0.79$ mm)

The data presented in this section comprises pressure traces and PIV images that show how the actuator performs when of  $d_{air} = 0.79$  mm,  $Q = 66.7$  std. cm<sup>3</sup>/s,  $\Phi = 0.75$ , and  $f = 5$  Hz. The PIV data has been presented in the form of vector fields, TKE fields, and contrast-enhanced images of the flow (visualized by Figures 4.11-4.13 and 4.15-4.17), and are used to understand the internal flow field of the actuator and how it affects the performance as measured by pressure traces (cf. Figure 4.7, data for  $Q = 66.7$  std. cm<sup>3</sup>/s).

#### 4.3.1 Non-Combusting Flow Field

Figure 4.11 shows the flow field within the combustion chamber in the absence of combustion, as measured using PIV (cf. Section 3.2). Data was collected for two orthogonal sets of planes: those Parallel to the front window of the actuator (P1, P2, P3, P4, and P5) in Figure 4.11a, and those Normal to the front window (N1, N2, and N3) in Figure 4.11b (cf. Figure 3.3). Planes P1–5 are  $15 \times 14$  mm ( $x$ - $y$  planes), while planes N1-3 are  $14 \times 14$  mm ( $x$ - $z$  planes). Both sets show velocity vectors as well as contours of velocity magnitude. The actuation and air inlet jets are marked by the orange and blue arrows. The gray regions within the PIV images show domains where the flow cannot be resolved (cf. Section 3.2), or where the light sheet is blocked by the spark plugs. This non-combusting flow field can be considered as being nominally equivalent to that of the late stages of the refill process at low actuation frequencies.

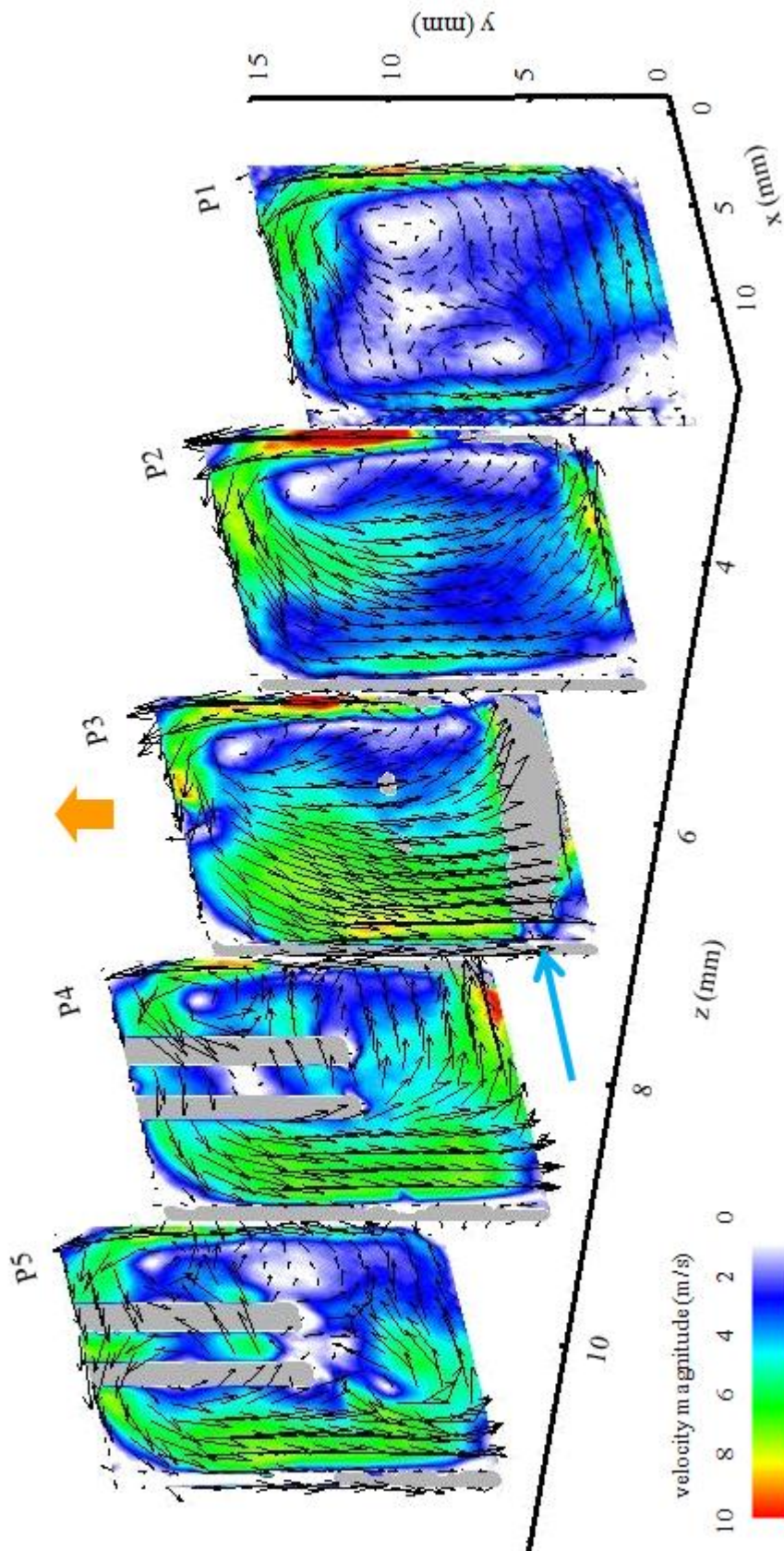


Figure 4.11a: Planar PIV cross-sections of the non-combusting flow field, Planes P1-5,  $d_{air} = 0.79$  mm  $Q = 66.7$  s-cm<sup>3</sup>/s,  $\Phi = 0.75$  and  $f = 5$ Hz



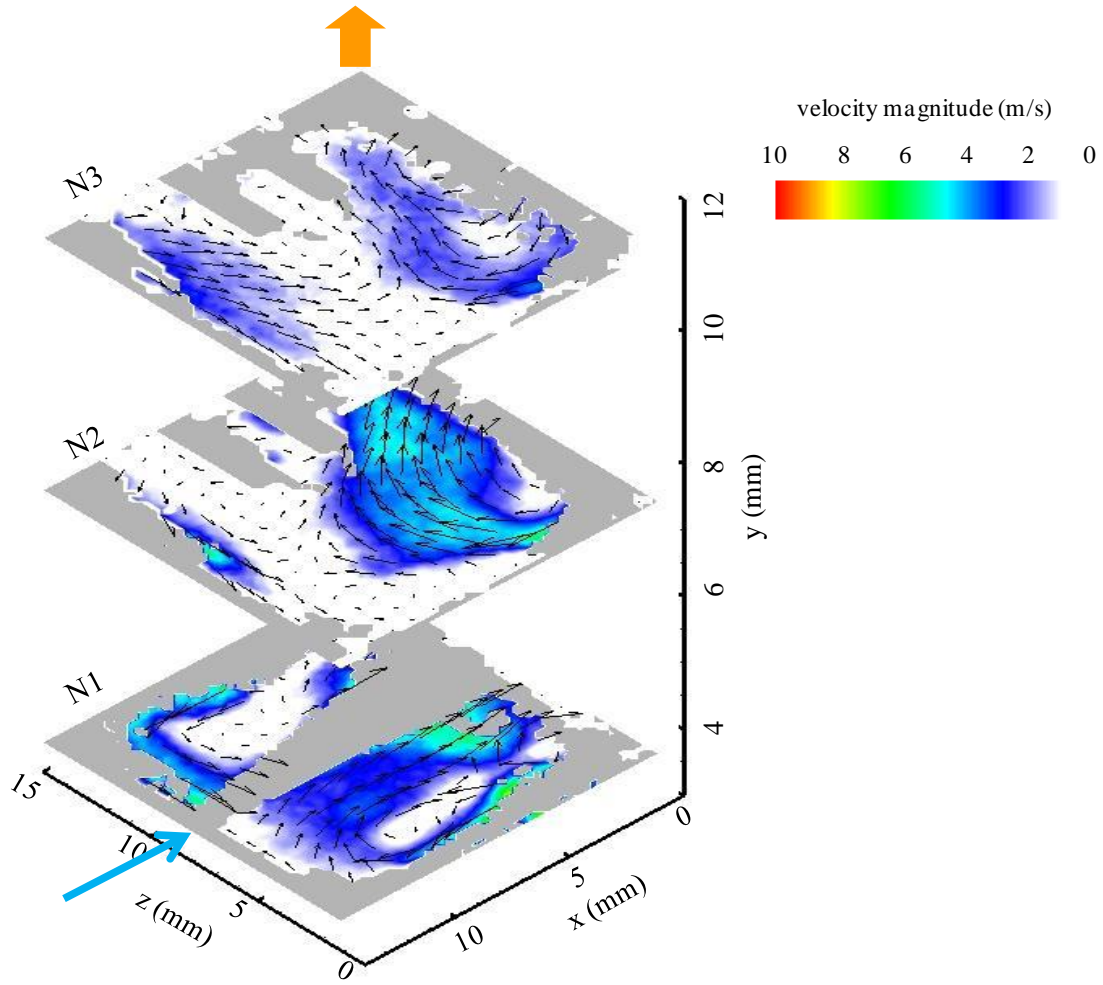


Figure 4.11b: Planar PIV cross-sections of the non-combusting flow field, N1-3,  $d_{air} = 0.79 \text{ mm}$   $Q = 66.7 \text{ s-cm}^3/\text{s}$ ,  $\Phi = 0.75$  and  $f = 5\text{Hz}$

These data show that the motion within the chamber is dominated by the air inlet jet. The outline of the jet can be clearly seen in the bottom left corner of plane P3, and is marked by the absence of data because the PIV settings are used to resolve the lower speeds observed in the majority of the chamber's volume ( $0.5 \leq u \leq 12 \text{ m/s}$ , cf. Section 3.2). The average speed of the air jet at the orifice is 104 m/s, and its momentum flux is about 28 times that of the hydrogen jet, which has an average speed of 30 m/s. Because of the position of the hydrogen inlet (directly opposing the air inlet) and

the significant difference in momentum fluxes, the penetration of the hydrogen jet into the chamber is small, and the majority of mixing takes place near the fuel inlet where the hydrogen stream is advected by the air flow.

The position of the air inlet at the bottom left corner of the central plane causes the jet to impinge on the opposite wall (Figure 4.11, P3) and circulate around the chamber. In planes P1–5, the bulk flow moves counter-clockwise (CCW) around the perimeter of the chamber. Data in the plane of the air jet show strong entrainment (approximately 8-9 m/s) of the bulk flow back into the jet as it circulates around. This circulation is strongest along the left wall of the chamber ( $x = 14$  mm).

This bulk CCW circulation pattern is also observed farther away from the air inlet in planes P1 and P2, although the induced velocities are significantly lower. While entrainment towards the jet still exists, the flow speeds are approximately 4 m/s or less, around half those in the corresponding location in P3. In P4 and P5, the flow field is partially masked by the spark plugs that protrude about 6 mm from the rear surface of the chamber. The presence of the spark plugs somewhat alters the circulation induced by the air jet in the rear of the chamber ( $z \geq 8$  mm), causing secondary flows in plane P5. Furthermore, while slowing of the bulk flow is also observed in P4 and P5, the blockage caused by the presence of the spark plugs appears to accelerate the flow, resulting in higher flow speeds around the perimeter of the chamber than in P1 and P2.

Planes N1, N2, and N3 also show the dominant influence of the air jet (inlet located in N1) upon the bulk flow in the chamber. These cross-sections show that the impingement of the air jet on the opposite wall creates two distinct counter-rotating circulation domains on either side of the jet, with regions of high velocity around the

perimeter of the chamber. The planes N2 and N3 show that the bulk flow weakens significantly towards the top of the chamber (as  $y$  increases), with the counter-rotating domains vanishing in N3. This is likely due to the protrusion of the spark plugs from the rear wall of the chamber, which disrupts the flow field. These data indicate that the CCW circulation in P1-5 is combined with the pattern in N1-3.

#### 4.3.2 Combusting Flow Field Evolution

Figure 4.12 shows PIV data for evolution of the flow field during the combustion process. The pressure trace for this case is shown in Figure 4.7 (—,  $d_{air} = 0.79$  mm,  $Q = 66.7$  s-cm<sup>3</sup>/s,  $\Phi = 0.75$ ,  $f = 5$  Hz). Spark ignition occurs at  $t/\tau_{refill} = 0$ , and the pressure rises steeply, peaking at  $P_{max}/P_{atm} = 3.75$  at  $t/\tau_{refill} = 0.026$ , after which there is a relatively slow relaxation down to atmospheric conditions.

At  $t = 0.1$  ms following spark ignition ( $t/\tau_{refill} = 0.002$ , Figure 4.12a), the flow field resembles the non-combusting flow (Figure 4.11) although build-up of radicals and heat transfer to the nucleus of ignition are presumably underway. By 0.3 ms ( $t/\tau_{refill} = 0.007$ , Figure 4.12b), the combustion process has begun, as is evidenced by the presence of the flame front at the center of P3. As noted in Chapter 3, the smoke particles close to the spark plugs are consumed by the combustion, and therefore the flame front is characterized by the absence of PIV data (the flame front is easily visible in instantaneous data and images of the combustion process). Owing to the expansion associated with the flame front, the fluid in its immediate vicinity starts moving away towards the walls of the chamber. However, the flame has not grown enough to be present or to produce significant changes in the adjacent planes P2 and P4.

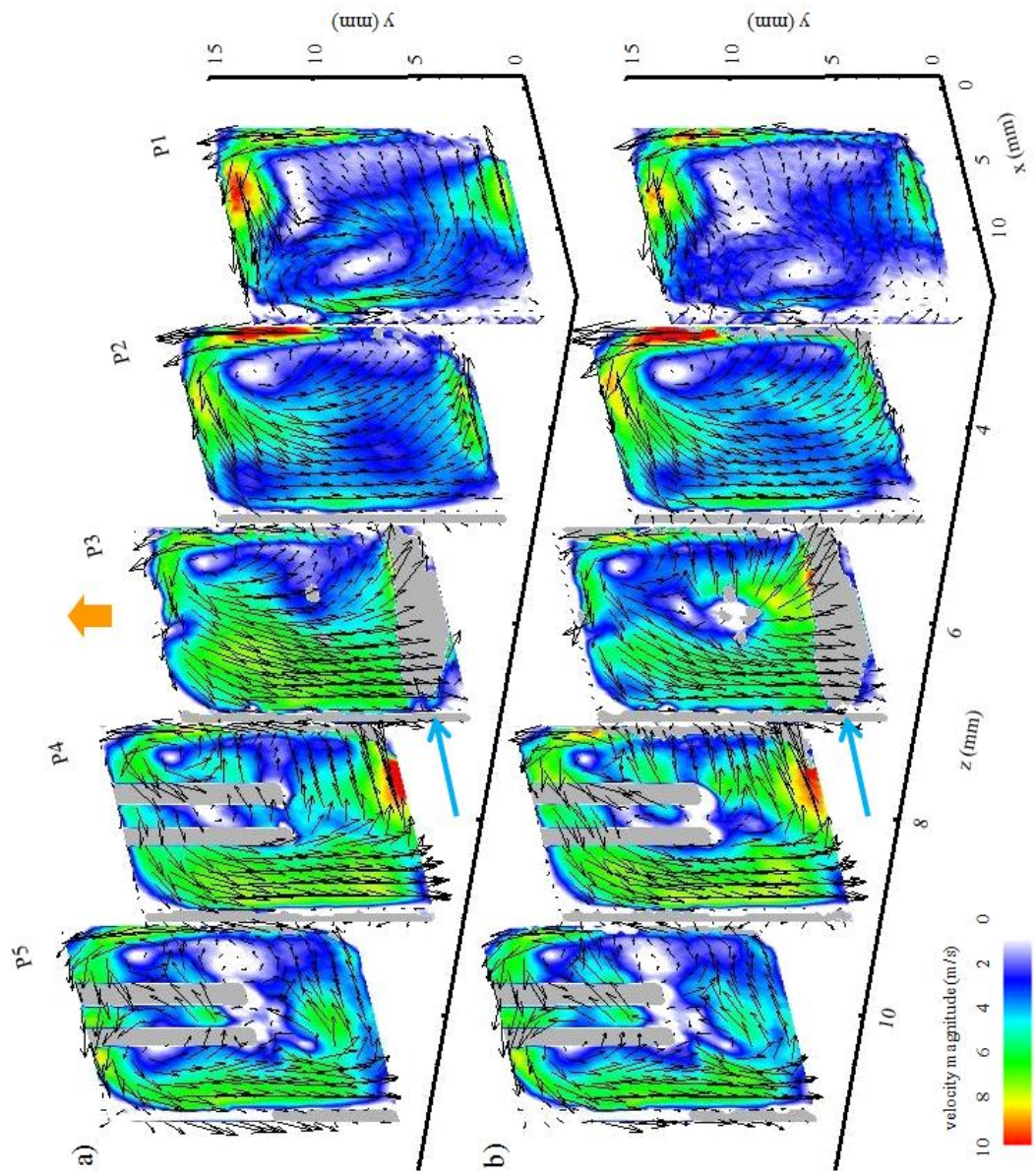


Figure 4.12: Planar PIV cross-sections of the combustor flow field,  $d_{air} = 0.79$  mm,  $Q = 66.7$  s-cm<sup>3</sup>/s,  $\Phi = 0.75$  and  $f = 5$  Hz, a)  $t = 0.1$  ms ( $t/\tau_{refill} = 0.002$ ) and b)  $0.3$  ms ( $0.007$ )

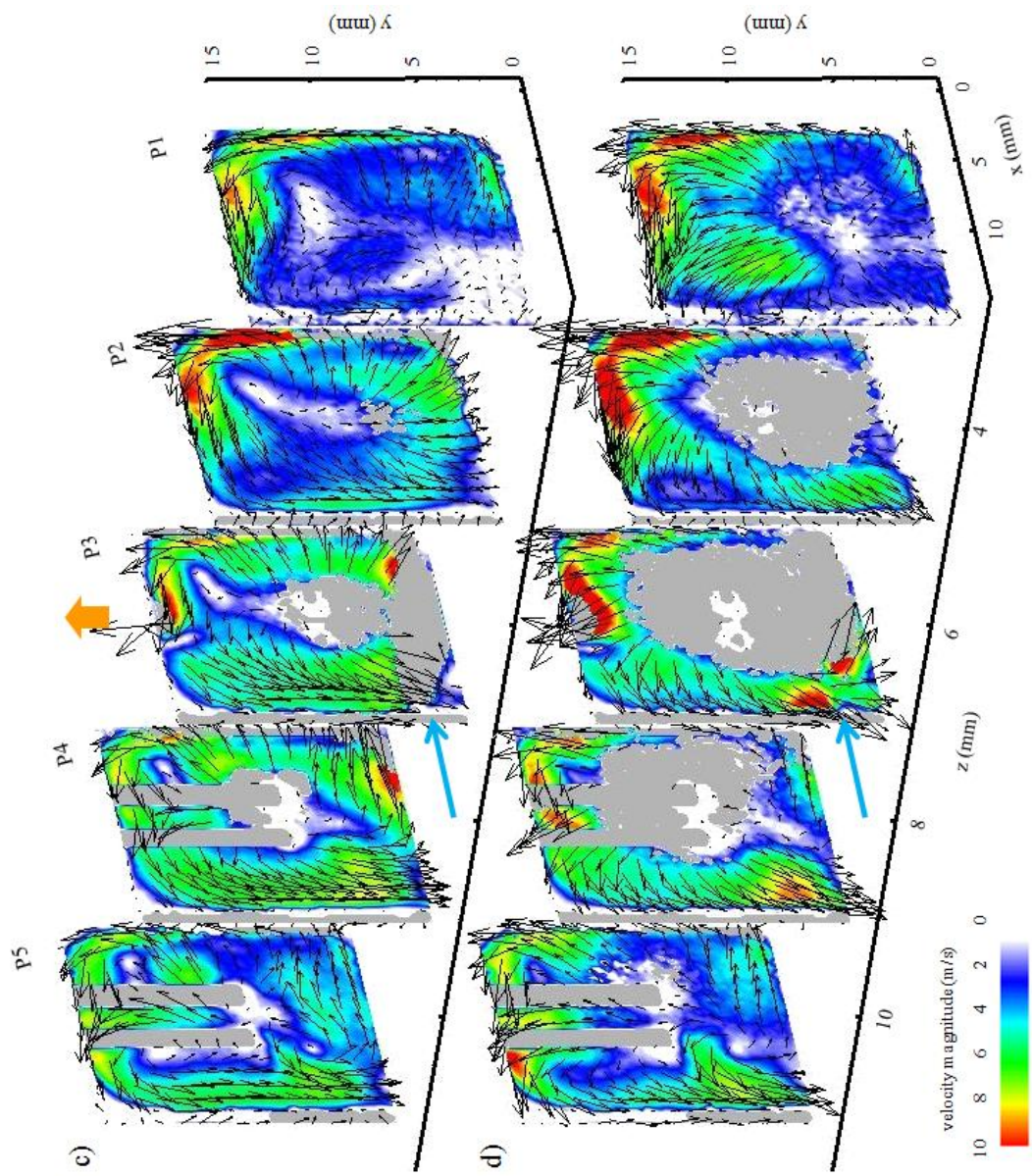


Figure 4.12: Planar PIV cross-sections of the combustor flow field,  $d_{air} = 0.79$  mm,  $Q = 66.7$  s-cm<sup>3</sup>/s,  $\Phi = 0.75$  and  $f = 5$  Hz, c)  $t = 0.5$  ms ( $t/\tau_{refill} = 0.011$ ), and d)  $0.7$  ms ( $0.016$ )

By 0.5 ms ( $t/\tau_{refill} = 0.011$ , Figure 4.12c), the flame front has grown sufficiently large to effect more pronounced changes, and an expansion of the burned region into P4 is observed with accompanying acceleration of the flow towards the edges of the chamber, disrupting the circulatory global flow field. In P3, growth of the flame front continues, as it propagates preferentially towards the bottom-right of the chamber, where the air and hydrogen streams nominally coincide. It is presumably in this region that local flame speed is highest, due to the existence of the most favorable local equivalence ratios where mixing occurs. The flame also propagates faster towards the rear of the chamber, where the spark plugs are located, than towards the front. This difference in flame propagation speeds is likely due to the increased speed of circulation in P4 and P5: the higher flow velocities towards the rear of the chamber result in better mixing of fuel and oxidizer, increased small-scale motion, as well as greater entrainment pulling the flame in that direction. By comparison, the flow velocities towards the front of the chamber (P1 and P2) are considerably lower, and hence the flame propagation there is slower.

As the flame front grows ( $t > 0.5$  ms,  $t/\tau_{refill} > 0.011$ ), flow through the exhaust orifice (located in P3, cf. Figure 4.11), increases and by 0.7 ms ( $t/\tau_{refill} = 0.016$ , cf. Figure 4.12d) the region of flow moving towards the exhaust orifice increases in volume. By this time, the flame front disrupts the circulatory flow driven by the air jet in all planes except P1 and P5, and the general motion of the fluid is away from the expanding flame front, towards the walls of the chamber. For  $t < 0.7$  ms, the pressure inside the chamber remains relatively unchanged ( $p/p_{atm} \approx 1$ , cf. Figure 4.7). After this point, it begins to rise rapidly. Note that the air jet ceases due to the build-up of back pressure in the chamber. For times

longer than 0.7 ms, the vector fields of P3, P4, and P5 are largely blank, and most of the seed particles vanish (not shown here).

The flame propagation speed,  $S_F$ , can be estimated from images showing the progression of the flame front, using (for simplicity) only images of the central plane P3. From the PIV data, it seems that the flame front is roughly spherical. By calculating the area of region consumed by the flame in a particular image at a particular time, it is possible to compute  $r_{eff}$ , the effective radius of a circle with the same area. This  $r_{eff}$  can be approximated as the effective radius of a sphere centered at the spark plugs in the middle of P3. Using this approximation and calculating  $r_{eff}$  for a number of images over a number of time steps it is possible to show how  $r_{eff}$  grows during the combustion process. The mean slope of this distance-time plot is the average speed. Ten randomly selected images are used for each time step. The flame front is then located manually and image processing is used to determine the area consumed by the flame.

Figure 4.13 shows the progression of the flame front. The chart (Figure 4.13c) shows how  $r_{eff}$  varies with time, while two images of the flame in plane P3 are used as examples of how the flame front appears at two different times. Figure 4.13a shows the flame front 0.3 ms after spark ignition, while Figure 4.13b shows the flame at 0.5 ms. There is obviously growth occurring between the two images, but what is more important is that wrinkling of the flame front that can be seen in both images. In Section 4.2 it was stated that the flame front is in the “wrinkled laminar” regime of turbulent flame propagation, which is confirmed by Figures 4.13a and b. The presence of wrinkling is indicative of more intense small-scale motion within the combustion chamber, resulting in a higher flame propagation speed (cf. Section 2.2.3), which is the obtained from the

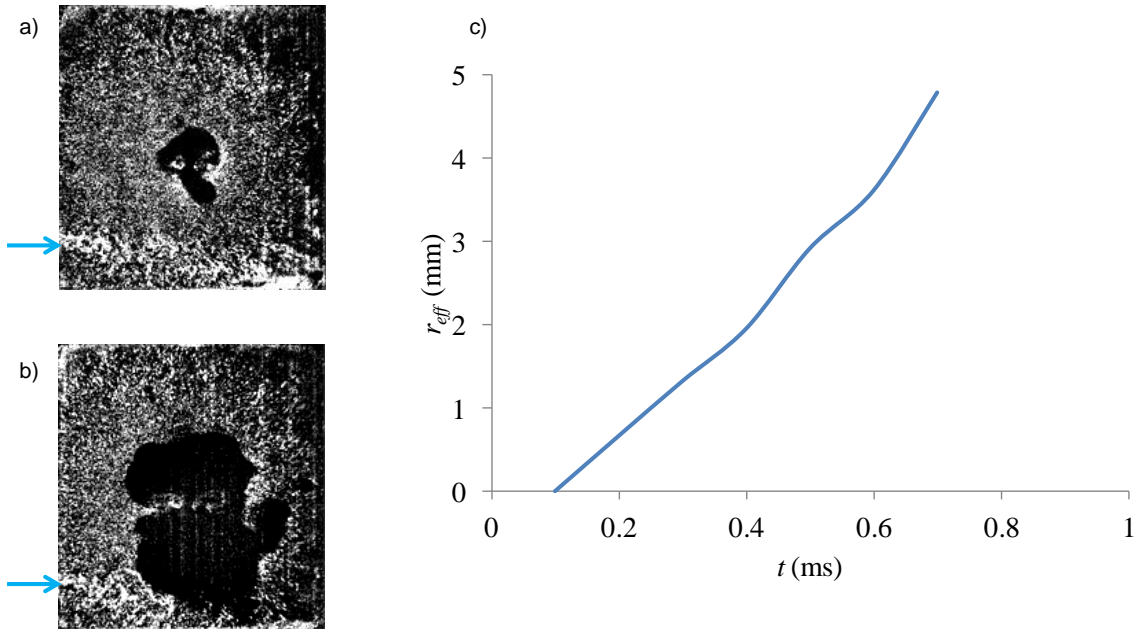


Figure 4.13: Images showing propagation of the flame front in the central plane P3 at a)  $t = 0.3$  ms and b) 0.5 ms after spark ignition, and c) the change in  $r_{eff}$  with time. The blue arrows mark the location of the air inlet.

slope of the plot in Figure 4.13. Using a linear fit,  $S_F$  is found to be around 7.8 m/s, and by 0.7 ms after spark ignition, the flame consumes around 32% of the combustion chamber's volume. This flame speed computed here is slightly higher than that calculated using the rise time of the pressure pulse ( $\sim 7.6$  m/s for  $\Phi = 0.75$ ,  $Q = 66.6$  std  $\text{cm}^3/\text{s}$ ,  $f = 5$  Hz, cf. Section 4.2, Figure 4.9). It is important to note that the speed calculated from plane P3 is an overestimate of the mean flame speed in the chamber because, as noted above, the flame travels more slowly in P1, P2 P4, and P5. Note also that the value for flame propagation speed is in turn four times higher than the values for  $S_L$  in Section 4.2. The effect of small-scale motion on flame speed is part of the explanation, but another important factor is that the burned gasses are expanding, pushing the flame front ahead of them faster than  $S_L$  or  $S_T$ . Figure 4.12 shows that the fluid ahead of the flame front moves



at approximately 6 m/s. If the flame front is being pushed by the expanding hot gasses behind it, then  $S_T \approx 1.8$  m/s, which is closer to the quoted values for flame speed (Law 1993;  $S_L = 2.1$  m/ ).

#### 4.4 Changes in Actuator Performance due to Variation of Air Inlet Jet

##### Momentum Flux

It was hypothesized that increasing the diameter of the air inlet for a given flow rate could help improve the efficiency of the refill process by more effective displacement of the combustion products from previous cycles with less mixing between products and reactants, and by allowing deeper penetration of the hydrogen jet into the chamber, thus allowing mixing between the reactants to occur over a larger area. However, these hypotheses proved to be incorrect, as explained below.

Figure 4.14 shows the phase-averaged pressure traces for  $f = 5, 10,$  and  $15$  Hz for  $d_{air} = 1.63$  and  $2.92$  mm. The traces exhibit qualitatively similar behavior, namely as  $f$  is increased, peak pressure,  $p_{max}/p_{atm}$  diminishes, and pressure pulse duration,  $\Delta t_{pulse}$  lengthens. As shown in Table 1, compared to  $d_{air} = 0.79$  mm, the two cases discussed here show reduced peak pressures ( $p_{max}$  for  $d_{air} = 1.63$  mm is 11% lower than for  $d_{air} = 0.79$  mm, while  $d_{air} = 2.92$  mm is 39% lower). The table compares the performance of the chamber with the three different air inlet diameters. The average speed of the air jet at the inlet is  $\overline{u_{air}}$ , and the momentum flux ratios are computed relative to the hydrogen jet (which always has the same average speed).

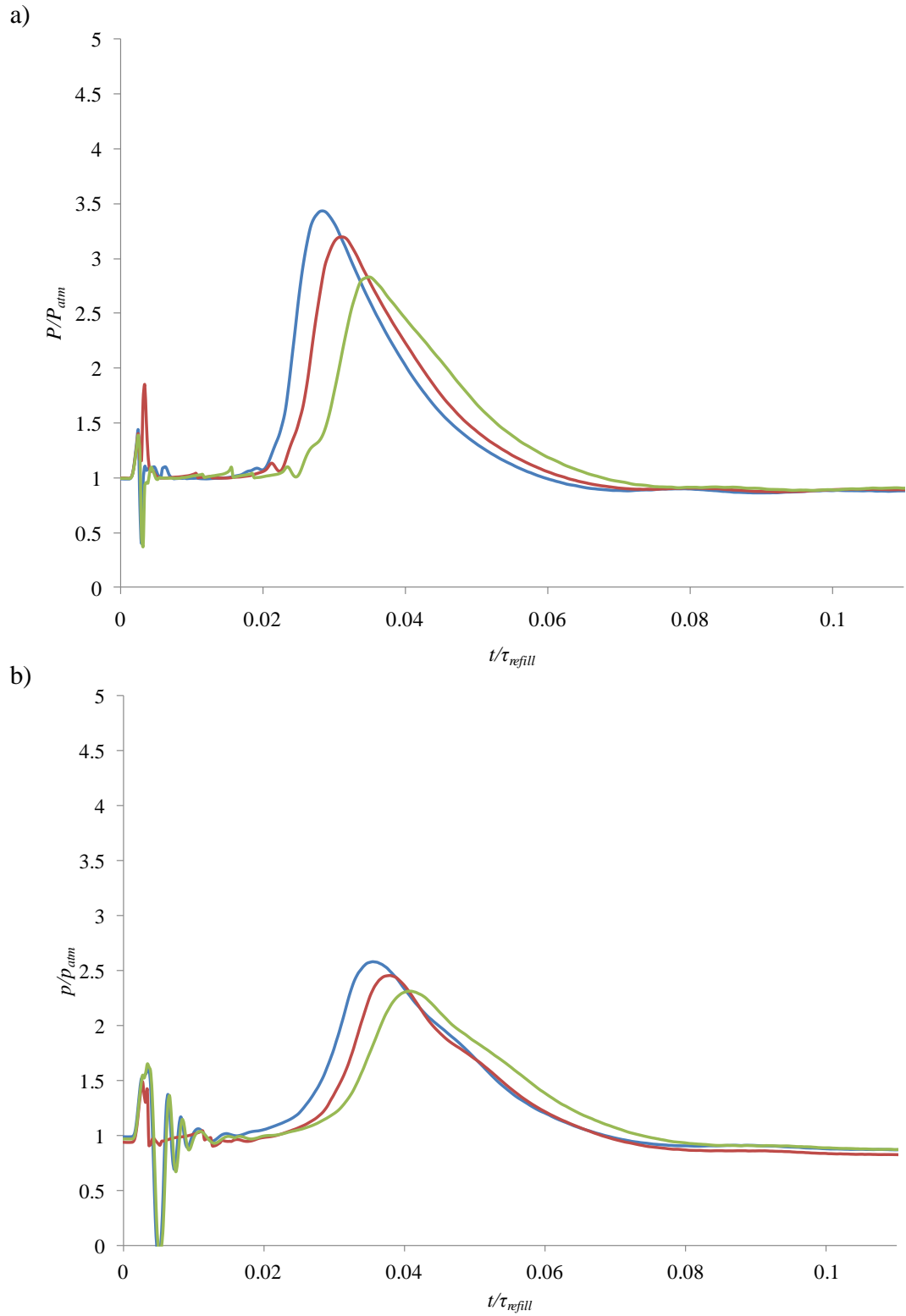


Figure 4.14: Pressure traces,  $Q = 66.7 \text{ s}\cdot\text{cm}^3/\text{s}$ ,  $\Phi = 0.75$  for a)  $d_{air} = 1.63$  and b)  $2.92 \text{ mm}$ ,  $f = 5$  (—),  $10$  (—),  $15 \text{ Hz}$  (—)

$d_{air}$ (mm)	$\overline{u_{air}}$ (m/s)	Momentum flux ratio	$p_{max}/$ $p_{atm}$	$\Delta t_{rise}/$ $\tau_{refill}$	$\Delta t_{pulse}/$ $\tau_{refill}$	$J_1/J_0$
0.79	89	28	3.8	0.0261	0.0427	151
1.63	24	6.5	3.4	0.0287	0.0444	144
2.92	7.6	2.0	2.6	0.0359	0.0434	112

Table 1: Peak pressure, mean inlet velocity, momentum flux ratio with respect to hydrogen jet, selected timing parameters, and actuation jet impulse for  $d_{air} = 0.79, 1.63,$  and  $2.92$  mm,  $Q = 66.7$  std.  $\text{cm}^3/\text{s}$ ,  $\Phi = 0.75$ , and  $f = 5\text{Hz}$

The correlation between the momentum flux ratio and the peak pressure is due in part to the loss of pressure because of back-flow of expanding chamber gases into the air inlet. As  $d_{air}$  increases, the upstream pressure required to maintain the desired flow rate decreases. Because of this, there is more flow of burning reactants back up the air line. This expansion over a greater volume is partially responsible for the decrease in  $p_{max}$  with decreasing momentum flux ratio. The momentum flux ratio can also be interpreted as a measure of the extent to which the air jet influences the flow field. When the momentum flux ratio is high, the air jet is dominant and the hydrogen inlet flow penetration is very low. Most mixing between the reactant streams occurs near the fuel inlet. As the air jet becomes weaker, and the penetration of the hydrogen jet increases, it would seem that mixing would improve. However, this is not the case. In order to understand this, it is necessary to examine flow field data for  $d_{air} = 2.92$  mm.

#### 4.4.1 Non-Combusting Flow Field

The internal flow in the absence of combustion for  $d_{air} = 2.92$  mm is shown in Figure 4.15. Comparison with the flow field in Figure 4.11 shows that the general circulatory flow is qualitatively similar. Foremost among the similarities is that the general flow patterns and the regions of circulation are still present in the same locations.

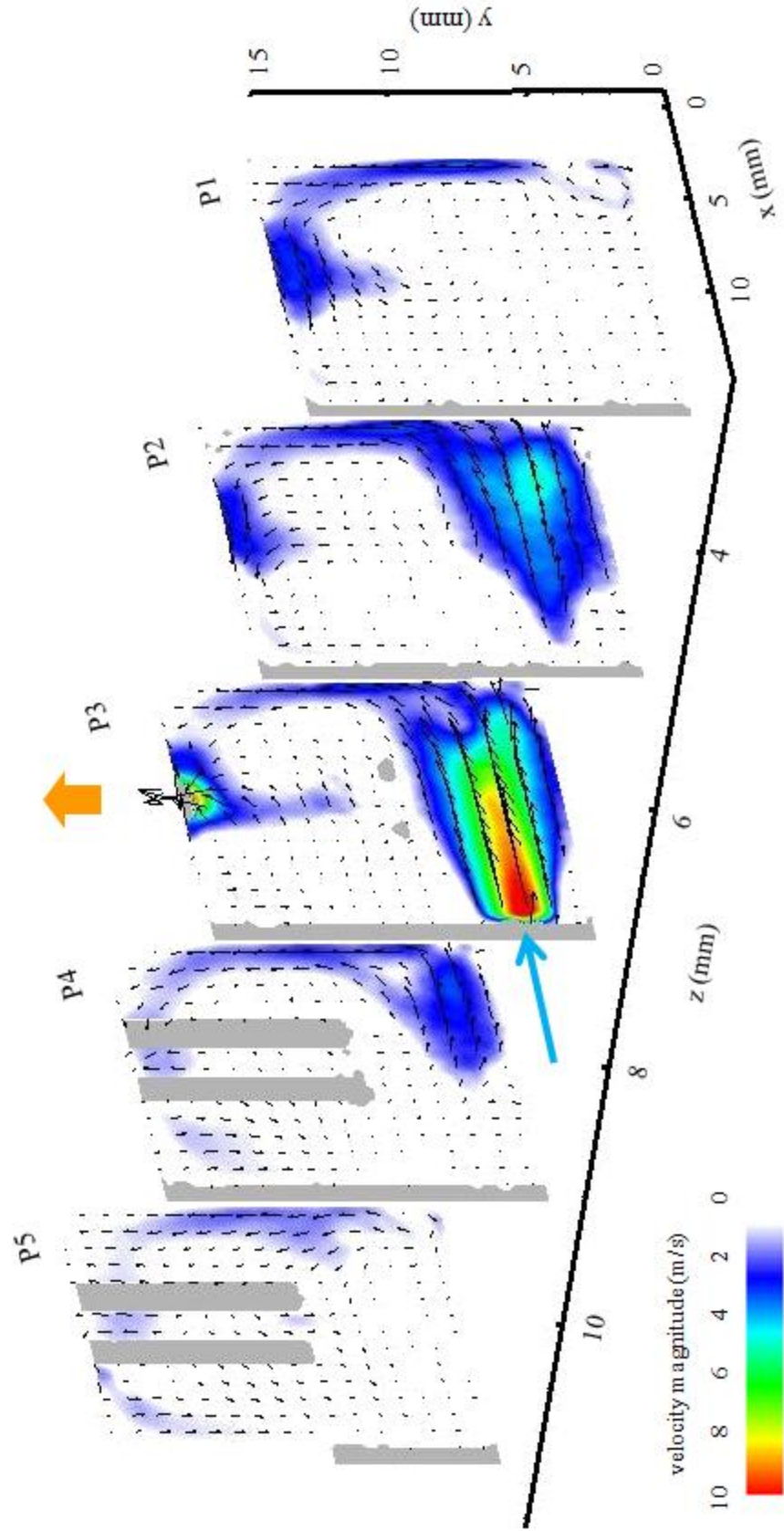


Figure 4.15a: Planar PIV cross-sections of the non-combusting flow field,  $P1-5$ ,  $d_{air} = 2.92$  mm,  $Q = 66.7$  s-cm<sup>3</sup>/s,  $\Phi = 0.75$  and  $f = 5$ Hz

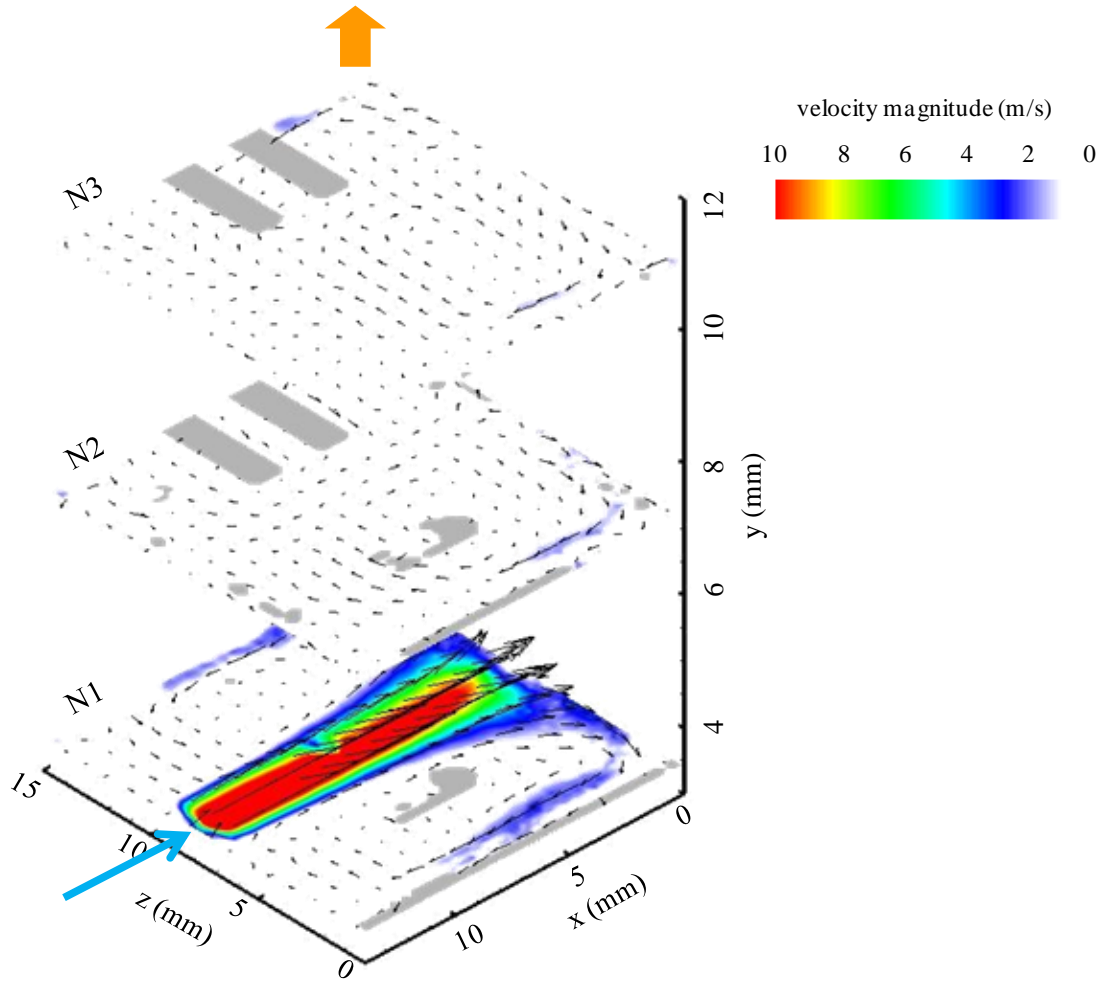


Figure 4.15b: Planar PIV cross-sections of the non-combusting flow field, N1-3,  $d_{air} = 2.92$  mm,  $Q = 66.7$  s-cm<sup>3</sup>/s,  $\Phi = 0.75$  and  $f = 5$ Hz

In both cases, plane N1 shows the impingement of the air jet on the opposite wall and the dual counter-rotating circulation cells set up on either side, and planes P1-5 show that the counterclockwise circulation is preserved. However, it is evident that the speed of the flow in all domains within the combustion chamber is significantly reduced (the bulk flow drops from  $\sim 3$ -5 m/s in Figure 4.11 to  $\sim 1$ -2 m/s in Figure 4.15). This change in the global flow field significantly affects the combustion process.

#### 4.4.2 Combusting Flow Field Evolution

The combusting flow field for  $d_{air} = 2.92$  mm is shown in Figure 4.16 (pressure trace shown in Figure 4.14b) and exhibits behavior similar to the field in Figure 4.12. Note that at this inlet speed, the air jet can be resolved by PIV. Similar to the actuator with  $d_{air} = 0.79$  mm (cf. Figure 4.12), the flame front starts by 0.3 ms after spark ignition ( $t/\tau_{refill} = 0.007$ , cf. Figure 4.16b) and propagates outwards from the center of the chamber. For both cases the flame propagates faster towards the rear of the chamber than the front (the size of the flame front is greater in planes P4 and P5 than in P1 and P2). However, for  $d_{air} = 2.92$  mm, the bulk flow is much slower during the combustion process, and the flame front propagates somewhat slower ( $\sim 6$  m/s for  $d_{air} = 2.92$  mm vs.  $\sim 8$  m/s for  $d_{air} = 0.79$  mm, cf. Figures 4.13 and 4.17). Another difference is the lower speed of the fluid ahead of the flame front at 0.5 ms and 0.7 ms ( $\sim 4$  m/s for  $d_{air} = 2.92$  mm, compared to approximately  $\sim 6$  m/s for  $d_{air} = 0.79$  mm in P3, cf. Figures 4.12c and 4.16a and b). Decreasing the momentum flux of the air jet also results in a longer duration combustion process and pressure pulse (cf. Table 1).

Further comparison of Figures 4.12 and 4.16 also shows that while there is still evidence of the air jet at  $t = 0.7$  ms for  $d_{air} = 0.79$  mm (Figure 4.12d), the air jet has ceased at the same time for  $d_{air} = 2.92$  mm (Figure 4.16d). This is a result of the pressure rise in the chamber: though  $\Delta t_{rise}$  is higher and  $p_{max}$  is lower for  $d_{air} = 2.92$  mm, the pressure upstream of the air inlet is lower, thus the pressure inside the chamber required to shut off the inlet flow is lower. Note also that by  $t = 0.5$  and 0.7 ms (Figures 4.16c and d), the flow towards the exhaust orifice does not exhibit the higher speeds that are observed for  $d_{air} = 0.79$  mm (Figures 4.12c and d). This is in agreement with the rise

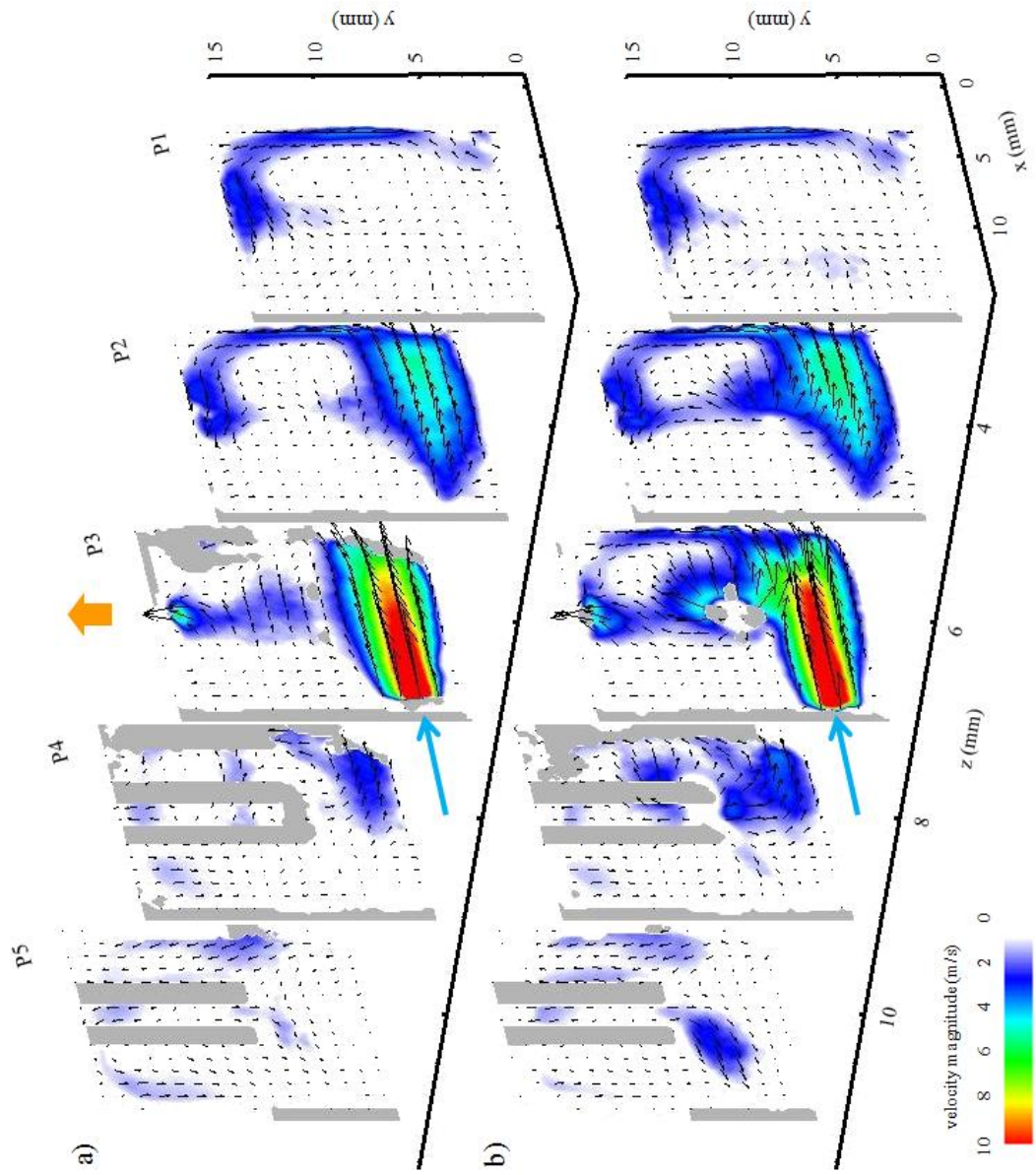


Figure 4.16: Planar PIV cross-sections of the combustor flow field,  $d_{air} = 2.92$  mm,  $Q = 66.7$  s-cm<sup>3</sup>/s,  $\Phi = 0.75$  and  $f = 5$  Hz, a)  $t = 0.1$  ms ( $t/\tau_{refill} = 0.002$ ) and b)  $0.3$  ms ( $0.007$ )

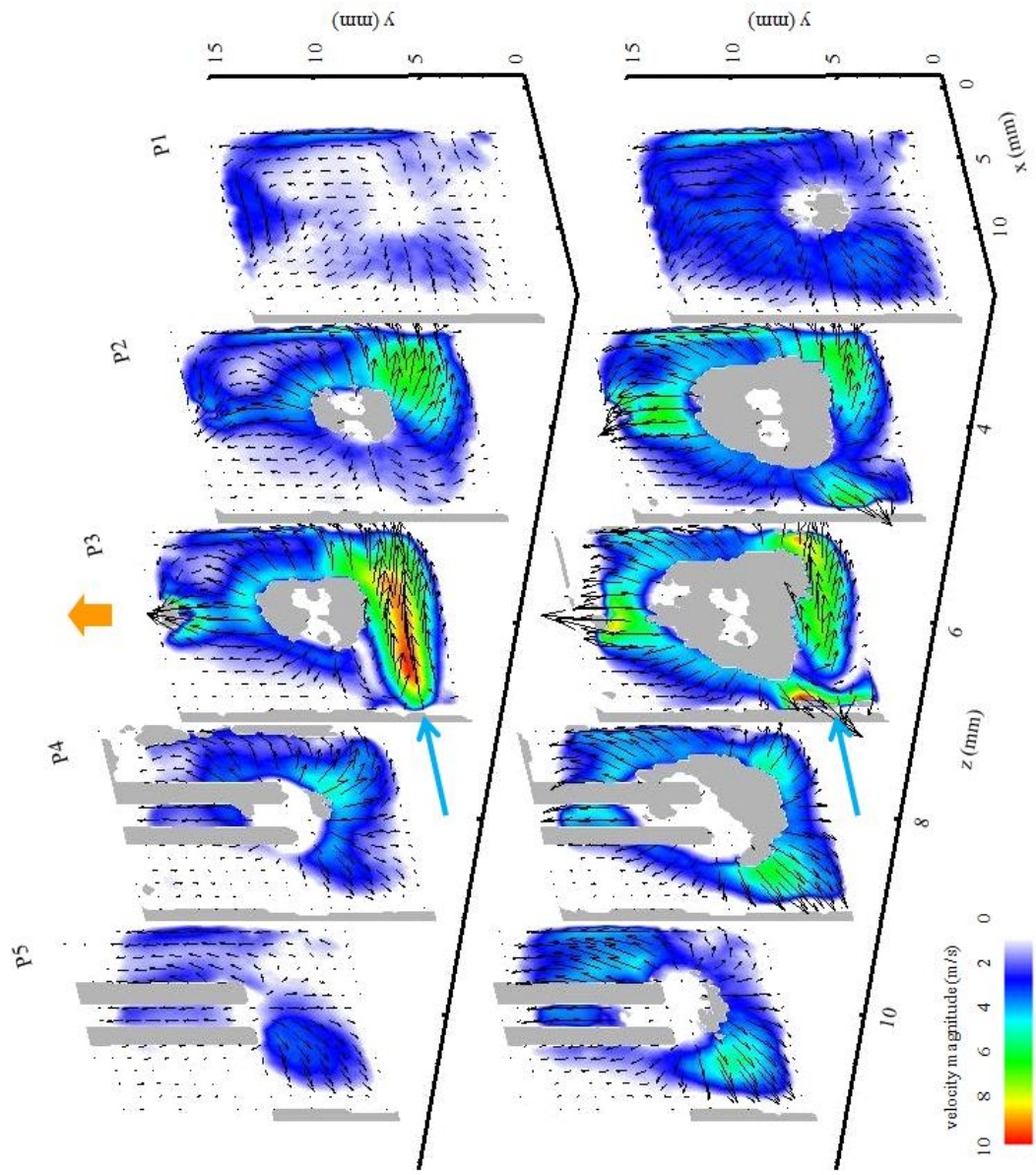


Figure 4.16: Planar PIV cross-sections of the combustor flow field,  $d_{air} = 2.92$  mm,  $Q = 66.7$  s-cm<sup>3</sup>/s,  $\Phi = 0.75$  and  $f = 5$  Hz, c)  $t = 0.5$  ms ( $t/\tau_{refill} = 0.011$ ), and d)  $0.7$  ms ( $0.016$ )



times and pressure pulse durations noted in Table 1 ( $\Delta t_{rise}/\tau_{refill} = 0.0261$  vs. 0.0359, and  $\Delta t_{pulse}/\tau_{refill} = 0.0427$  vs. 0.0434 for  $d_{air} = 0.79$  and 2.92 mm respectively), confirming that decreased momentum flux of the air inlet jet results in a lower-momentum control jet.

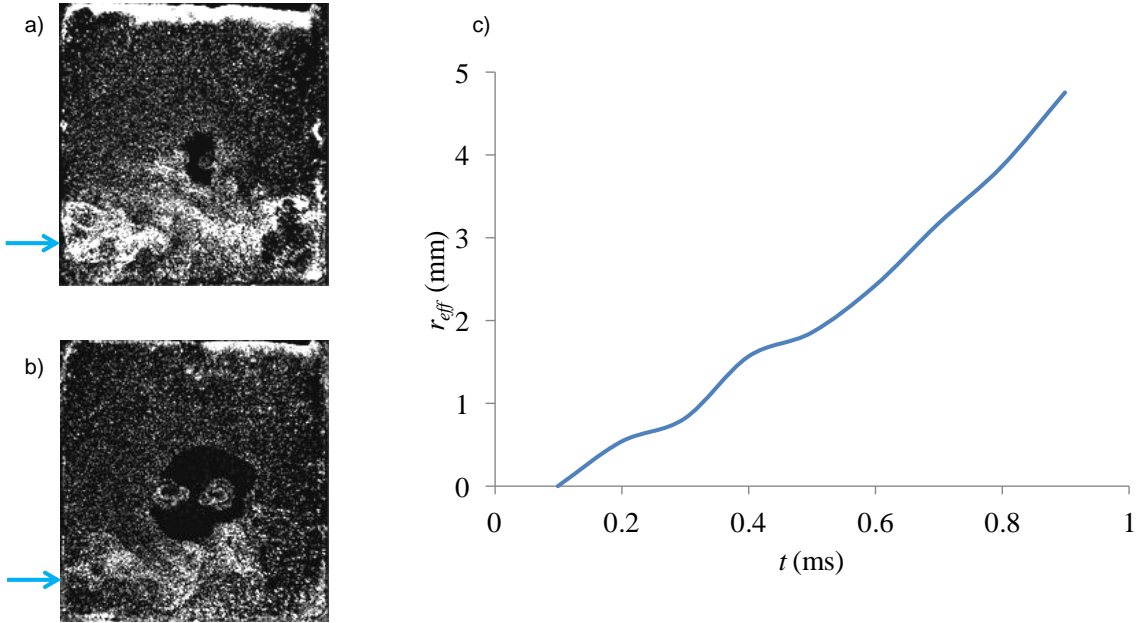


Figure 4.17: Images showing propagation of the flame front in the central plane P3 at a)  $t = 0.3$  ms and b) 0.5 ms after spark ignition, and c) the change in  $r_{eff}$  with time. The blue arrows mark the location of the air inlet.

Figure 4.17 shows the progression of the flame front. Compared to Figure 4.13, the images of the flame show a smoother flame front, with less wrinkling (though wrinkling is still present). This is indicative of the decreased intensity of small-scale motion within the combustion chamber, and therefore of a lower flame propagation speed, as is evidenced by the lower increase of flame area in Figures 4.17a and b, and the lower growth rate of  $r_{eff}$  in Figure 4.17c, compared to the corresponding data in Figure 4.13. While the  $x$ -intercept suggests that the flame front appeared at around the same time for both values of  $d_{air}$ , the shallower slope of the curve confirms that the flame

propagation rate is indeed lower for  $d_{air} = 2.92$  mm. The mean slope of the curve yields a flame speed of 5.7 m/s, approximately 26% lower than that for  $d_{air} = 0.79$  mm. The decrease in small-scale motion within the chamber associated with the lower Reynolds number of the air jet (cf. Section 4.2). As a result of the reduced small scale motion, the flame speed  $S_T$  and thus the flame propagation speed  $S_F$  are both reduced, resulting in the lower performance in terms of reduced peak pressure and maximum operating frequency.

The magnitude of small-scale motion can be assessed from distributions of the Turbulent Kinetic Energy (TKE) for both the non-combusting and the combusting flows for  $d_{air} = 0.79$  and 2.92 mm (Figures 4.18 and 4.19 respectively. Figure 4.18a shows that the greatest concentration of TKE is in the circulatory flow around the perimeter of the chamber that issues directly from the jet. Some of the data for the inlet jet is masked (cf. Sections 3.2 and 4.3) but it is known that the Reynolds number of the jet is approximately 6000 (cf. Section 4.2) and therefore the jet is likely turbulent (Rajaratnam 1976). Note also that during combustion, the TKE intensity increases in the vicinity of the flame front, suggesting that the combustion process itself accelerates the flow, thus causing increased small-scale motions.

Figure 4.19 shows that the result of reducing the momentum flux of the air jet, and hence its Reynolds number ( $Re_{air} \approx 1600$ ), drastically reduces small-scale motions. The distribution of TKE in Figure 4.19a is somewhat more uniform, with a slightly higher concentration where the air jet impinges on the opposite wall (i.e. where the hydrogen inlet is located). Once combustion occurs, it is possible to see slight increases in TKE around the flame front, indicating that, once again, there is flame-induced small-scale motion. The reduced TKE throughout the flow field is associated with the reduced

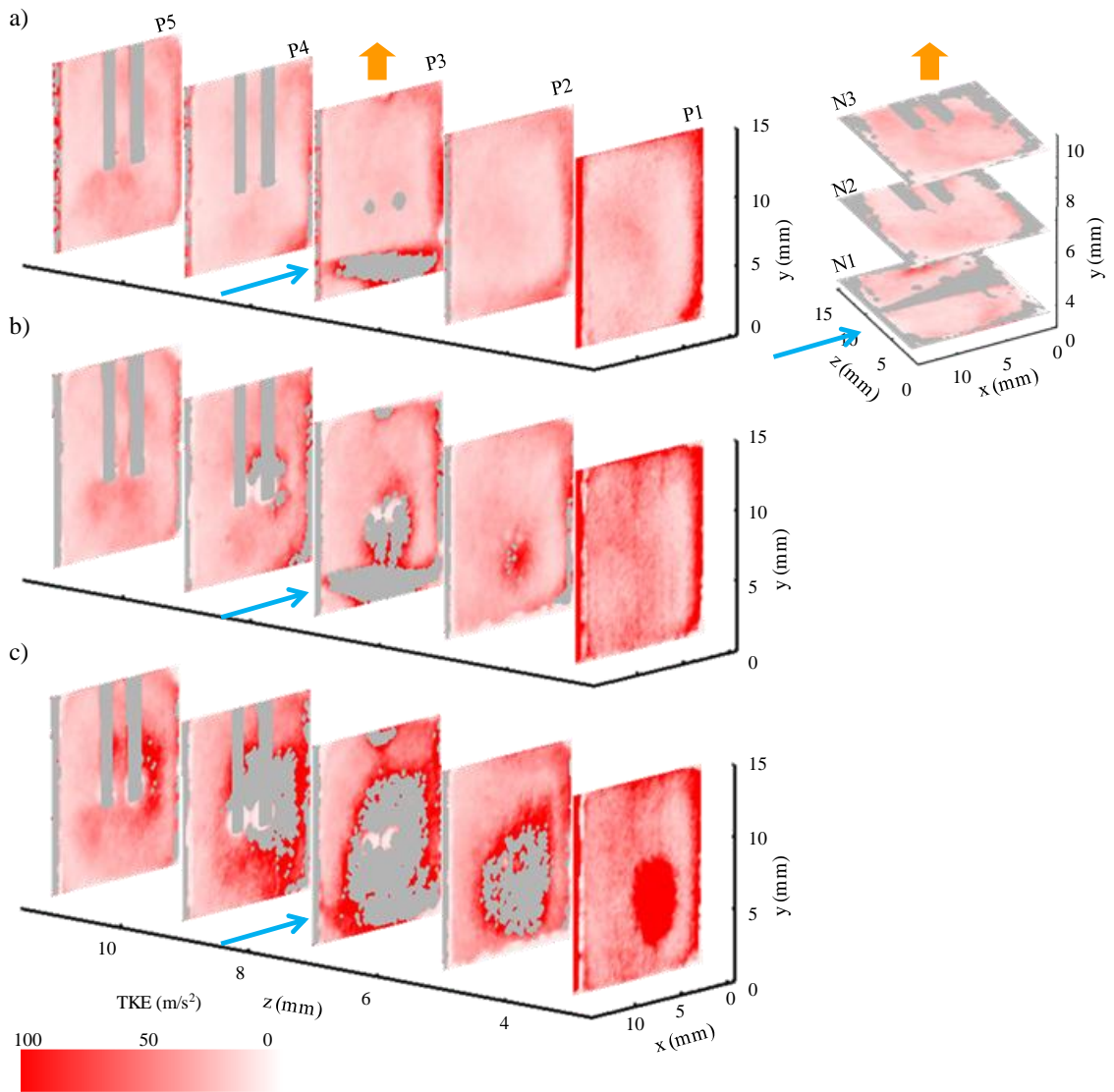


Figure 4.18: Planar cross-sections of TKE of the combustng flow field,  $d_{air} = 0.79$  mm,  $Q = 66.7$  s-cm<sup>3</sup>/s,  $\Phi = 0.75$  and  $f = 5$ Hz, a) non-combusting flow, b) 0.3 ms (0.007), and c) 0.5 ms (0.011)

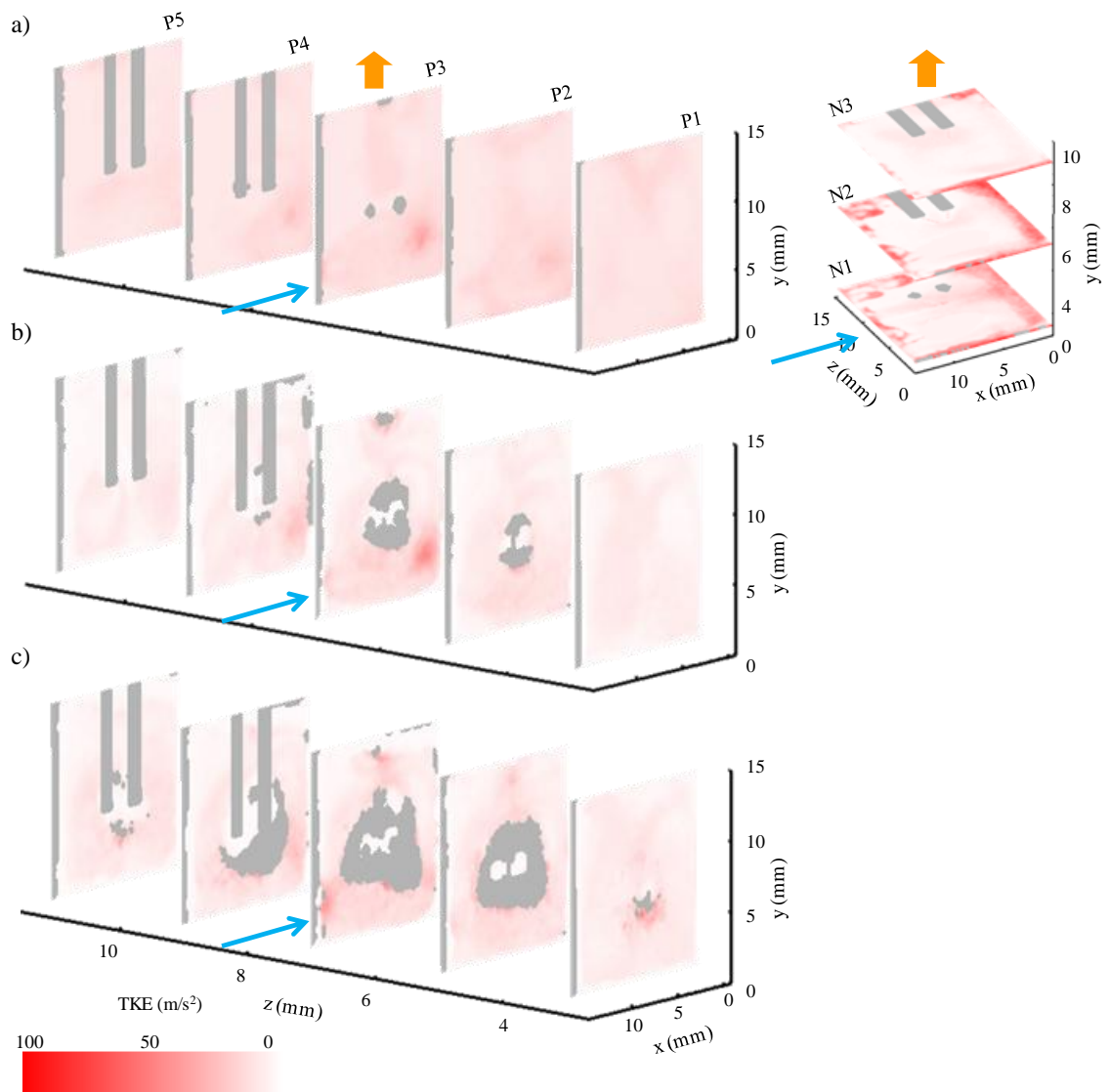


Figure 4.19: Planar cross-sections of TKE of the combustor flow field,  $d_{air} = 2.92$  mm,  $Q = 66.7$  s-cm<sup>3</sup>/s,  $\Phi = 0.75$  and  $f = 5$ Hz, a) non-combusting flow, b) 0.3 ms (0.007), and c) 0.5 ms (0.011)

bulk flow speeds shown in Figures 4.15 and 4.16. From this data and the data in Figure 4.18, it can be concluded that the increasing the Reynolds number of the air jet increases the intensity of the small scale motions within the bulk flow in the combustion

chamber, and therefore increases the flame speed and improves the performance characteristics of the actuator.

#### **4.4 Investigation of the Refill Process**

The preceding discussion has focused on the combustion process and how it is affected by changing inlet flow parameters. The efficiency of the refill process is an important factor in determining the actuator's performance and is discussed here. As Figures 4.5 and 4.10 show, it is necessary to lower the operating frequency below 5 Hz to reach the point at which the peak pressure reaches a maximum. This suggests that the mixing process in the present experiments is incomplete (i.e.: the time required to completely mix reactants and products is longer than the time between pulses, cf. Section 2.2.2), as is the scavenging of the combustion products from the previous cycle.

The ideal refill process is as follows: following combustion, the remnant products inside the chamber are displaced by incoming fresh reactants once the inlet flows begin. The reactants mix evenly upon contact, and are advected by the flow induced by the air inlet throughout the volume of the chamber. However, the present combustion chamber configuration has several limitations. First, combustion products are never displaced without some mixing with the incoming reactants. Thus, along with combustion products some fresh charge leaves the chamber during the refill process, while some of the product species remain in the chamber for longer times. It is possible that there are regions of the flow, such as circulation cells in the corners of the chamber, which trap combustion products for multiple cycles. Second, complete mixing between reactants is unlikely to happen on contact, and distribution of the fresh charge throughout the chamber is likely

to be hampered by regions of recirculating flow or the placement of the air and hydrogen inlets. This placement of inlets may result in well-mixed charge, but as Chapter 5 will show, there can be regions of the chamber that are fuel deficient. These regions experience lower flame speeds resulting in either slow or incomplete combustion overall and generally lower performance.

In order to quantify  $\Delta t_{mix}$  and hence the refill process, phase-locked PIV measurements were obtained for various times between combustion and processed to reveal the amount of fresh oxidizer that enters the chamber. The hypothesis underpinning this method is that once combustion is complete, all the smoke particles used for seeding of the previous cycle will have burned off. New seed particles arriving with fresh flow of air into the chamber therefore indicate the concentration of fresh reactant in the chamber. By tracking the concentration of seeding particles (the seeding density,  $\rho_s$ ) over time, the progress of the refill process can be charted.

Figure 4.20 shows how this is accomplished. Single images of the flow in plane P3 at a given time are extracted from a PIV image pair (Figure 4.20a). This grayscale image is then processed to first enhance contrast and then turned into black and white using a user-defined threshold (Figures 4.20b and c). This produces an image where seed particles stand out against a dark background. A region within the chamber is then selected, away from the inlet jets, exhaust orifice, and spark plugs, as the area in which the concentration is computed. In this area, the mean brightness is calculated, with the brightness increasing in proportion with the number of seed particles. This is repeated for the same region in 100 images taken at the same phase during the refill process. By repeating this procedure at a series of time steps prior to ignition, it is possible to show

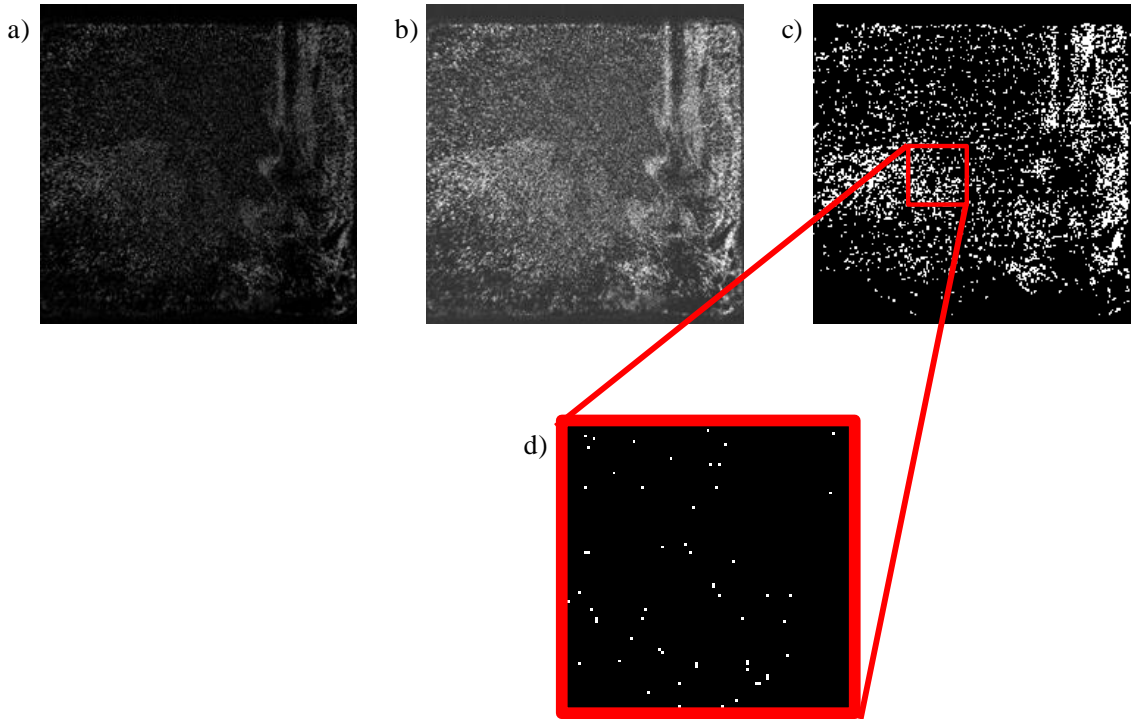


Figure 4.20: Images used to determine seed particle density, a) PIV image of P3 seeded flow, b) contrast-enhanced image, c) conversion to black and white, and d) computation of seed density based on mean brightness of selected area

how  $\rho_s$  varies over time, and thus gain an estimate for the mixing time. Because the smoke particles are produced by burning incense, there is some variability in concentration, and therefore the data must be normalized by the concentration of particles in the non-combusting flow produced by the same incense source ( $\rho_{s0}$ ).

Figure 4.21 shows the variation of seed density versus for  $d_{air} = 0.79$  and  $2.92$  mm at  $f = 5, 10,$  and  $15$  Hz. It is assumed that  $\Delta t_{mix}$  can be approximated as the time interval from  $t/\tau_{refill} = 0$  to the time when the curve levels off. There are three clear trends: 1) the curves have generally similar shapes with seed density increasing with time and the slope of the curve decreasing with time, 2) higher frequency operation implies a longer  $\Delta t_{mix}$ , and 3) the higher momentum flux case,  $d_{air} = 0.79$  mm, is refilled faster at all tested

frequencies. The fact that increasing  $f$  adversely affects performance has already been established in earlier discussion. Lengthening  $\Delta t_{mix}$  results in a longer and less efficient refill process, such that the effective equivalence ratio of the starting mixture is lower.

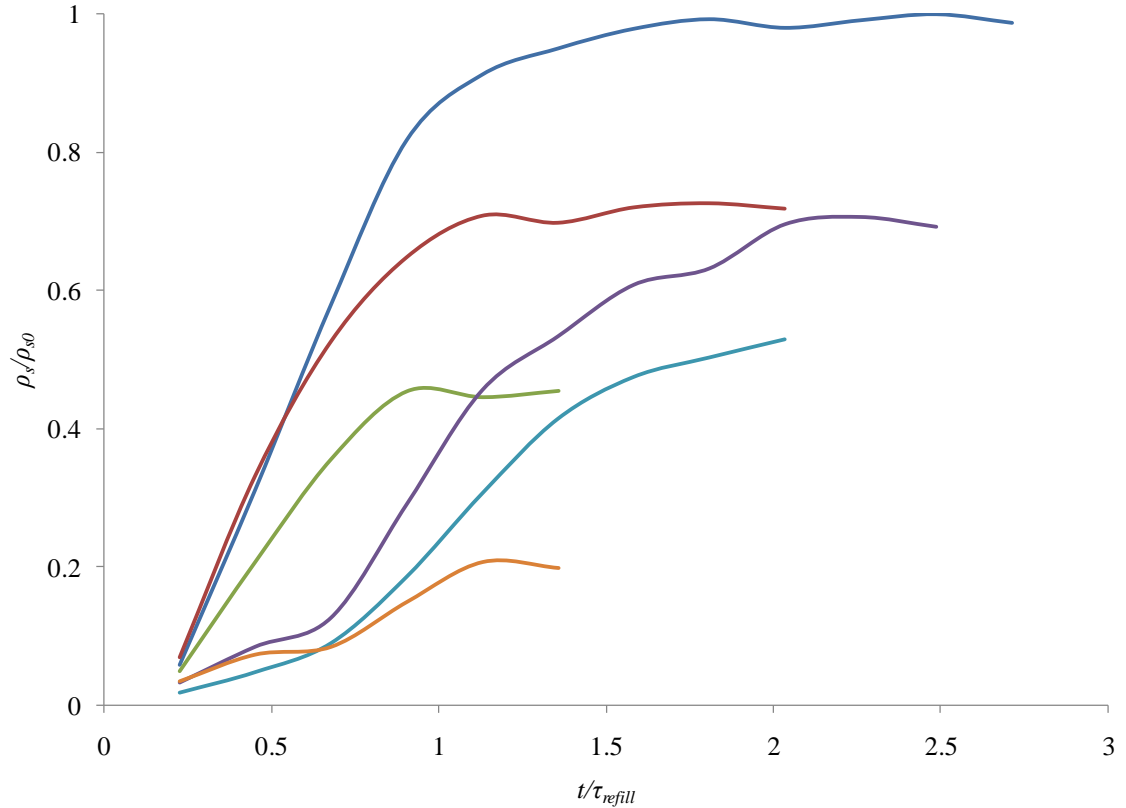


Figure 4.21: Variation of  $\rho_s/\rho_{s0}$  with  $t/\tau_{refill}$ ,  $Q = 66.7 \text{ s-cm}^3/\text{s}$ ,  $\Phi = 0.75$ ,  $d_{air} = 0.79 \text{ mm}$  at  $f = 5$  (—),  $10$  (—), and  $15 \text{ Hz}$  (—), and for  $d_{air} = 2.92 \text{ mm}$  at  $f = 5$  (—),  $10$  (—), and  $15 \text{ Hz}$  (—)

The increased duration of the process is due to the increased amount of exhaust products that are still present in the chamber after combustion. At low actuation frequencies the peak pressure is higher as a consequence of more complete mixing leading to higher flame speeds and an increased in the volume of exhaust gases exiting the chamber in the actuation jet. As peak pressure decreases, it is possible that a greater mass of combustion



products remain in the chamber to be displaced by the incoming flow such that scavenging of the chamber takes more time. The reduced  $\Delta t_{mix}$  due to increased momentum flux of the air jet is due to the higher speed of the fresh reactant streams, since the chamber is evacuated in a shorter time. Higher inlet jet speeds also mean more small-scale motions, and thus more mixing of reactants and products. However, this effect is outweighed by the improved scavenging from using a high-speed air jet.

The increase in  $\rho_s$  with time is obvious, and certainly, as seed density approaches maximum, the rate of increase should slow. The curve for  $d_{air} = 0.79$  mm at  $f = 5$  Hz has leveled off at  $\rho_s/\rho_{s0} = 1.0$  prior to ignition of the next cycle, which would suggest that mixing is complete, but as mentioned earlier the pressure data in Figures 4.5, and 4.10 shows that this is not the case under these conditions. There are two possible explanations for this discrepancy. First, although the concentration of air may reach the desired level, it is possible that concentration of fuel has not. Second, the data is taken from plane P3 (where the air jet is located), and it is certainly possible that concentrations and mixing away from the center plane are low and incomplete respectively. Note that at higher frequencies, the temperature of the actuator walls and the inlet tubes increases so that more seed particles may be burned when they come into contact with these surfaces. It is recognized that the true extent of the mixing during the refill process is overestimated by the seeding method (though to what extent is unknown), but the trends show that refill occurs faster for higher momentum air jets and at lower frequencies.

## CHAPTER 5

### EFFECT OF VARIATION OF INLET CONFIGURATION ON ACTUATOR PERFORMANCE

In the Chapter 4, it was shown increasing the Reynolds number of the air jet and its momentum flux relative to the hydrogen jet results in improved mixing and flame speed, and therefore significantly improves the performance of a combustion powered actuator. These data suggest that changes in inlet geometry might alter the internal flow field of the combustion chamber to further improve the performance of the actuator. This section considers the effects of relocation of both the air and fuel inlets, together with variation of the air inlet diameter.

#### 5.1 Combustion Actuator Inlet Configurations

The opposed  $3 \times 3$  array of air and fuel inlets allow the locations of the air and fuel inlets to be varied relative to each other and with respect to the fixed chamber features (i.e. the exhaust orifice and spark plugs), while maintaining all other critical dimensions. This combined with the ability to vary the air inlet diameter  $d_{air}$  results in a large number of possible configurations. The present work is restricted to configurations with one air inlet and one fuel inlet. Furthermore, the number of inlet position configurations was limited to 54 by bisecting the chamber along a plane of symmetry through the exhaust orifice ( $z = 7$  mm, cf. Figure 3.2). Figure 5.1 shows a schematic of inlet positions and the labeling scheme for various configurations. The fuel inlets are

labeled from A to F, while the air inlets are labeled from 1 to 9. A particular configuration is identified by a letter-number combination (e.g.: B5).

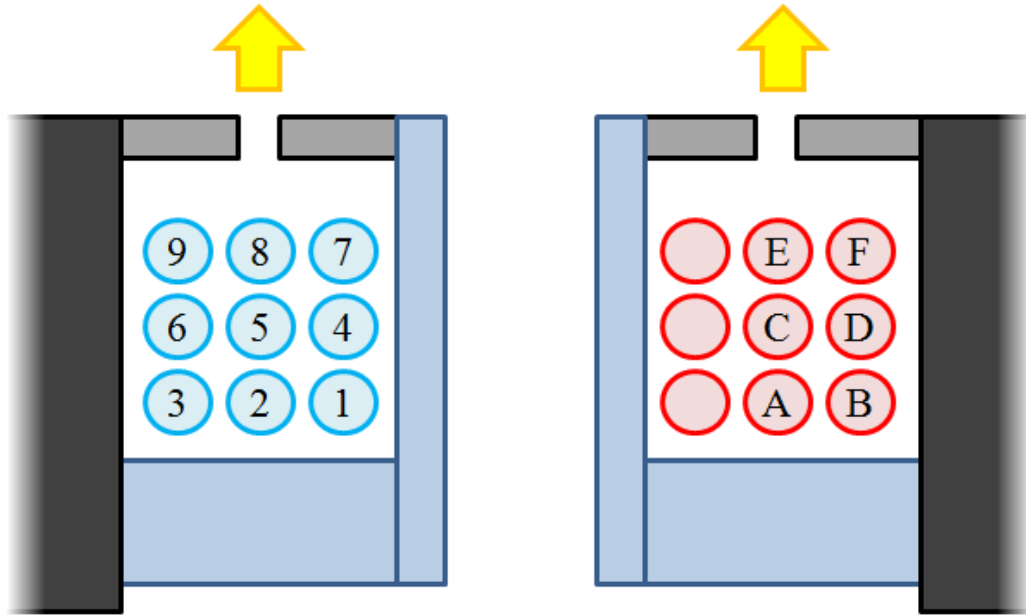


Figure 5.1: Schematic of actuator in showing arrays of air inlets (left) and fuel inlets (right).

The symmetry is approximate due to the presence of the spark plugs that emerge from the rear wall of the chamber. As noted in Chapter 4, the presence of the spark plugs significantly affects the flow field. In configuration A2 the spark plugs enhanced flame propagation towards the rear of the chamber.

## 5.2 Pressure Testing of Inlet Configurations

Combustion pressure measurements of the 54 configurations show that some inlet combinations yield better and worse performance than the baseline configuration, A2. Table A (appendix) shows  $p_{max}/p_{atm}$  for all tested configurations for  $\Phi = 0.75$ ,  $Q = 66.7$  std.  $\text{cm}^3/\text{s}$ , and  $f = 5\text{Hz}$ . These data show that for a given air inlet diameter ( $d_{air}$ ), the

difference between the lowest and highest  $p_{max}/p_{atm}$  varies between 2.2 ( $d_{air} = 1.63$  mm) and 1.8 ( $d_{air} = 0.79$  mm) and does not depend strongly on  $d_{air}$ . The difference between the lowest and highest fractions of  $p_{max}/p_{atm}$  relative to the maximum  $p_{max}/p_{atm}$  increases with  $d_{air}$  as the momentum flux of the air jet decreases. For  $d_{air} = 0.79$  mm,  $p_{max}/p_{atm}$  of configurations yielding the worst performance are 36% lower than those of the configurations producing the best performance. This difference increases to 53% for  $d_{air} = 2.92$  mm. It is not surprising that the performance of the actuator improves when the air jet Reynolds number increases (as discussed in Chapter 4).

As shown in Table A, the performance of the baseline configuration A2, as characterized by  $p_{max}/p_{atm}$ , is roughly in the middle relative to the performance of the other configurations for all three  $d_{air}$ . Two configurations, F1 and E5, were selected for detailed investigation: relative to the baseline, F1 produces higher  $p_{max}$  while E5 produces lower  $p_{max}$  for all  $d_{air}$ .

Figures 5.2a and b show pressure traces during the combustion process for F1 and E5 respectively for  $f = 5, 10,$  and  $15$  Hz ( $f/f_{refill} = 0.2215, 0.4425,$  and  $0.66375$ ) and  $d_{air} = 0.79$  mm, with pressure trace for A2 under the same conditions shown in dashed gray (note that there is some noise at the beginning of the cycle and after pressure relaxes). In light of the discussions in Chapter 4, and comparing the peak pressures for F1 and A2 between  $f = 5$  and  $15$  Hz, it is concluded that F1 would produce higher peak pressures at all frequencies ( $f_{max} = 110$  Hz and  $95$  Hz for F1 and A2 respectively). Conversely, for E5,  $p_{max}$  drops rapidly with frequency, indicating a low value of  $f_{max}$  ( $f_{max} \leq 25$  Hz for E5 under the conditions tested). By comparing the data in Figure 5.2 to that in Section 4.2, it is apparent that performance of A2 falls between F1 and E5.

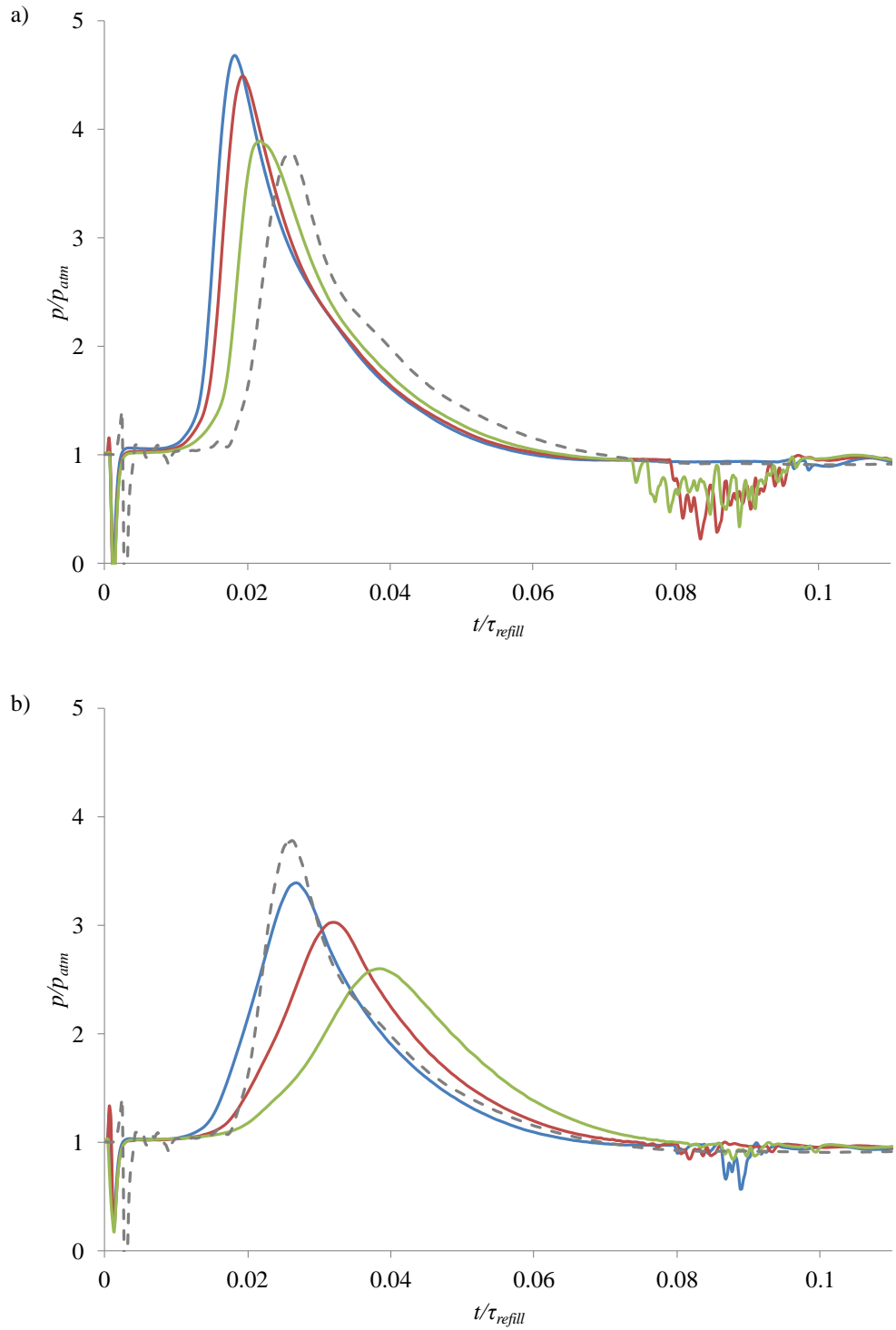


Figure 5.2: Pressure traces,  $Q = 66.7 \text{ s-cm}^3/\text{s}$ ,  $\Phi = 0.75$ ,  $d_{air} = 0.79 \text{ mm}$  for a) cfg. F1 and b) cfg. E5, for  $f = 5$  (—),  $10$  (—),  $15 \text{ Hz}$  (—); cfg. A2,  $f = 5 \text{ Hz}$  (— —)

Configuration	$p_{max}/p_{atm}$	$t_{start}/\tau_{refill}$	$\Delta t_{rise}/\tau_{refill}$	$\Delta t_{pulse}/\tau_{refill}$	$J_1/J_0$
A2	3.8	0.0179	0.0262	0.0427	151
F1	4.7	0.0113	0.0183	0.0389	190
E5	3.4	0.0133	0.0269	0.0452	144

Table 2: Peak pressure, start time, rise time, pulse duration, and actuation jet impulse for configurations A2, F1, and E5,  $d_{air} = 0.79$  mm,  $Q = 66.7$  std. cm<sup>3</sup>/s,  $\Phi = 0.75$ , and  $f = 5$ Hz

Table 2 shows other metrics used to quantify performance (cf. Section 4.2). As show, F1 produces the lowest  $t_{start}/\tau_{refill}$ ,  $\Delta t_{rise}/\tau_{refill}$ , and  $\Delta t_{pulse}/\tau_{refill}$ , thus indicating most rapid ignition, highest flame speed, a sufficiently short pulse such that there is more time for mixing at a given operating frequency, and the highest actuation jet impulse. The opposite is true for configuration E5, with A2 falling in the middle for most metrics except starting time.

### 5.3 PIV for F1 and E5

#### 5.3.1 F1 (High Peak Pressure Configuration)

##### *Non-Combusting Flow Field*

Figure 5.3 shows the non-combusting flow field for F1. There are marked differences compared to Figure 4.11 (configuration A2). First, the air jet is located in the bottom left corner of P1, while the hydrogen inlet is located in the top right of P5. As discussed in Section 4.3, the air jet exerts a dominant influence on the evolution of the flow field within the chamber, but since it is not in the central plane (P3) of the chamber its effect on the flow decreases with increasing  $z$ . In both A2 and F1 the air jet creates circulatory flow that impinges on the opposite wall and is forced CCW so that it interacts

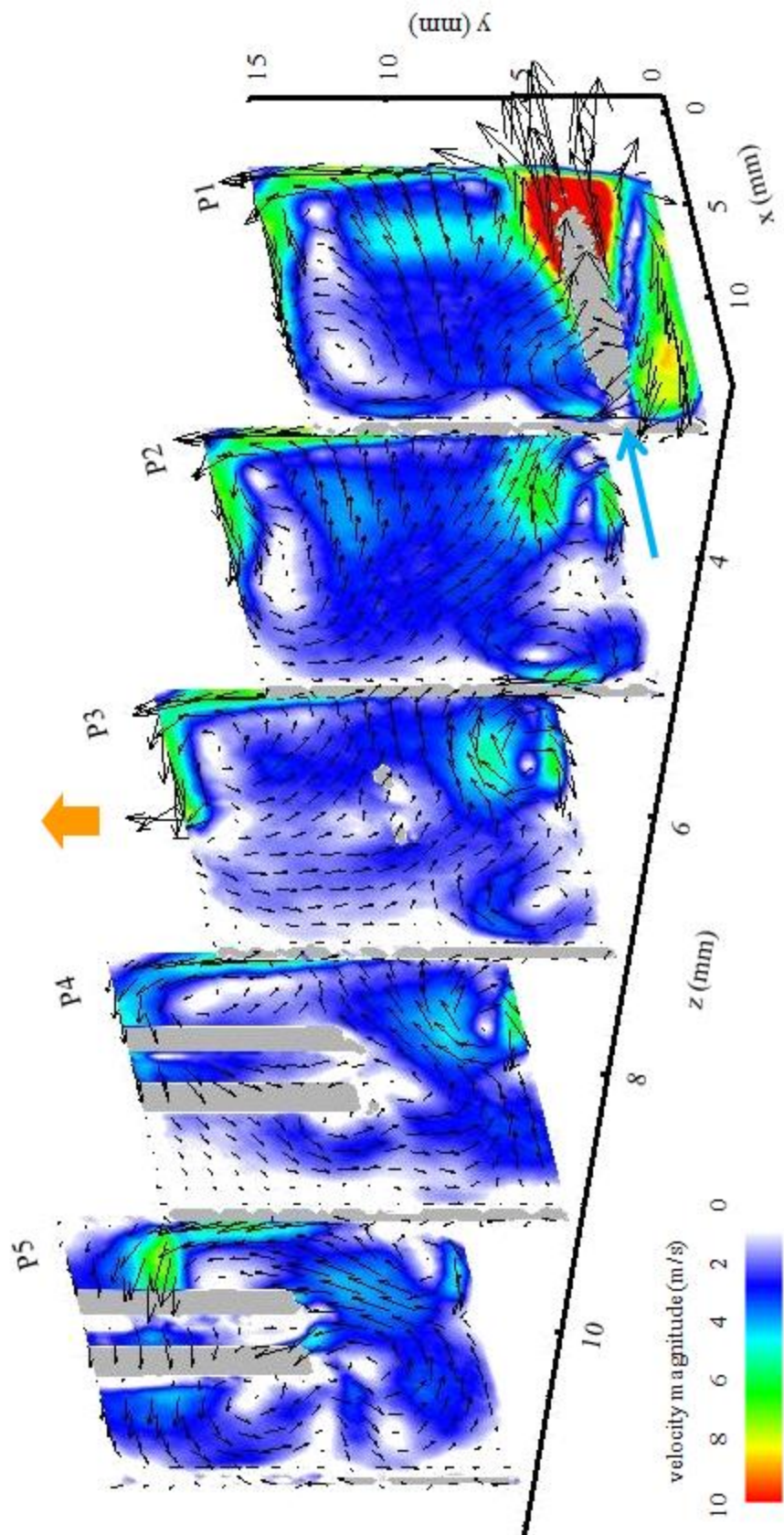


Figure 5.3a: Planar PIV cross-sections of the non-combusting flow field for configuration F1, P1-5,  $d_{air} = 0.79$  mm,  $Q = 66.7$  s-cm<sup>3</sup>/s,  $\Phi = 0.75$  and  $f = 5$  Hz

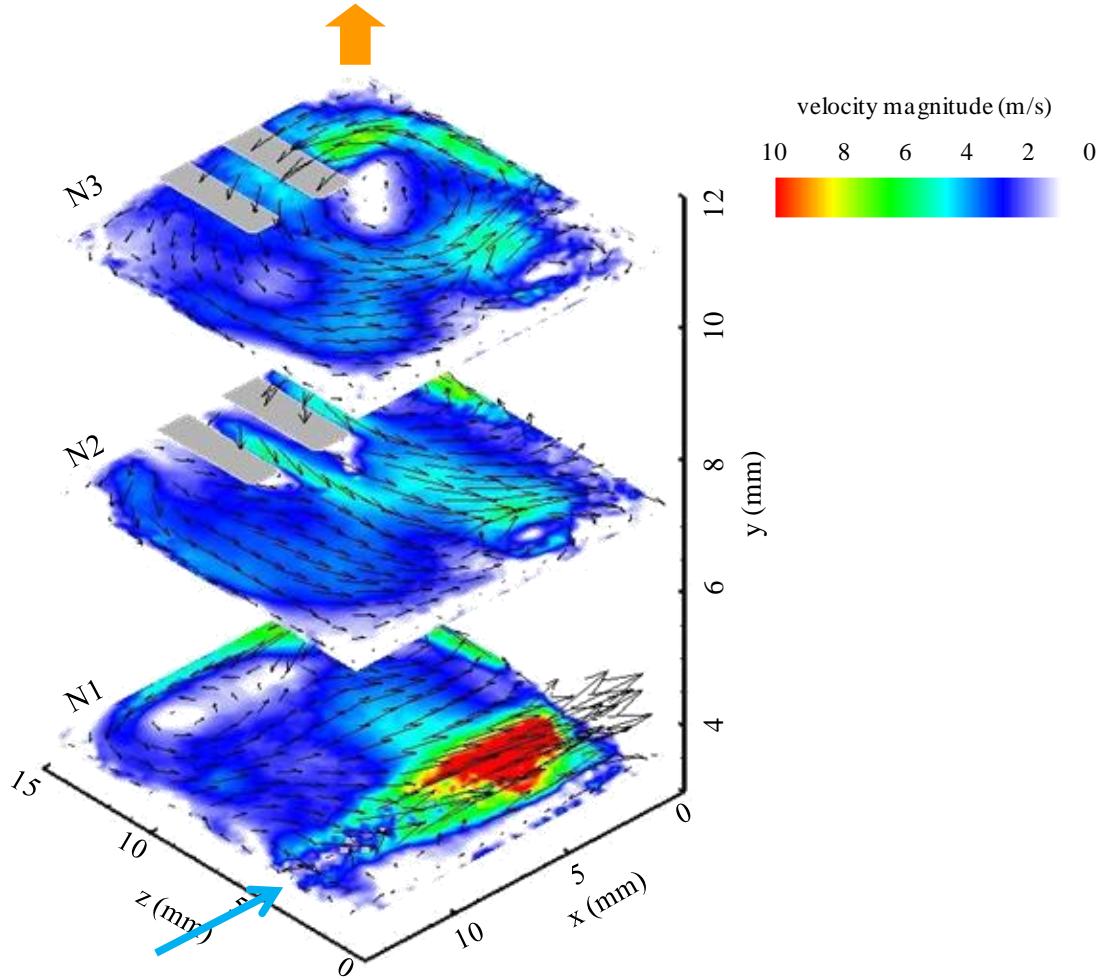


Figure 5.3b: Planar PIV cross-sections of the non-combusting flow field for configuration F1, N1-3,  $d_{air} = 0.79$  mm  $Q = 66.7$  s-cm<sup>3</sup>/s,  $\Phi = 0.75$  and  $f = 5$ Hz

with the jet. For F1 this circulation is weakest in P5. The interaction between the entrainment and the walls creates smaller CCW circulation regions near the walls in P2-4, but the general counter-clockwise circulation is maintained.

While the general motion of the fluid is circulatory in P4 and P5, there is considerable distortion of the flow by the presence of the spark plugs. Since the air jet is in P1, the flow decelerates before reaching planes P4 and P5. It is the distortion of the flow field created by the spark plugs and the slow-moving fluid in their vicinity that



enables perimeter circulation in P5, and to a lesser extent in P4, to remain at higher speeds than the flow in the same regions in P1 and P2. Of note is the faster region of flow in the top right corner of P5. This is due to entrainment and mixing of the circulatory flow with the hydrogen inlet jet. It appears that in this configuration, the circulatory flow produced by the offset inlets enables quicker and more even advection of mixed reactants throughout the chamber than in A2.

The images of planes N1-3 show a similar CCW circulation in all three planes. N1 and N2 are similar to P1, P2, and P3, as expected because of the similarity in geometry with respect to the location of the planes relative to the air jet. N3, which is located above the spark plugs, also exhibits circular motion, but in this case the motion is more complex because of interaction with the spark plugs.

### *Combusting Flow Field*

Figure 5.4 shows the evolution of the flow field during the combustion process. Only planes P1-5 are shown for simplicity, since the evolution of N1-3 is similar. The first appearance of the flame front in configuration F1 is observed at approximately  $t = 0.1$  ms after spark ignition ( $t/\tau_{refill} = 0.002$ ), earlier than in configuration A2 ( $t = 0.3$  ms, or  $t/\tau_{refill} = 0.007$ , cf. Figure 4.12b). The small flame front can be seen in P3 at the center of the chamber though the global flow field does not appear to be affected.

By  $t = 0.3$  ms, the flame front propagates through the chamber such that it is evident in every plane except P5. While the flame does not reach P5, the increased speed of the flow there is due to the enlarged flame front. An important distinction between the performances of configurations F1 and A2 is that flame propagation in F1 appears to be

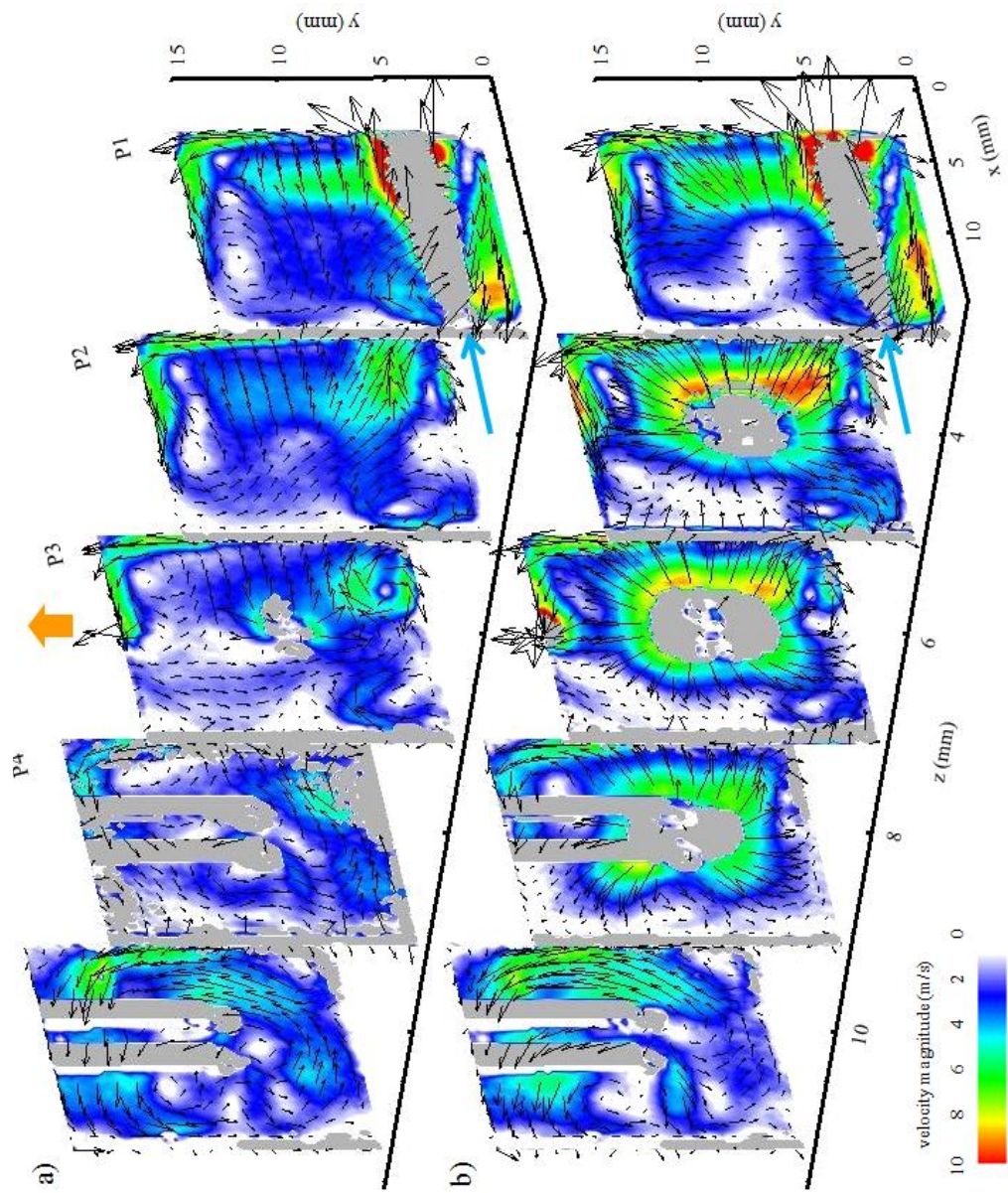


Figure 5.4: Planar PIV cross-sections of the combustor flow field of configuration F1,  $d_{air} = 0.79$  mm,  $Q = 66.7$  s-cm<sup>3</sup>/s,  $\phi = 0.75$  and  $f = 5$ Hz, a)  $t = 0.1$  ms ( $t/\tau_{refill} = 0.002$ ), b)  $0.3$  ms ( $0.007$ )

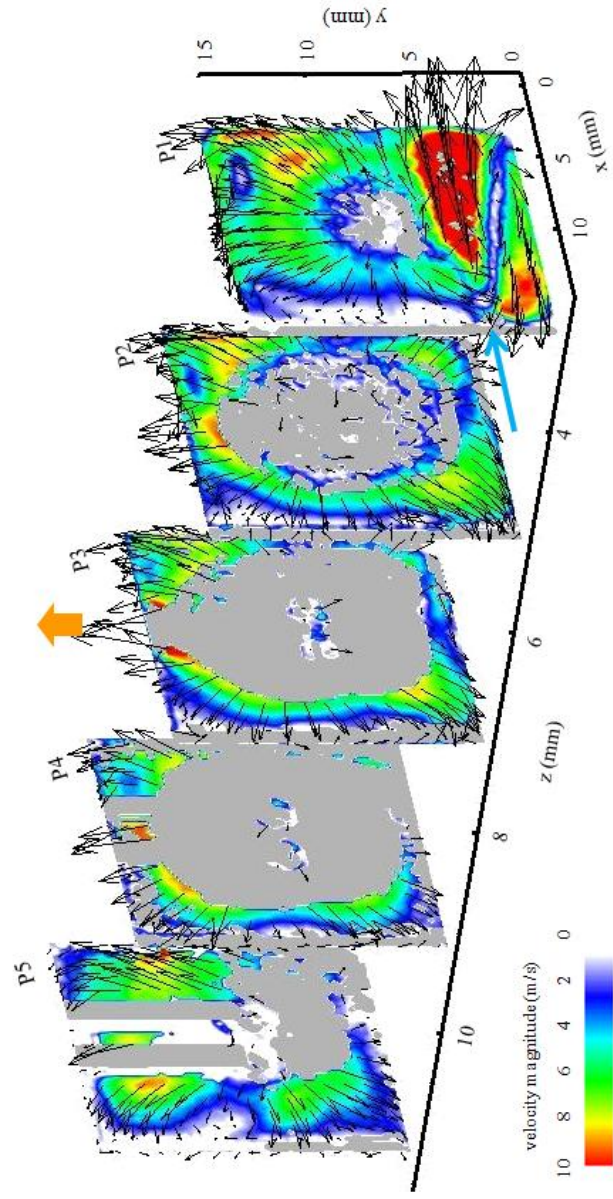


Figure 5.4c: Planar PIV cross-sections of the combustor flow field of configuration F1,  $d_{air} = 0.79$  mm,  $Q = 66.7$  s-cm<sup>3</sup>/s,  $\Phi = 0.75$  and  $f = 5$ Hz,  $t = 0.5$  ms ( $t/\tau_{refit} = 0.011$ )

more spherically symmetric throughout the chamber: combustion begins at the center of the chamber, at the tips of the spark plugs, and then burns outwards from this point at approximately equal speeds in all directions, suggesting that the distribution of reactants within the chamber is indeed more uniform.

At  $t = 0.5$  ms after spark ignition, the flame front occupies an approximately circular area 9 mm in diameter in plane P3. If this is plane is a symmetric cut through a spherical flame front, an assumption also made in Chapter 4, then this cavity has a volume of  $0.38 \text{ cm}^3$ , about 13% of the total combustion chamber (cf. Figure 5.5). At this time the burned exhaust gasses are escaping the chamber via the exhaust orifice, producing the control jet. Compared to the corresponding velocity field for A2, the outflow at  $t = 0.5$  ms for F1 is largely composed of burned gases, whereas for A2 the accelerating flow is unburned (seen from the presence of seeded flow escaping the chamber) and is pushed outwards by the slower-moving flame front. As such, this quicker burning and outflow imply that the mean momentum flux of the exhaust jet is higher for F1. Moreover, less unburned reactants appear to leave the chamber, as most of the exhaust flow seems to consist of burned gasses, resulting in more complete combustion and hence greater energy release.

Figure 5.5 shows the progression of the flame front. Similar to Figures 4.13 and 4.17, Figure 5.5a and b show representative images of the flame front at  $t = 0.3$  and 0.5 ms, while Figure 5.5c shows the growth of the effective radius of the flame front,  $r_{eff}$  with time (cf. Section 4.3). As in Figure 4.13, the flame front shows significant wrinkling, which is to be expected since  $Re_{air}$  is the same in both cases. However, it is clear that the flame front progresses farther within the same time than in A2, and expands

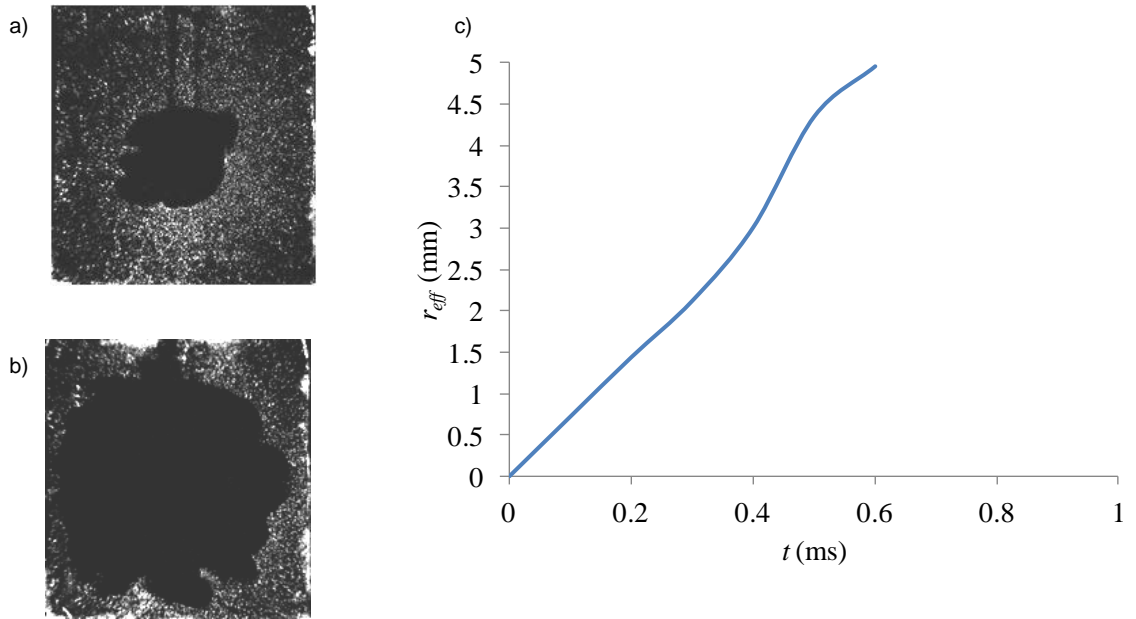


Figure 5.5: Images showing propagation of the flame front in the central plane P3 for configuration F1 at a)  $t = 0.3$  ms and b) 0.5 ms after spark ignition, and c) the change in  $r_{eff}$  with time.

more evenly in all directions, unlike the uneven motion towards the hydrogen inlet in A2. A comparison between the slopes of  $r_{eff}(t)$  in Figures 4.13c and 5.5c shows that the average slope of the curve in F1 is greater, which is consistent with the faster flame front in the images. Indeed, the flame speed calculated from the slope is 8.45 m/s, approximately 8% higher than A2. The plot also suggests that compared to A2, flame front growth begins sooner following ignition.

These data suggest that the global circulatory flow induced by location of the air jet in a corner of the chamber results in better mixing of the hydrogen, and more importantly more even distribution of the reactant mixture throughout the combustion chamber. The flow near the walls of the chamber moves faster than the flow at the center, thus providing a more quiescent domain in the vicinity of the spark plugs. The resultant lower rate of flame stretching in this region enables easier ignition. The flame propagates

rapidly outwards towards the faster perimeter flow which has more intense small-scale motion. Note that similar to A2, the pressure does not increase until after  $t = 0.5$  ms ( $t/\tau_{refill} = 0.0113$ ).

### 5.3.2 E5 (Low Peak Pressure Configuration)

#### *Non-Combusting Flow Field*

The non-combusting flow field of this configuration is shown in Figure 5.6, and immediately reveals some of the issues with this geometry. The air jet, visible in both P3 and N2, issues directly onto the spark plugs, such that fresh oxidant is the dominant species in the vicinity of the spark. The air jet then impinges on the opposite wall and spreads in directions normal to the jet axis, creating four recirculating domains. These domains are bounded by the walls of the combustion chamber, the plane P3, and a plane parallel to N2 containing the axis of the air inlet, and are as follows: 1)  $y > 7.5$  mm,  $z < 7$  mm, 2)  $y < 7.5$  mm,  $z < 7$  mm, 3)  $y < 7.5$  mm,  $z > 7$  mm, and 4)  $y > 7.5$  mm,  $z > 7$  mm. The hydrogen jet issues into the cross flow created by the air jet above the plane of the air inlet, which, while allowing some mixing, results in uneven distribution of the fuel in the two lower recirculating domains ( $y < 7.5$  mm). This therefore leads to a lean mixture both at the spark and in the recirculating regions below the air jet.

#### *Combusting Flow Field Evolution*

The PIV images of the flow field during combustion are shown in Figure 5.7. The time steps for PIV measurements following ignition are  $t = 0.1$  ms,  $0.5$  ms, and  $0.9$  ms to accommodate the slow rate of flame propagation relative to A2 and F1. At  $t = 0.1$  ms, the flow field remains unchanged. It is unknown if the mixture is ignited at this time, but

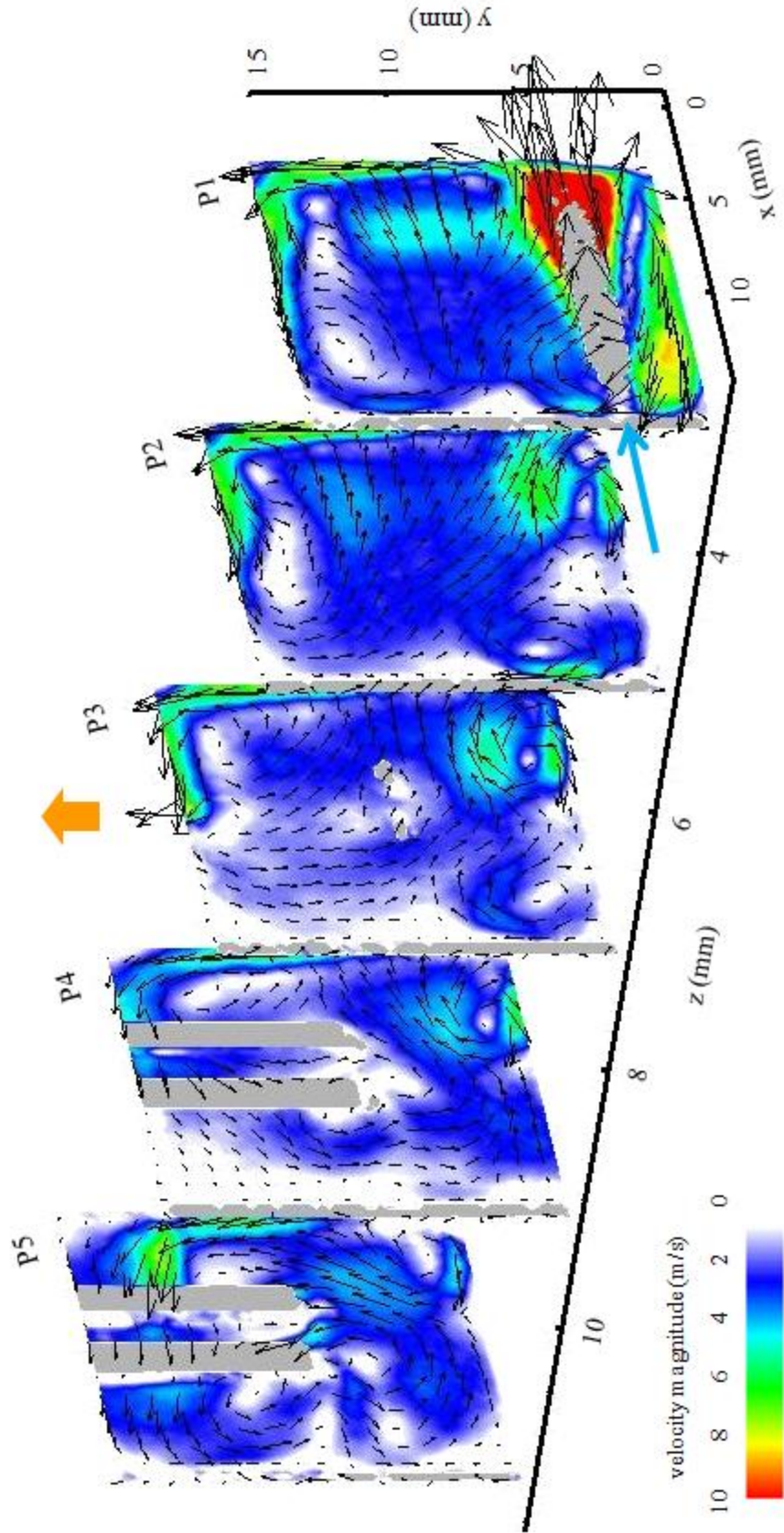


Figure 5.6a: Planar PIV cross-sections of the non-combusting flow field for configuration E5, P1-5,  $d_{air} = 0.79$  mm  $Q = 66.7$  s-cm<sup>3</sup>/s,  $\Phi = 0.75$  and  $f = 5$ Hz

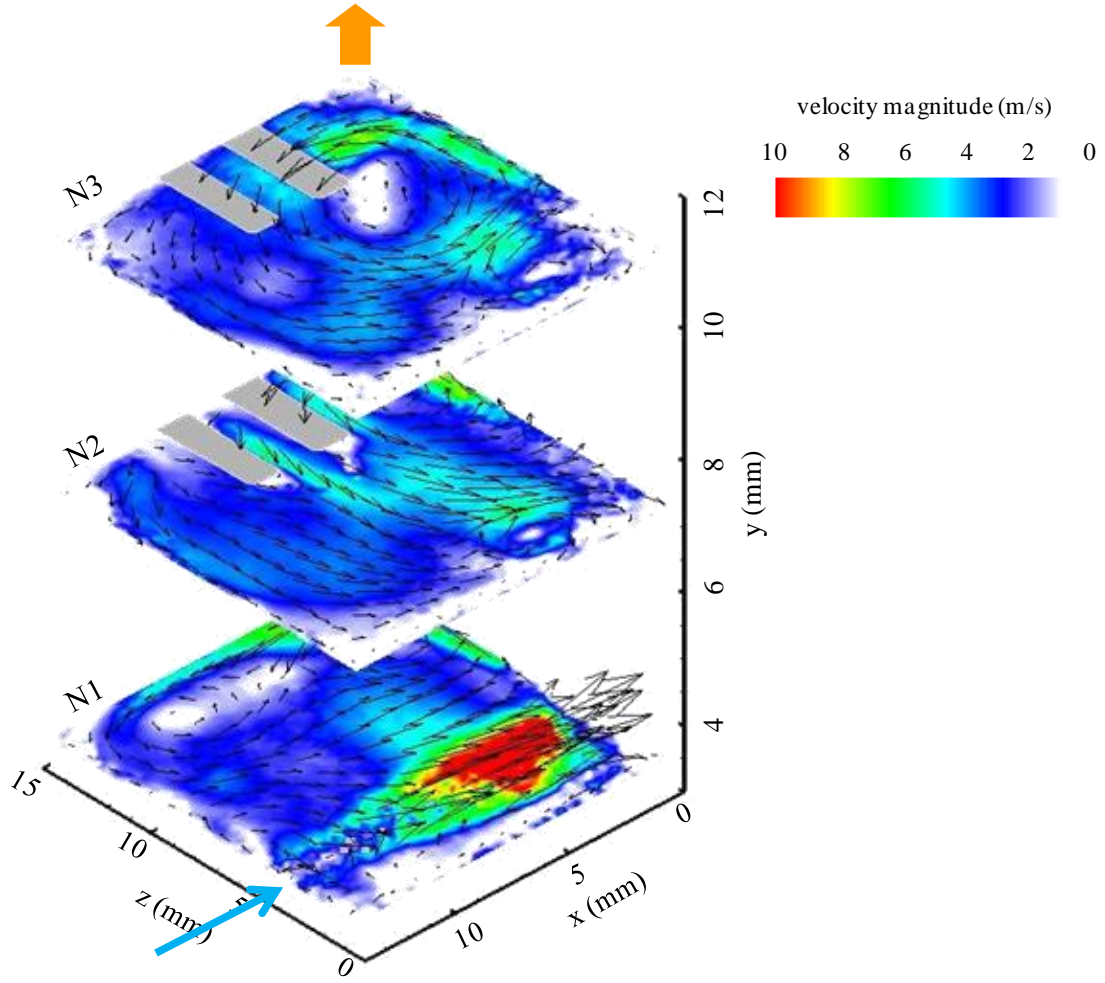


Figure 5.6b: Planar PIV cross-sections of the non-combusting flow field for configuration E5, N1-3,  $d_{air} = 0.79$  mm  $Q = 66.7$  s-cm<sup>3</sup>/s,  $\Phi = 0.75$  and  $f = 5$ Hz

because of its low local equivalence ratio as well as the flame stretching induced by the air jet, ignition is hindered and propagation of any flame front that is present is slowed.

By  $t = 0.5$  ms, the beginning of the flame front is visible in P3, in the path of the inlet jet near the spark plugs. The front moves preferentially towards the right wall, mainly due to advection by the air jet. This is also due to the position of the hydrogen inlet, as the concentration of fuel and therefore the flame speed is highest here as well.



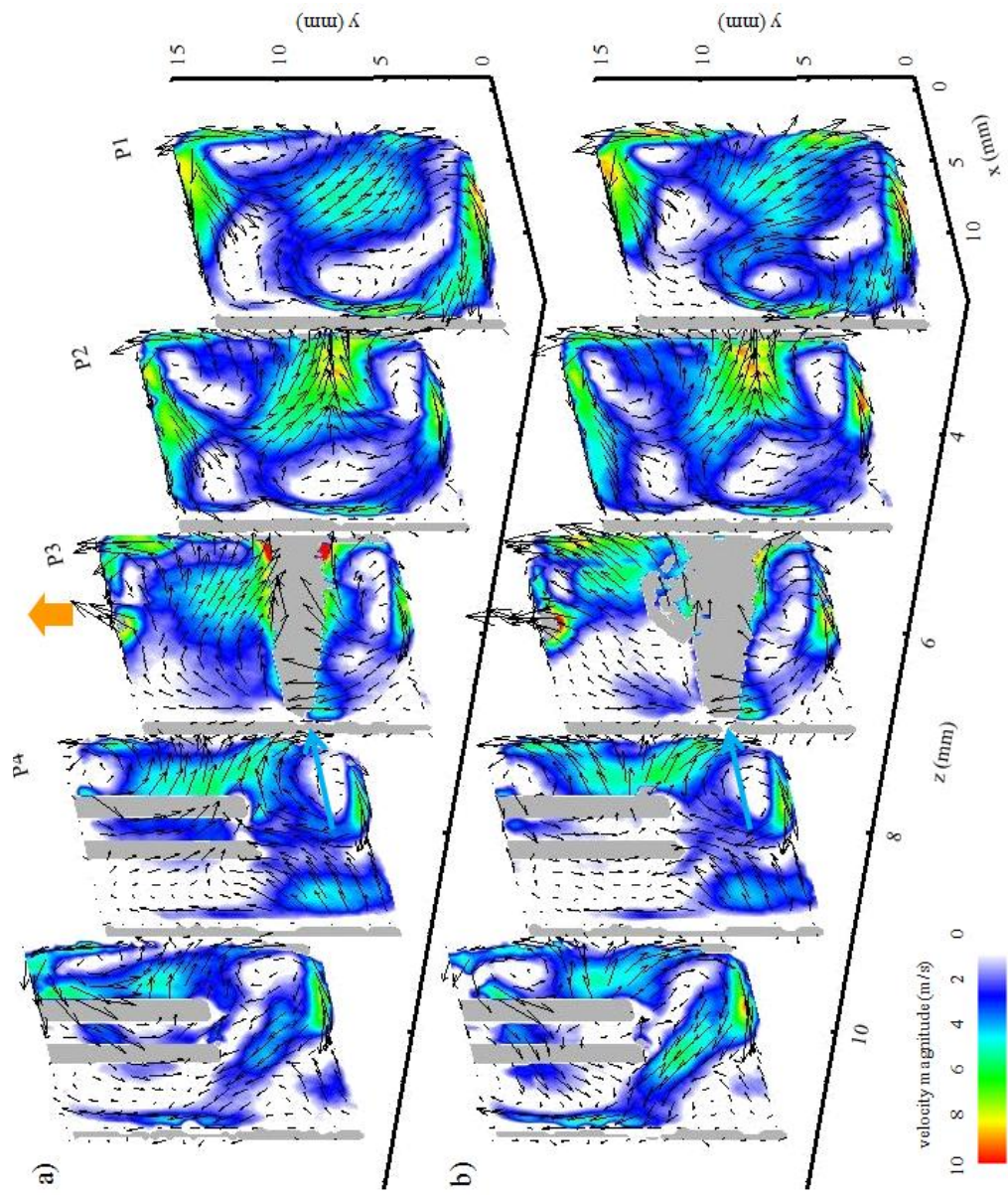


Figure 5.7: Planar PIV cross-sections of the combustor flow field of configuration E5,  $d_{air} = 0.79$  mm,  $Q = 66.7$  s-cm<sup>3</sup>/s,  $\Phi = 0.75$  and  $f = 5$ Hz, a)  $t = 0.1$  ms ( $t/\tau_{refill} = 0.002$ ), b)  $0.5$  ms ( $0.011$ )

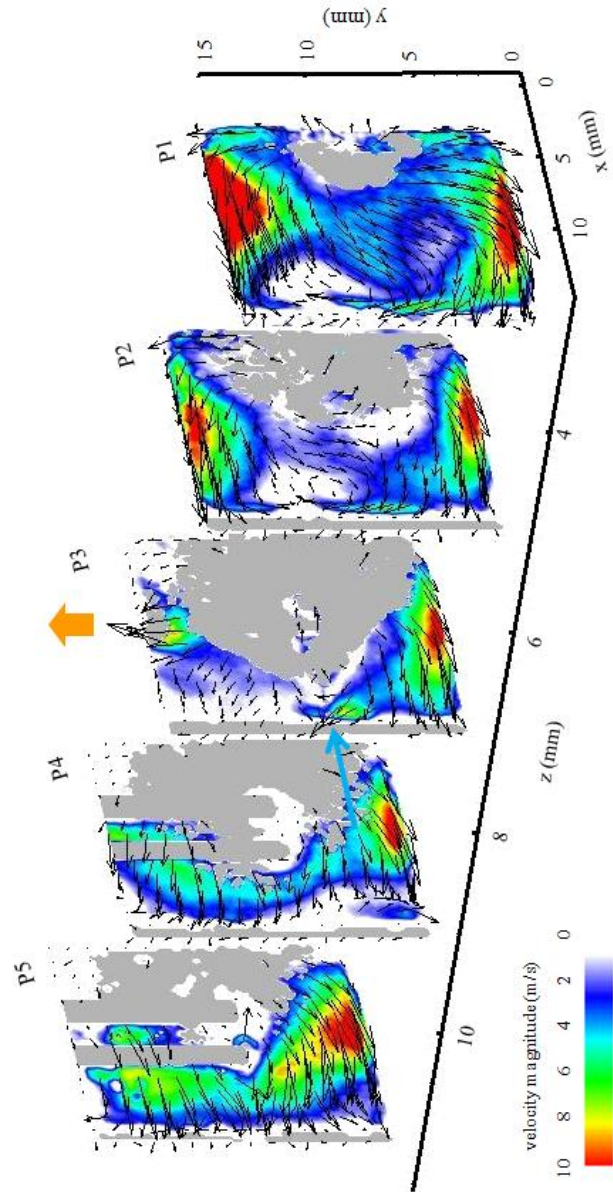


Figure 5.7c: Planar PIV cross-sections of the combustor flow field of configuration E5,  $d_{air} = 0.79$  mm,  $Q = 66.7$  s-cm<sup>3</sup>/s,  $\Phi = 0.75$  and  $f = 5$ Hz,  $t = 0.9$  ms ( $t/\tau_{refit} = 0.020$ )

At this time the front appears to move a relatively short distance, and bulk flow is unchanged, which is notably different from the flow field at  $t = 0.5$  ms ( $t/\tau_{refill} = 0.011$ ) for both A2 and F1. It is only by  $t = 0.9$  ms ( $t/\tau_{refill} = 0.020$ ) that the flame front consumes a significant portion of the reactants in the chamber. The front slowly advances towards the regions of most favorable equivalence ratio, and then propagates across the remainder of the chamber. At  $t = 0.9$  ms, the outflow at the exhaust orifice comprises unburned gasses being forced out by the expanding flame front, considerably worse compared to F1 and A2.

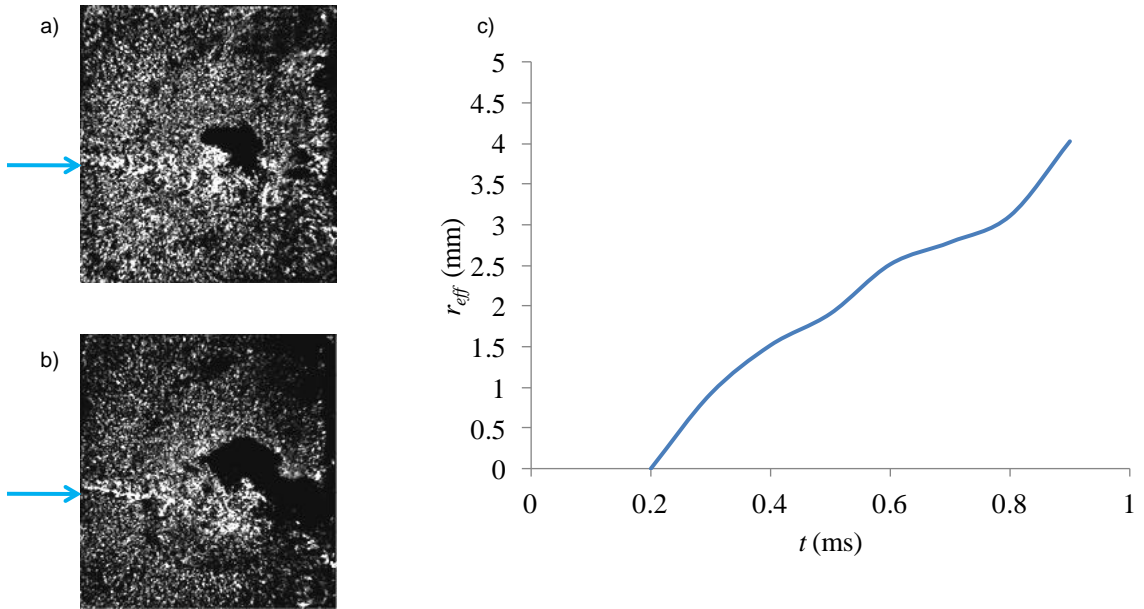


Figure 5.8: Images showing propagation of the flame front in the central plane P3 for configuration E5 at a)  $t = 0.3$  ms and b) 0.5 ms after spark ignition, and c) the change in  $r_{eff}$  with time.

Figures 5.8a and b show images of the flame front at  $t = 0.3$  and 0.5 ms, and Figure 5.8c shows the growth of the effective radius of the flame front. As in Figures 4.13 and 5.5, the flame front shows significant wrinkling as expected, and the flame moves toward the right wall as the PIV data suggests.

Figure 5.8c shows the increase in  $r_{eff}$  of the flame front with time. Compared to the same data for A2 (Figure 4.13c) and F1 (Figure 5.5c), the slope of the curve, and thus the flame speed is significantly lower, with a mean speed of around 5.2 m/s. Moreover, the late start of the flame front (obtained from the curve's intersection with  $t = 0$ ) shows that it is difficult to ignite the reactant mixture, which is consistent with the data about configuration E5 in Table 2. It should be noted that the approximation of a spherical flame-front used to calculate the flame speed is considerably less accurate in this case. For both A2 and F1, the flame front expanded in a roughly spherical manner, as determined from images of the expanding flame during operation. This is not the case for E5: the flame front does not approximate a sphere, moving almost entirely towards the right wall of the chamber with little propagation in other directions until after this region of high fuel concentration has been consumed. The exact shape of the flame front at any one time is irregular, and with more three-dimensional variation than the flame fronts in A2 and E5. The result is a flame that likely propagates more slowly than the  $r_{eff}$  approximation would suggest. This is the reason that the E5 pressure pulse lasts much longer than the pulse of A2 with  $d_{air} = 2.92$  mm, even though  $r_{eff}(t)$  is similar for both cases.

The single most important feature that results in diminished performance in E5 is the air jet blowing directly on the spark that leads to low local equivalence ratio in the vicinity of the spark plugs. This, combined with the flame stretching caused by the intense small-scale motion in the high-speed jet, makes the mixture harder to ignite. The positioning of the hydrogen inlet leads to local equivalence ratio in one half the chamber ( $y < 7.5$  mm) lower than that of the other half. Consequently, the flame propagates

unevenly, resulting in a lower overall flame speed, slower burning of reactants, more unburned reactants escaping through the exhaust orifice, and more incomplete combustion, all of which adversely impact actuator performance.

### **5.5 Flow field types and general effects**

At the flow rates and equivalent ratios tested, the air inlet jet dominates the flow field inside the chamber because of its high momentum flux relative to the hydrogen jet. Thus the  $3 \times 3$  inlet arrays allow for three basic types of flow field when using a single air inlet. If one does not consider the presence of the exhaust orifice and the spark plugs, the air inlet can be placed in a corner of the array, in the middle of one of the outer rows, or in the center of the array. The air jet issues out of the orifice and impinges on the opposing wall and is then forced to flow at right angles to the jet axis along the surface.

For a jet issuing from a corner orifice, the flow is forced to circulate counter-clockwise in orthogonal planes, shown in Figure 5.9, creating what was referred to in Section 5.4 as global circulatory flow. This is the general flow field that exists when the air inlet is at positions 1, 3, 7, or 9, (cf. Figure 5.1). Specifically, this is the flow field that exists for configuration F1, and in that case produces high peak pressures and maximum stable operating frequencies because the position of the inlets relative to the spark results in even mixing of the fuel and air and effective advection of the mixture throughout the chamber.

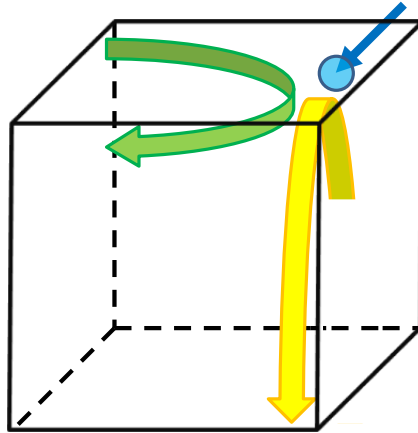


Figure 5.9: Simplified flow field for air inlet jet in corner of array

Table A (appendix) shows that configurations with air inlets at 1 and 7 exhibit considerably variation in terms of peak pressure and maximum operating frequency. The performance of such a configuration depends on the location of the hydrogen inlet. Due to this dependence, it is likely that detailed PIV and pressure data is needed to understand the effects of each flow field. With respect to the spark plugs, positions 1 and 7 mirror one another. However, the location of the exhaust orifice likely exerts a significant influence on the flow, which is evidenced by the very different behavior of A7 and E1. The former produces higher peak pressures, despite the similarities between the configurations.

Configurations with air inlets at positions 3 and 9 invariably produce a flow field that inhibits combustion when the hydrogen inlets are at A, C, and E. This is likely because position 3 is located directly below the spark plugs: while the air jet impinges on the opposite wall and creates circulation in the  $x$ - $y$  and  $y$ - $z$  planes (cf. Figure 3.2, for orientation), the presence of the spark plugs inhibits  $y$ - $z$  circulation. It is possible that this makes it difficult to ignite the mixture.

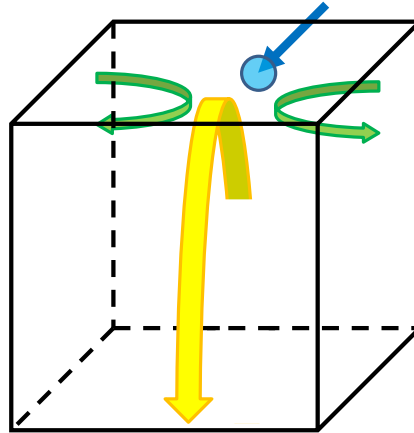


Figure 5.10: Simplified flow field for air inlet jet in middle hole on outer row of array

The second general flow field is produced when the air jet is placed in the middle hole on the edge of the array, between two corner holes. This corresponds to air inlet positions 2, 4, 6, and 8, and to configuration A2 (baseline), and is shown in Figure 5.10. In this type of flow field, the air jet issues from the orifice and impinges on the opposing wall, forcing it to circulate at right angles to the air inlet axis and along to the wall, as in the previous case. However, while circulation in one of the orthogonal planes is similar to the previous case (yellow arrow), circulation in the other directions occurs in two counter-rotating cells. In general, configurations with air inlets at position 2 perform worse than the baseline A2 configuration case, while inlet 4 performs better. This may happen because the spark plugs protruding into the flow disrupt the counter-rotating cells when the air inlet is at position 2 ( $y$ - $z$  plane), while the distortion of these circulation zones when the air inlet is at position 4 may be less severe (counter-rotating cells are in the  $x$ - $y$  plane), since the axes about which the circulating zones rotate are parallel to the spark plugs.

Configurations using air inlet 6 perform poorly, because the air jet blows directly on the spark plugs. Like all configurations with air inlets 3 and 9, the use of hydrogen inlets A, C, and E results in a chamber design that does not ignite the mixture. The obstruction caused by the spark plugs results prevents circulation. Instead, the flow pattern is more complicated and difficult to predict without either PIV (or simulation). It is likely that the obstruction of the sparks inhibits both mixing as well as advection of the mixture to the vicinity of the spark plugs, thus reducing the chamber's performance in these configurations. Like air inlet 2, inlet 8 produces worse than average performance, possibly because they are symmetric about the spark plugs, though the influence of the exhaust orifice would need to be investigated to confirm this hypothesis.

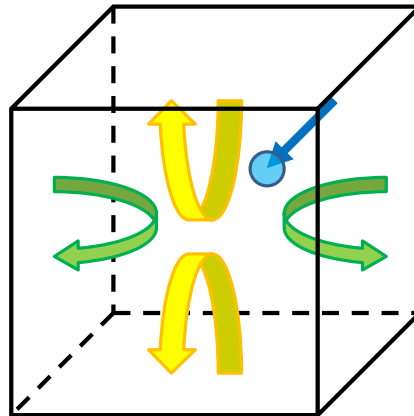


Figure 5.11: Simplified flow field for air inlet jet in central hole of array

The final type of circulatory flow occurs when the air jet emerges from the center orifice of the array, air inlet position 5. This is shown in Figure 5.11, and is the same flow observed in configuration E5. Flows resulting from these configurations circulate in two pairs of counter-rotating cells, because the air inlet jet directly impinges on the center of the opposing wall. The resulting performance from these chambers is typically poor,



producing some of the lowest peak pressures measured. In part, this is because the air jet blows directly on the spark plugs. This hinders chamber performance by making the mixture more difficult to ignite due to flame stretching and relative lack of fuel species in the vicinity of the spark (cf. Section 5.4 for more details). Moreover, this four-cell circulation pattern also means that unless the hydrogen inlet is at position C, in the center of the opposing wall, then the hydrogen jet issues into only one or two of the circulating regions, depending on the location of the inlet. This results in lower concentrations of fuel in the other cells, thus reducing flame speed and peak pressure in these regions of the flow, and causing longer pressure pulses.

## **CHAPTER 6**

### **CONCLUSION**

A novel combustion actuator was designed and fabricated for detailed investigations of the effect of the inlet flows and the internal flow field on the performance of combustion-powered actuators. Diagnostics included Particle Image Velocimetry (PIV) vector fields and time-resolved pressure traces. These data were used to assess the effect the momentum fluxes of the fuel and oxidizer inlet jets and their positions on the chamber walls have on the actuator's operating pressure and frequency. Combustion of air and fuel inside these actuators produces high speed, high momentum pulsed actuation jets that can be used for aerodynamic flow control.

In order to investigate the effect that the speed of the air inlet jet has on the operation and performance of the combustion actuator, the air and fuel inlets were placed near the base of the combustion chamber, opposite each other. Using this configuration, it was found that, at equivalence ratios and flow rates of interest, the air jet issuing from the inlet orifice has a dominant influence on the flow within the chamber, owing to its high momentum flux and volumetric flow rate. The performance of the actuator was quantified using the peak pressure produced during combustion, the impulse of the actuation jet, and timing parameters such as the rise time of the pressure pulse.

The diameter of the air inlet, which determines the speed and momentum flux of the air jet for a given equivalence ratio, determines the jet Reynolds number and affects the intensity of small-scale motion within the combustion chamber. In the present investigation, flame speed increases with intensity of small-scale motion, resulting in

faster heat release and consequently high peak pressures and shorter pulse durations. It was found that, of the three air inlets tested,  $d_{air} = 0.79$  mm produced the fastest inlet jet and highest momentum flux ( $Re_{air} > 6000$ , vs.  $Re_{air} = 1600$  for  $d_{air} = 2.92$  mm,  $\Phi = 0.75$ ,  $Q = 66.7$  s-cm<sup>3</sup>/s), and therefore the highest peak pressures ( $P_{max}/P_{atm} = 3.8$  vs. 2.6 for  $d_{air} = 0.79$  and 2.92 mm respectively), shortest pulse durations ( $\Delta t/\tau_{refill} = 0.0179$  vs. 0.0210), and highest stable operating frequencies ( $f_{max}/f_{refill} = 3.7$  vs. 1.9). This was verified by the scalar fields of Turbulent Kinetic Energy (TKE) within the combustion chamber, as well as contrast-enhanced images of the expanding flame front. The flame front shows wrinkling consistent with turbulent combustion in the “wrinkled laminar flame” regime.

The refill process was also investigated, showing that the chamber is filled more slowly when the momentum flux of the air jet is lower, even though the mass flow rate is unchanged. It was shown that increasing the actuator’s operating frequency also results in longer refill times. Although it should be noted that the method used to investigate the refill process may overestimate the time required, that the trends suggested are consistent with the other findings about actuator performance.

The second phase of experiments focused on the placement of the air and fuel inlets within the chamber, relative to each other as well as other chamber features such as the spark plugs and exhaust orifice. Air and fuel inlets were placed in different locations of the square grids on the walls.

It was found that there are three basic types of circulatory flow that are induced by the air inlet array: corner inlets cause global circulation through the entire volume of the chamber, center inlets result in four counter-rotating circulation cells, and inlets on

the edge of the grid between corner inlet positions produce two counter-rotating cells. The variations in flow field that determine whether a given configuration produces high peak pressures and high operating frequencies is a result of the interaction of the circulatory flow with the chamber's spark plugs. Two particular cases are discussed in detail: F1, which produces high peak pressures and can operate at high frequencies for all air inlet diameters tested, and E5, which performs poorly for all air inlet diameters, producing low peak pressures, and was unable to combust in a repeatable fashion at more than 20 Hz.

It was found that F1 benefits from the corner air inlet that allows the global circulation to effectively mix and distribute reactants throughout the volume of the combustion chamber. The spark itself is within a domain of relatively quiescent flow, which allows the nucleus of combustion (the hot spot and free radicals) to form without excessive stretching. Thus, the flame can propagate evenly throughout the chamber, and the refill process results in well-mixed reactants distributed throughout the chamber.

Conversely, E5 is of the four-cell type – in this particular case, the hydrogen inlet is confined to two of the four cells, resulting in an uneven mixture of reactants throughout the chamber. Aggravating this is the air inlet jet, which blows directly on the spark. This inhibits the steady propagation of the flame, and forces it to propagate unevenly, slowing it, and causing slower heat release, lower peak pressures, and long pulse durations.

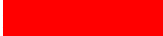
## APPENDIX

### TABLE A


This table lists peak pressures for the actuator described in this document assembled into a variety of configurations for  $d_{air} = 0.79, 1.63, \text{ and } 2.92$  mm operated at the following conditions: frequency  $f = 5$  Hz, equivalence ratio  $\Phi = 0.75$ , overall flow rate  $Q = 66.7$  std.  $\text{cm}^3/\text{s}$ .

$d_{air} = 0.79$ mm			$d_{air} = 1.63$ mm			$d_{air} = 2.92$ mm		
H <sub>2</sub>	Air	Peak press. (atm)	H <sub>2</sub>	Air	Peak press. (atm)	H <sub>2</sub>	Air	Peak press. (atm)
F	3	3.13	E	5	1.91	E	5	1.64
C	2	3.14	F	6	1.96	E	7	1.68
E	2	3.33	F	3	2.01	F	6	1.74
E	5	3.39	D	3	2.58	E	4	1.77
C	5	3.55	E	1	2.76	E	1	1.90
E	1	3.69	F	2	2.85	D	3	1.96
B	5	3.75	B	2	2.98	F	7	2.29
B	6	3.77	B	6	3.00	B	8	2.35
C	8	3.84	C	2	3.05	D	2	2.38
A	8	3.89	D	5	3.07	C	2	2.45
D	2	3.91	B	5	3.15	D	6	2.46
D	8	4.00	C	7	3.15	B	5	2.48
B	2	4.00	E	2	3.17	F	3	2.48
F	5	4.03	C	8	3.19	F	5	2.50
A	2	4.04	B	3	3.24	E	2	2.50
D	6	4.05	A	5	3.37	C	5	2.51
F	6	4.05	C	5	3.37	B	2	2.52
C	4	4.05	F	8	3.42	C	4	2.53
C	7	4.06	D	6	3.46	B	7	2.58
D	1	4.10	D	2	3.49	A	5	2.61
B	1	4.11	F	7	3.52	D	4	2.61
A	7	4.11	F	5	3.53	F	4	2.62
D	9	4.13	A	8	3.54	D	5	2.62
A	5	4.13	B	1	3.56	B	6	2.63
B	3	4.14	A	1	3.58	B	1	2.74
B	4	4.16	C	4	3.60	A	8	2.77
F	9	4.20	E	4	3.60	C	7	2.77
F	2	4.23	D	9	3.60	B	3	2.79
A	4	4.27	A	7	3.60	A	4	2.80
D	7	4.32	B	7	3.63	A	2	2.83
F	8	4.33	B	9	3.66	C	1	2.86

$d_{air} = 0.79 \text{ mm}$			$d_{air} = 1.63 \text{ mm}$			$d_{air} = 2.92 \text{ mm}$		
H <sub>2</sub>	Air	Peak press. (atm)	H <sub>2</sub>	Air	Peak press. (atm)	H <sub>2</sub>	Air	Peak press. (atm)
B	9	4.33	D	1	3.69	B	9	2.91
C	1	4.35	C	1	3.70	A	7	2.95
D	5	4.38	A	2	3.75	B	4	2.97
D	3	4.39	E	7	3.76	D	8	2.97
B	7	4.44	D	8	3.76	F	8	3.07
E	4	4.44	B	4	3.77	D	1	3.13
E	8	4.48	D	7	3.79	D	7	3.15
F	7	4.52	F	9	3.88	A	1	3.17
A	1	4.56	D	4	3.93	C	8	3.17
B	8	4.58	B	8	3.98	F	2	3.19
D	4	4.67	F	4	3.99	F	9	3.28
F	1	4.68	A	4	4.00	E	8	3.35
E	7	4.71	E	8	4.05	D	9	3.36
F	4	4.88	F	1	4.07	F	1	3.51

 configuration producing consistently low peak pressures

 baseline configuration

 configuration producing consistently high peak pressures

## REFERENCES

- Aichlmayr, H.T., Kittelson, D.B., and Zahcaria, M.R., "Miniature Free-Piston Homogeneous Charge Compression Ignition Engine-Compressor Concept – Part I: Performance Estimation and Design Considerations Unique to Small Dimensions," *Chemical Engineering Science*, **57**, pp. 4161-4171, 2002
- Aichlmayr, H.T., Kittelson, D.B., and Zahcaria, M.R., "Miniature Free-Piston Homogeneous Charge Compression Ignition Engine-Compressor Concept – Part II: Modeling HCCI Combustion in Small Scales with Detailed Homogeneous Gas Phase Chemical Kinetics," *Chemical Engineering Science*, **57**, pp. 4173-4186, 2002
- Bellorio, M.B. and Pimenta, J.M.D., "Theoretical Analysis of Air Conditioning by Evaporative Cooling Influence on Gas Turbine Cycles Performance," *Proceedings of 18<sup>th</sup> COBEM International Congress of Mechanical Engineering*, 2005
- Black, G., et al., "An Experimental and Modelling [sic] Study of the Combustion of Acetone," *Proceedings of 3<sup>rd</sup> European Combustion Meeting*, 2007
- Bradley, D. et al., "Laminar Burning Velocities of Lean Hydrogen-Air Mixtures at Pressures up to 1.0 MPa," *Combustion and Flame*, **149**, pp. 162-172, 2006
- Brzozowski, D. and Glezer, A., "Transient Separation Control using Pulse-Combustion Actuation," AIAA Paper 2006-3024, 2006
- Crittenden, T.M., "Fluidic Actuators for High Speed Flow Control," Department of Mechanical Engineering, Atlanta, GA, Georgia Institute of Technology, Ph.D. Thesis, 2003
- Crittenden, T.M. and Raghu, S., "Combustion Powered Actuator with Integrated High Frequency Oscillator," *International Journal of Flow Control*, **1-1**, pp. 87-97, 2009
- Crittenden, T.M., Warta, B.J., and Glezer, A., "Characterization of Combustion Powered Actuators for Flow Control," AIAA Paper 2006-2864, 2006
- Cutler, A.D. et al., "Development of a Pulsed Combustion Actuator for High-Speed Flow Control," AIAA Paper 2005-1084, 2005
- Cutler, A.D. and Drummond, J.P., "Toward a High-Frequency Pulsed-Detonation Actuator," AIAA Paper 2006-555, 2006

- Dowdy, D.R. et al., "The Use of Expanding Spherical Flames to Determine Burning Velocities and Stretch Effects in Hydrogen/Air Mixtures," *Twenty-Third Symposium (International) on Combustion*, The Combustion Institute, pp. 325-332, 1990
- Drell, I.L. and Belles, F.E., "Survey of Hydrogen Combustion Properties," National Advisory Committee for Aeronautics (NACA) Report 1383, 1957
- Epstein, A.H. et al., "Micro-Heat Engines, Gas Turbines, and Rocket Engines – The MIT Microengine Project," AIAA Paper 97-1773, 1997
- Fernandez-Pello, C.A., "Micropower Generation using Combustion: Issues and Approaches," *Proceedings of the Combustion Institute*, **29**, pp. 883-889, 2002
- Fu, K. et al., "Microscale Combustion Research for Applications to MEMES Rotary IC Engine," *Proceedings for the National Heat Transfer Conference*, **1**, pp. 613-618, 2001
- Funk, R. et al., "Transient Separation Control Using Pulse Combustion Actuation," AIAA Paper 2002-3166, 2002
- Lamoureux, N., Djebaili-Chaumeix N., and Paillard, C., "Laminar flame velocity determination for H<sub>2</sub>-air-He-CO<sub>2</sub> mixtures using the spherical bomb method," *Experimental Thermal and Fluid Science*, **27**, pp. 385-393, 2003
- Law, C.K., "A Compilation of Experimental Data on Laminar Burning Velocities," *Reduced Kinetic Mechanics for Applications in Combustion Systems*, edited by N. Peters and B. Rogg, Springer-Verlag, New York, pp. 15-26, 1993
- London, A.P., Epstein, A.H., and Kerrebrock, J.L., "High Pressure Bipropellant Microrocket Engine," *Journal of Propulsion and Power*, **17**-4, 2001
- Mattingly, J.D., "Elements of Gas Turbine Propulsion," American Institute of Aeronautics and Astronautics, 2005
- Milton, B.E. and Keck, J.C., "Laminar Burning Velocities in Stoichiometric Hydrogen and Hydrogen-Hydrocarbon Gas Mixtures," *Combustion and Flame*, **58**, pp. 13-22, 1984
- Moran, M.J. and Shapiro, H.N., "Fundamentals of Engineering Thermodynamics," 5<sup>th</sup> edition, Wiley, 2004
- Morley, C., "Gaseq: A Chemical Equilibrium Program for Windows," ver. 0.79, [www.c.morley.dsl.pipex.com](http://www.c.morley.dsl.pipex.com), 2005
- Ellis, H., ed., "Book of Data, Revised Nuffield Advanced Science," Revised Edition, Longman, 1999



- Ogawa, J. et al. "Design and Fabrication of a Micro Combustion Rig for Micro Reciprocating Engine," *Fourth International Workshop on Micro and Nanotechnology for Power Generation and Energy Conversion Applications*, Kyoto, Japan, 2004
- Protz, J.M., "An Assessment of The Aerodynamic, Thermodynamic, and Manufacturing Issues for the Design, Development, and Microfabrication of a Demonstration Micro Engine", Department of Aeronautics and Astronautics, Cambridge, MA, Massachusetts Institute of Technology, Ph.D. Thesis, 2000
- Raffel, M. et al., "Particle Image Velocimetry: A Practical Guide," 2<sup>nd</sup> edition, Springer, 1998
- Rajaratnam, N., "Developments in Water Science 5: Turbulent Jets," Elsevier, 1976
- Rajendar, A., Crittenden, T., and Glezer, A., "Characterization of the Internal Flow Dynamics of Combustion Powered Actuators," AIAA Paper 2008-3760, 2008
- Shan, X.C. et al., "A Silicon-Based Micro Gas Turbine for Power Generation," *Symposium on Design, Test, Integration, and Packaging of MEMS/MOEMS*, Stresa, Lago Maggiore, Italy, 2006
- Spadacinni, C.M., "Combustion Systems for Power-MEMS Applications", Department of Aeronautics and Astronautics, Cambridge, MA, Massachusetts Institute of Technology, Ph.D. Thesis, 2004
- Srinivas, S., Girgis, B., and Menon, S., "Large-Eddy Simulation of a Combustion Powered Actuator," AIAA Paper 2008-4680, 2008
- Swanger M. et al., "Small-Scale Rotary Engine Power System Development Status," *Western States Section of the Combustion Institute's Spring 2004 Meeting at the University of California, Davis*, 2004
- Tennekes, H., and Lumley, J., "A First Course in Turbulence," MIT Press, 1972
- Turns, S.R., "An Introduction to Combustion: Concepts and Applications," 2<sup>nd</sup> edition, McGraw-Hill, 2006
- Waitz, I.A., Gauba, G., and Tzeng, Y.H., "Combustors for Micro-Gas Turbine Engines," *Journal of Fluids Engineering*, **120**, pp. 109-117, 1998
- Warta, B.J., "Characterization of High Momentum Flux Combustion Powered Fluidic Actuators for High Speed Flow Control," Department of Mechanical Engineering, Atlanta, GA, Georgia Institute of Technology, M.S. Thesis, 2007
- Woo, G.T.K., Crittenden, T., and Glezer, A., "Transitory Separation Control over a Stalled Airfoil," AIAA Paper 2009-4281, 2009